

The official bi-monthly publication of Bhabha Atomic Research Centre



BARC newsletter

July-August 2023

ISSN: 0976-2108



▲ Hydrogen Recombiner ▲ Optimum HI to H₂ Conversion ▲ Fire Hazard Analysis ▲ RBI Governor visits BARC



Igniting young minds
Networking
WITH EMINENT PERSONS



Editor

Dr. S. Adhikari

Associate Editors

Dr. (Smt.) S. Mukhopadhyay

Dr. K.K. Singh

Editorial Assistant

Shri Madhav N

Design & Creative Work

Shri Dinesh J. Vaidya

Shri Madhav N

Newsletter Committee

Chairman

Dr. A.P. Tiwari

Members

Dr. A.K. Nayak

Dr. G. Sugilal

Dr. V.H. Patankar

Dr. (Smt.) B.K. Sapra

Dr. L.M. Pant

Dr. Ranjan Mittal

Dr. (Smt.) S. Mukhopadhyay

Dr. K.P. Muthe

Dr. V. Sudarsan

Dr. A.V.S.S.N. Rao

Dr. S.R. Shimjith

Dr. Sandip Basu

Dr. Pranesh Sengupta

Dr. R. Tripathi

Member Secretary &

Coordination

Shri Madhav N



BARC Newsletter
July-August 2023
ISSN: 0976-2108



INTERNATIONAL YEAR OF
MILLETS
2023

Computational Fluid Dynamics

An indispensable tool for in-depth understanding of flow and multi-physics systems

I am glad to write the foreword for this thematic issue of BARC Newsletter on “Computational Fluid Dynamics in Chemical Engineering, Material Science and Safety”. This is the second BARC Newsletter issue on this theme, the previous being November-December 2021 issue. The importance of computations and numerical simulations in all scientific and technological fields cannot be overemphasized. Particularly, Computational Fluid Dynamics (CFD) plays very important role in chemical engineering and related disciplines. While experiments are indispensable for validation purpose, CFD simulations help rationalize the number of experiments, virtually simulating some scenarios which, owing to being fraught with significant risk, cannot be studied experimentally. CFD simulation becomes a very useful practical tool if the phenomenon to be understood requires conducting highly controlled experiments. Also, the quantum of quantitative data and insights revealed by CFD simulations cannot be matched by experimental techniques. Having said this, it is worth mentioning that many problems such as the ones involving multiphase flows, phase change, breakage and coalescence of discrete phase, and multiphysics problems, pose significant challenges in CFD modelling. While, numerical tools and methodologies to solve such difficult problems are continuously being evolved, experimental validation remains an integral part of CFD modelling of such problems.

Increasing use of CFD by researchers is evident from the fact that the number of Scopus-indexed research articles having the word “CFD” in their title increased from up to 1500 during the period 1991-2000 to up to 7700 during the period 2001-2010. Further, the number of such articles increased to 18765 during the period 2011-2020. This whopping increase can partly be attributed to significant improvement in computational hardware and software which has made simulation of complex and large-scale problems easier. But the main reason is increasing reliance on CFD modelling by researchers.

This issue has 6 articles and 4 research highlights on CFD modelling. The first three articles are on applications of CFD in chemical engineering, the fourth article is on application of CFD in material science in which CFD has been used to analyse a system required for synthesis of CNT fiber. The last two articles highlight the use of CFD for safety related applications. Four research synopses provide a glimpse of the publication of the researchers and engineers working at BARC in the field of CFD.

I take this opportunity to thank Associate Editors for their time and efforts in preparing this issue, and the Newsletter Editorial Committee for suggesting the theme of the special issues on CFD in Chemical Engineering, Material Science and Safety. I would like to thank Dr. K.K. Singh, Head, Process Modelling and Demonstration Section, ChED, BARC for serving as one of the Associate Editors of these thematic issues. I would like to appreciate the efforts made by the authors for contributing articles to this special issue and the reviewers who have painstakingly reviewed the articles and gave suggestions to make them better. Special thanks to SIRD Editorial Team for their professional approach in preparing this issue of newsletter in a time-bound manner.

I hope this special issue will motivate young researchers and engineers to utilize CFD in pursuit of their research and development activities.

K. T. Shenoy

Director
Chemical Engineering Group
Bhabha Atomic Research Centre (BARC)

- **FOREWORD:** K. T. Shenoy, Director, Chemical Engineering Group, BARC 3

R&D IN CFD: APPLICATIONS IN CHEMICAL ENGG., MATERIALS SCIENCE AND SAFETY

- 1 **Numerical Simulations of HI Decomposition in Packed Bed Membrane Reactor with Molten Salt Heating** 7
B. C. Nailwal, N. Goswami, Soumitra Kar and A. K. Adak
- 2 **Incompressible Flow Solver using Least Square based Artificial Compressibility Method** 15
Mihir Chatterjee
- 3 **CFD Modeling of Fundamental Phenomena Relevant to Solvent Extraction: An Overview** 22
K. K. Singh, R. K. Chaurasiya, S. Sarkar, N. Sen and S. Mukhopadhyay
- 4 **CFD-enabled Optimization for Highly Efficient Purging in Glovebox used for CNT Fiber Production** 29
Rajath Alexander, Amit Kaushal and Kinshuk Dasgupta
- 5 **Hydrogen Recombiner CFD Model: Development, Benchmarking and Performance Evaluation** 33
Bhuvaneshwar Gera, Pavan K. Sharma, Vishnu Verma and Jayanta Chattopadhyay
- 6 **CFD based Fire, Explosion and Toxicity Safety Evaluation for Nisargruna Biogas Plant** 40
Pavan K. Sharma, Vishnu Verma and J. Chattopadhyay

RESEARCH HIGHLIGHTS: CFD APPLICATIONS IN CHEMICAL ENGG., MATERIALS SCIENCE & SAFETY

- 7 **SO₃ Decomposition in Tubular-Packed Bed Reactor** 47
S. Sujeesh
- 8 **CFD Modeling of Liquid-Liquid Flow and Mass Transfer** 48
Rajnish Kumar Chaurasiya
- 9 **A Novel Computational Model to Simulate Flow in a Vortex Mixer** 49
Sourav Sarkar
- 10 **Transmission, Evaporation of Cough Droplets Inside an Elevator** 50
Nirvik Sen

BOOK REVIEW

- **Insights into Laser Science** 51
Dhruba J. Biswas, Former Head, L&PTD, BARC

NEWS & EVENTS

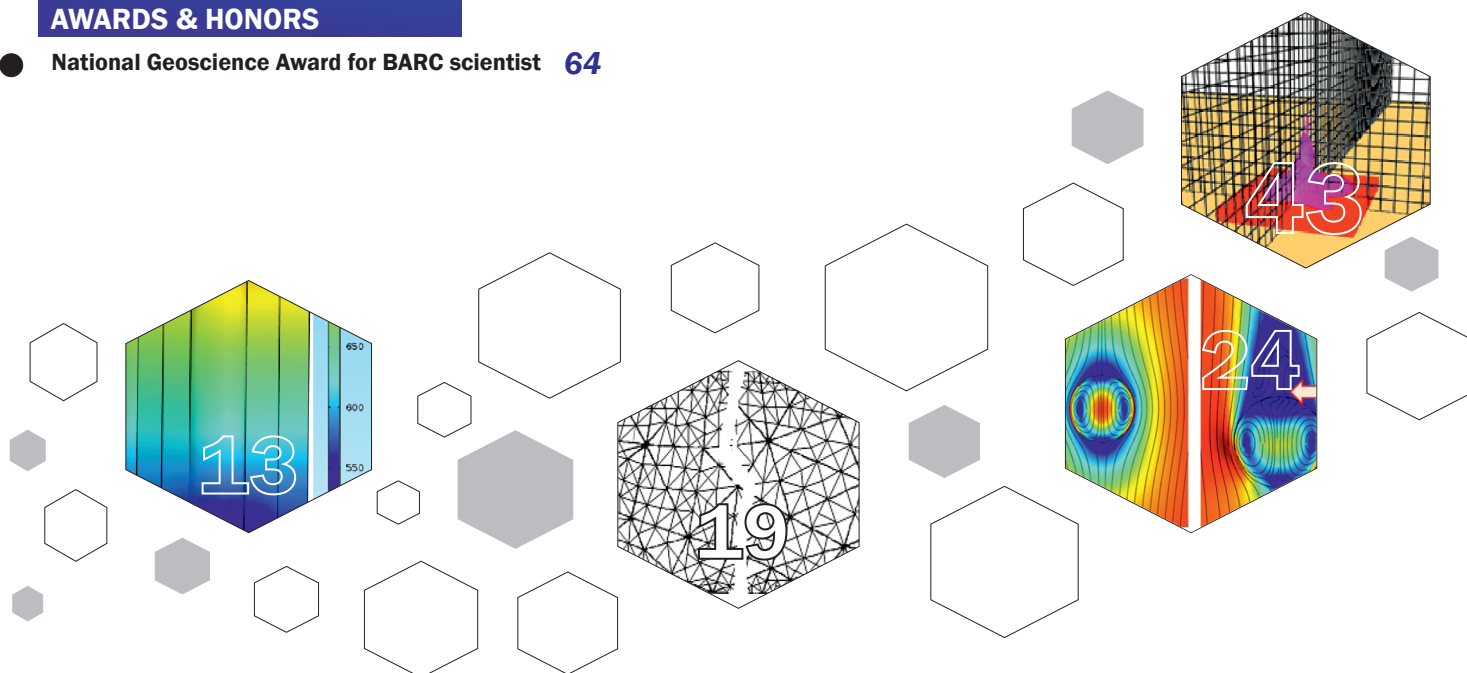
- **India should harness its R&D capabilities by capitalising on benefits of globalisation: RBI Governor Shri Shaktikanta Das** 52
- **Trombay Colloquium by Dr. Naba K. Mondal, and Dr. Raghunath A. Mashelkar** 54
- **BARC Chintan Baithak** 56
Chemistry Group, Chemical Engg. Group, Chemical Tech. Group; Physics Group
- **BARC Water Technologies secure the needs of India's Border Security Force** 58
Chemical Engineering Group and SIRD Editorial Team

SCIENTIFIC SOCIAL RESPONSIBILITY IN DAE

- **Glimpses of Parmanu Jyoti Program organized pan-India this year** 59

AWARDS & HONORS

- **National Geoscience Award for BARC scientist** 64



C O N T E N T S



This page intentionally left blank

Optimum HI to H₂ Conversion

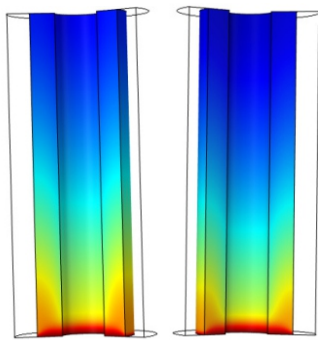
1

Numerical Simulations of HI Decomposition in Packed Bed Membrane Reactor with Molten Salt Heating

B. C. Nailwal¹, N. Goswami^{1*}, Soumitra Kar^{1,2} and A. K. Adak¹

¹Desalination & Membrane Technology Division, Bhabha Atomic Research Centre (BARC), Trombay – 400085, INDIA

²Homi Bhabha National Institute, Anushaktinagar, Mumbai- 400094, INDIA



HI mole fraction profile inside the membrane reactor at different outlet pressures

ABSTRACT

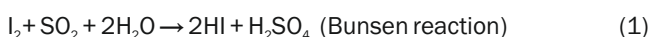
Hydrogen is considered amongst clean fuel options, for its utilization does not lead to emission of any pollutant or greenhouse gases. Water electrolysis and thermochemical cycles, coupled with renewable or nuclear energy source, are two important processes for green hydrogen energy production. Amongst the thermochemical routes, Iodine-Sulfur (IS) cycle offers advantages of higher efficiency and no solid handling. Efficiency of HI₂ processing section dictates the overall efficiency of IS thermochemical cycle. This section handles highly corrosive species, while the HI to H₂ equilibrium conversion is very low (~22%) at 700 K. In this work, the authors have carried out simulations of single-tube membrane reactor using tantalum composite membrane, coupled with molten salt heating, to determine the effect of various operating parameters on the conversion of HI. The optimum molten salt inlet temperature is found to be ~773 K, as beyond this temperature the conversion of HI does not increase, posing in addition the materials challenges. The findings confirmed that at a feed velocity of 0.0005 m/s, a conversion of ~83% can be achieved with the membrane tube radius of ~36 mm and a pressure of 3 bar. The studies provide useful insights into a molten-salt heated membrane reactor for optimum HI to H₂ conversion.

KEYWORDS: Green hydrogen energy, Iodine-Sulfur (IS) cycle, Membrane reactor

Introduction

It is important to reduce dependency on fossil fuels and look for promising alternatives. As energy demands are going to increase due to industrialization, population growth and betterment of life standards, the new technologies must be expandable. The upcoming energy sources needs to be environment friendly, i.e., energy sources should be green and cost effective. Considering these factors, hydrogen energy economy is going to be a game changer, offering a clean and green source of energy. Amongst different hydrogen production methods, steam reforming and water electrolysis are proven and used extensively for the production of hydrogen today. Thermochemical cycles have definite advantage over the electrochemical process because they do not involve conversion of heat into electricity. The IS cycle, a closed-loop thermochemical water splitting process, is of particular interest because unlike contemporary methods, it can produce hydrogen efficiently in being coupled with nuclear/solar energy source.

Following reactions are involved in IS process:



In Bunsen reaction (first reaction), H₂O reacts with I₂ and SO₂ to produce HI and H₂SO₄. In the second reaction, decomposition of H₂SO₄ to O₂, SO₂ and H₂O takes place, and SO₂

is recycled back to the Bunsen reaction. In the third reaction, decomposition of HI to H₂ and I₂ occurs. H₂ is collected as the product and I₂ is recycled back to the Bunsen section. The overall reaction is decomposition of H₂O into H₂ and O₂ [1]. However, the IS process has got several challenges.

The decomposition of HI to hydrogen is an equilibrium limited reaction with a very low conversion [2], leading to reduction in overall thermal efficiency of the process. In order to address this, ongoing research is focussed on development of membrane reactor [3]. In this work, CFD simulations of packed bed membrane reactor for HI decomposition using molten salt heating have been carried out. The molten salt is an effective technique to couple membrane reactor heating requirement with solar/nuclear energy. In this work, molten nitrate salt has been considered as the heating medium. Fig.1 shows the schematic of molten salt heated packed bed membrane reactor setup.

In this work, to the best of authors' knowledge, simulation studies on molten salt heated tantalum membrane-based reactor for application in IS thermochemical process are being reported for the first time.

Computational Approach

Momentum Transport

For packed bed membrane reactor Brinkman equation (Eq. (1)) was used.

$$\frac{\eta}{K} \bar{u} + \nabla \cdot \left[p\mathbf{I} - \frac{\eta}{\epsilon} (\nabla \bar{u} + (\nabla \bar{u})^T) \right] = 0 \quad (1)$$

*Author for Correspondence: Nitesh Goswami
E-mail: niteshg@barc.gov.in

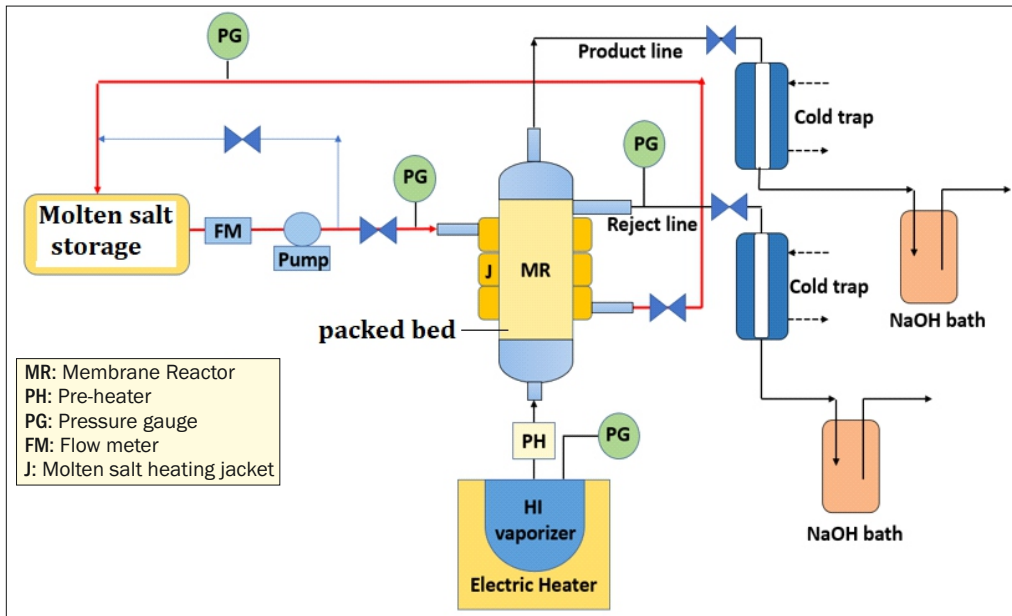


Fig.1: Schematic of molten salt heated packed bed membrane reactor setup.

The hydraulic permeability (κ) of the porous medium is defined by Eq. (2).

$$K = \frac{(d_p)^2 \varepsilon^3}{180(1-\varepsilon)^2} \quad (2)$$

To model momentum transport for molten salt flow in the jacket, Navier-Stokes equation was used.

Energy Transport

Eq. (3) is the energy transport equation used in the modelling. This equation has been used for simulation of both membrane reactor and molten salt heating domain. The equation accounts for both convective and conductive transport of the heat as well as heat generation due to reaction.

$$\rho C_p \left(\frac{\partial T}{\partial t} + \vec{u} \cdot \nabla T \right) = \nabla \cdot (k_i \nabla T) + Q \quad (3)$$

For molten salt heating, Q is taken as zero.

Species Transport

For species transport, Maxwell-Stefan diffusion and convection equation (Eq. (4)) was used for HI, H_2 and I_2 .

$$\nabla \cdot \left((\rho \omega_i \vec{u} - \rho \omega_i \sum_{j=1}^n D_{ij} (\nabla x_j + (x_j - \omega_j) \frac{\nabla p}{p})) - D_i^T \frac{\nabla T}{T} \right) = R_i \quad (4)$$

Reaction Kinetics

Langmuir-Hinshelwood type rate equation, as proposed by Oosawa et al [4] was used for carrying out the simulations. The simulations are carried out using the membrane permeability reported in literature [5]. The relevant expressions are given by Eqs. (5) - (8).

$$r_{HI} = -kpR_{HI} \quad (5)$$

$$R_{HI} = \frac{x_{HI}}{1 + K_{I_2} p x_{I_2}} - \frac{\sqrt{x_{H_2} x_{I_2}} (1 + K_{I_2} p \frac{\phi_e}{2})}{K_p (1 + K_{I_2} p x_{I_2})^2} \quad (6)$$

$$k = 1.58 \times 10^{-1} \exp \left(\frac{-34.31 \times 10^3 \text{ J mol}^{-1}}{RT} \right) \quad (7)$$

$$K_{I_2} = 5.086 \times 10^{-11} \exp \left(\frac{86.66 \times 10^3 \text{ J mol}^{-1}}{RT} \right) \quad (8)$$

The equilibrium constant, K_p for the decomposition of HI was obtained by the free energy values ($\Delta G \sim 12 \text{ kJ/mol}$) given in the JANAF [6], by means of the following equation:

$$K_p = \exp \left(\frac{-\Delta G}{RT} \right) \quad (9)$$

The physical properties for all the species like heat capacity, viscosity, density and thermal conductivity were calculated using equations reported in our previous work [7]. All these physical properties were taken to be temperature and pressure dependent.

Boundary Conditions

Fig.2 shows the computational domain with boundary conditions. A membrane reactor with single membrane tube has been considered for simulations.

For Momentum Transport:

- Outlet pressure of membrane reactor: p_o
- Inlet feed velocity to membrane reactor: u_o
- At wall: No slip condition
- Inlet velocity of molten salt: 0.0005 m/s
- Outlet pressure of molten salt: 1 atm

For Energy Transport:

- Inlet feed temperature to membrane reactor: 523 K
- At outlet of membrane reactor: $k_i \nabla T = 0$, $q_i \cdot \vec{n} = \rho C_p T \vec{u}$
- At molten salt wall: $Q_w = U A (T_2 - T)$
- Inlet temperature of molten salt: T_1

For Species Transport:

- Inlet mole fraction of HI, x_{10} : 0.95
- At outlet of the membrane reactor: $D_i \cdot \nabla c_i = 0$, $N_i \cdot \vec{n} = c_i \vec{u}$
- Flux of hydrogen at membrane wall: $Pe p x_2$

Validation of model

Since there is no relevant experimental data available in literature for the reactor geometry and conditions which have been used in the simulations of this work, an attempt was made to model a packed bed tubular reactor for steam

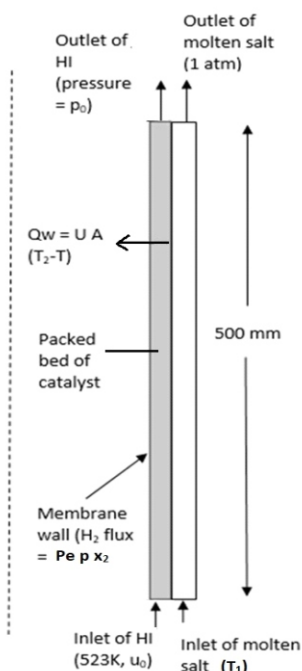


Fig.2: Computational domain with boundary conditions (dashed line show the axis of symmetry).

reforming of methanol using COMSOL Multiphysics by adopting the computational approach used for modeling of membrane reactor for HI decomposition in this study. The experimental data for steam reforming of methanol for packed bed tubular reactor has been reported in the literature [8]. The modeling of steam reforming of methanol was carried out to see the effect of ratio of weight of catalyst to methanol feed flow rate on the conversion. The results obtained by modeling were close to the values obtained through experiments. Table 1 shows the experimental and simulation results for the steam reforming of methanol (where X_{sim} is the conversion obtained by simulations and X_{exp} is the conversion reported in literature). The match between the experimental and simulation results for this case validates the computational approach which is then used for modeling of membrane reactor for HI decomposition in this work.

Results and Discussion

The computational approach validated with the reported experimental data of steam reforming of methanol was used to perform parametric analysis for HI decomposition reaction in molten salt heated single-tube membrane reactor. This section presents the results of this parametric analysis.

Effect of outlet pressure of reactor

Fig.3 shows the effect of pressure on conversion of HI inside the membrane reactor. It is observed that as the outlet pressure increases from 0.3 bar to 3 bar, the conversion of HI decomposition increases from 55% to 83%. It may be noted that the ceramic support tube on which metal is coated to fabricate the membrane can tolerate pressure up to 5 bar. As the pressure increases, the partial pressure of hydrogen increases due to increase in overall pressure leading to increase in driving force across the membrane for hydrogen transport. This increase in driving force leads to increase in flux of membrane as shown in Fig.4. The hydrogen flux increases from $3.15 \times 10^{-7} \text{ kg/m}^2\cdot\text{s}$ to $4 \times 10^{-6} \text{ kg/m}^2\cdot\text{s}$ as pressure is increased from 0.3 bar to 3 bar. Due to increase in hydrogen separation from the reaction mixture owing to permeation through the membrane, the HI decomposition reaction is pushed forward to a greater extent, leading to increased conversion.

Table 1: Validation of numerical simulations.

Ratio of catalyst mass to feed flow rate	X_{sim}	X_{exp}	Deviation (%)
35	0.959	0.89	7.7
40	0.967	0.9	7.4
45	0.972	0.92	5.6
50	0.976	0.94	3.8
55	0.979	0.95	3.1

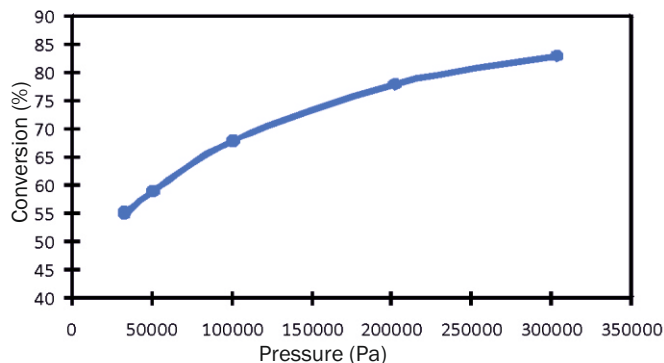


Fig.3: Effect of pressure on conversion of HI ($u_0 = 0.0005 \text{ m/s}$, $T_r = 500\text{K}$, $T_1 = 823\text{K}$, $x_{10} = 0.95$, $\epsilon = 0.3$).

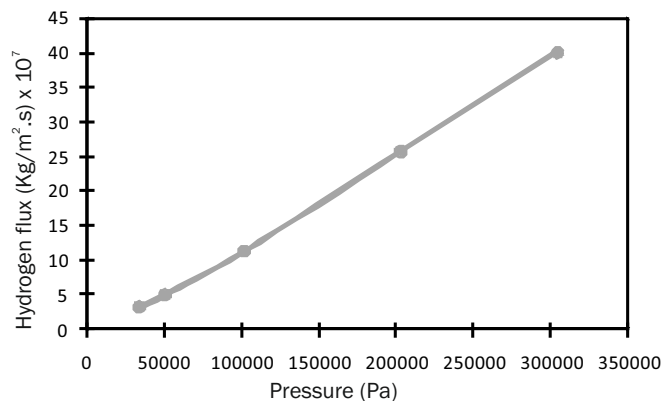


Fig.4: Effect of pressure on average flux of hydrogen ($u_0 = 0.0005 \text{ m/s}$, $T_r = 500\text{K}$, $T_1 = 823\text{K}$, $x_{10} = 0.95$, $\epsilon = 0.3$).

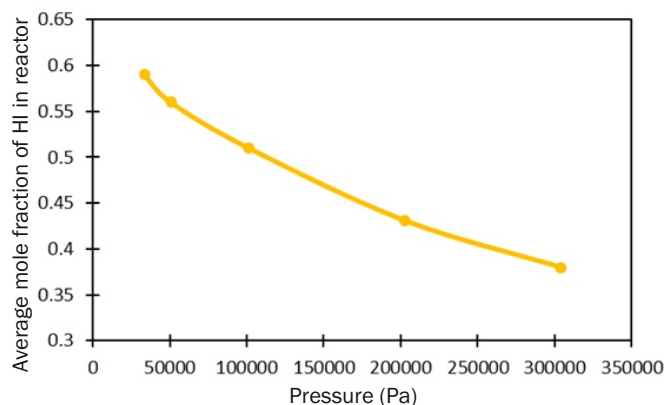


Fig.5: Effect of pressure on average mole fraction of HI in reactor ($u_0 = 0.0005 \text{ m/s}$, $T_r = 500\text{K}$, $T_1 = 823\text{K}$, $x_{10} = 0.95$, $\epsilon = 0.3$).

Fig.5 shows the effect of pressure on the average mole fraction of HI inside the membrane reactor. It is observed that the average mole fraction of HI decreases from 0.59 to 0.38 with increase in pressure from 0.3 bar to 3 bar. As the pressure increases, the flux through membrane increases which leads to increase in decomposition of HI and reduction of average mole fraction of HI.

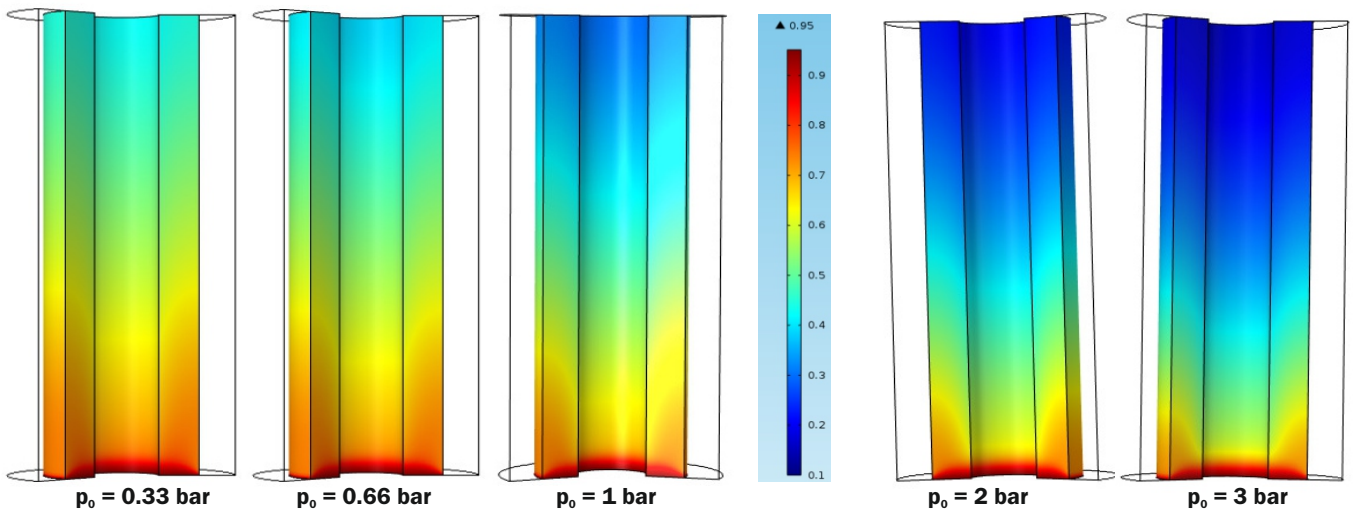


Fig.6: HI mole fraction profile inside the membrane reactor at different outlet pressures ($u_o = 0.0005 \text{ m/s}$, $T_r = 500\text{K}$, $T_1 = 823\text{K}$, $x_{10} = 0.95$, $\epsilon = 0.3$).

Fig.6 shows the contours of mole fraction of HI inside the membrane reactor at different pressures. It is seen that at higher pressure, the mole fraction becomes constant after a small distance from the inlet. This shows reaction reaching equilibrium within a short distance from the inlet at higher pressures. At lower pressure, the mole fraction of hydrogen does not become constant in axial direction indicating reaction is taking place throughout the reactor. The mole fraction of HI was found to be lower close to the membrane wall of reactor. This is because hydrogen permeation is higher in this zone and hence conversion also increases which leads to increased decomposition of HI near the walls.

Effect of inlet temperature of molten salt

Fig.7 shows the effect of inlet temperature of molten salt on the conversion of HI to hydrogen. It is observed that with increase in molten salt inlet temperature from 623 K to 823 K, the conversion of HI increases from 39 to 83%. With increase in temperature, rate of the reaction increases hence the conversion increases. It is also observed that beyond a certain point, the conversion becomes almost constant and does not change with temperature. This is because after a certain point, the membrane surface area is not sufficient to remove the increased amount of hydrogen from the reaction zone, leading to saturation in conversion. At the same time, density of gas mixture decreases with increases in temperature which lowers the residence time of gases. This is also corroborated from results shown in Fig.8 in which it can be observed that the hydrogen flux becomes almost constant after temperature of 773 K. Hence, it can be concluded that increasing the temperature beyond 773 K is not useful for conversion enhancement.

Fig.9 shows the effect of inlet temperature of molten salt on hydrogen generation rate inside the membrane reactor. It can be observed that it increases with increase in molten salt inlet temperature. In this case also, it can be seen that beyond 773 K, the rate of increase in hydrogen generation rate decreases as conversion tends to stagnate due to reasons mentioned earlier.

Fig.10 shows the contours of mole fraction of HI inside the membrane reactor at different inlet temperatures of molten salt. It is seen that at higher temperature (beyond 773 K), the mole fraction becomes constant after a small distance from the inlet. This shows reaction reaching equilibrium within a short distance from the inlet at higher temperatures. At lower temperatures, the mole fraction of HI varies in axial direction throughout the reactor length indicating higher utilization of membrane reactor length.

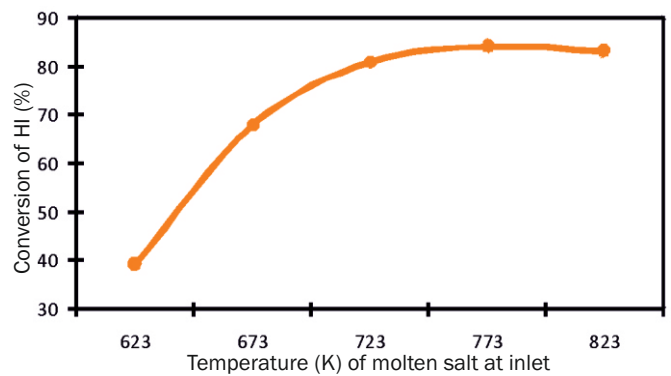


Fig.7: Effect of molten salt inlet temperature on HI conversion ($u_o = 0.0005 \text{ m/s}$, $T_r = 500\text{K}$, $x_{10} = 0.95$, $\epsilon = 0.3$, $p_o = 303975 \text{ Pa}$).

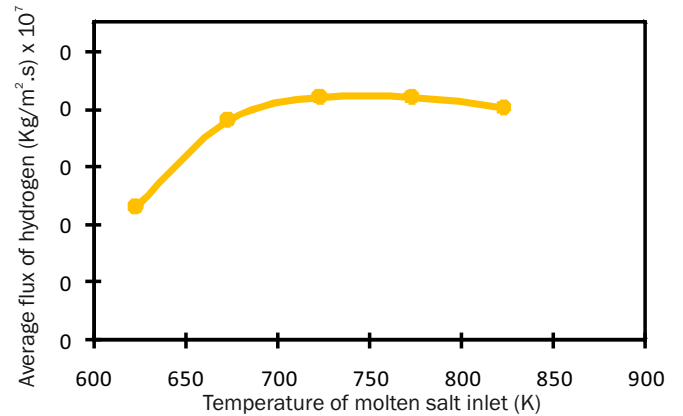


Fig.8: Effect of molten salt inlet temperature on average flux of H_2 ($u_o = 0.0005 \text{ m/s}$, $T_r = 500\text{K}$, $x_{10} = 0.95$, $\epsilon = 0.3$, $p_o = 303975 \text{ Pa}$).

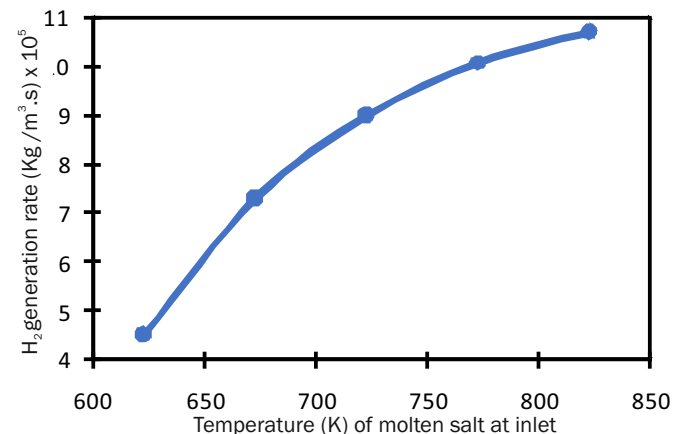


Fig.9: Effect of molten salt inlet temperature on H_2 generation rate ($u_o = 0.0005 \text{ m/s}$, $T_r = 500\text{K}$, $x_{10} = 0.95$, $\epsilon = 0.3$, $p_o = 303975 \text{ Pa}$).

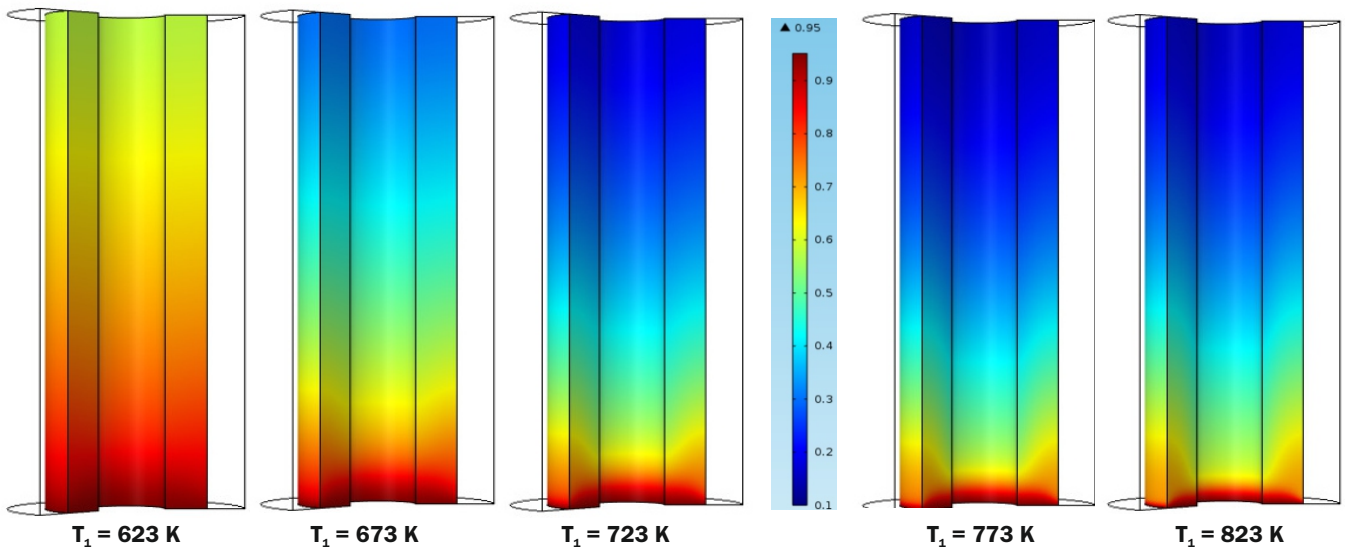


Fig.10: HI mole fraction profile inside the membrane reactor at different inlet temperatures of molten salt ($u_0 = 0.0005\text{ m/s}$, $T_r = 500\text{ K}$, $x_{10} = 0.95$, $\varepsilon = 0.3$, $p_0 = 303975\text{ Pa}$).

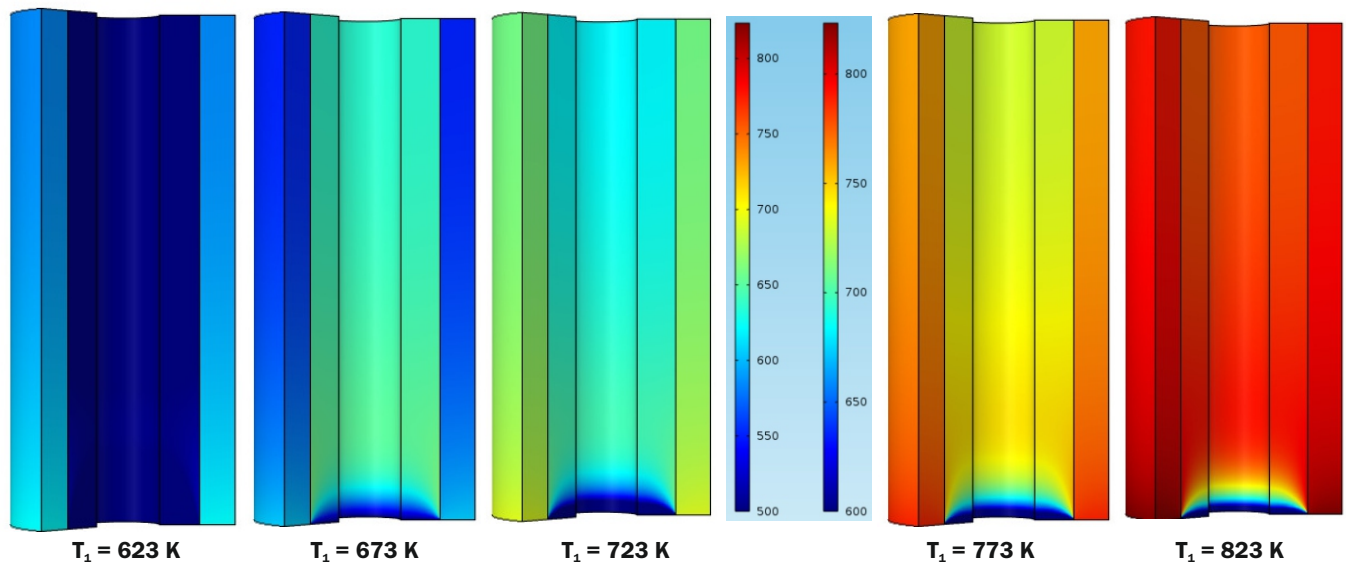


Fig.11: Contours of temperature inside the membrane reactor at different inlet temperatures of molten salt ($u_0 = 0.0005\text{ m/s}$, $T_r = 500\text{ K}$, $x_{10} = 0.95$, $\varepsilon = 0.3$, $p_0 = 303975\text{ Pa}$; the first scale corresponds to reaction mixture temperature and the second corresponds to molten salt temperature).

Fig.11 shows the contours of temperature inside the membrane reactor and in the molten salt flow channel at different inlet temperatures of molten salt. It is seen that at all the values of molten salt inlet temperatures, the temperature inside the reactor becomes constant after a small distance from the inlet. Hence, it can be concluded that for the entire range of molten salt inlet temperatures, the temperature of the reactor remains uniform throughout. This is because this simulation is carried out at optimised feed velocity of 0.0005 m/s , at which the residence time of reactant species is sufficient to allow effective heat transfer causing the temperature to become constant within a short distance from inlet.

Effect of feed velocity

Fig. 12 shows the effect of feed velocity on conversion of HI. As the feed velocity increases, conversion reduces. A conversion of $\sim 83\%$ is obtained at a feed velocity of 0.0005 m/s . From this figure, it may be concluded that lower velocities increase the residence time and hence the conversion. So, it would be preferable to operate the reactor at a low feed rate, however, it will be at the cost of lower throughput.

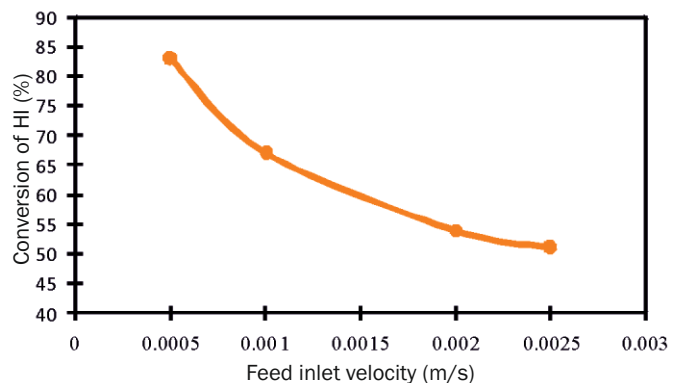
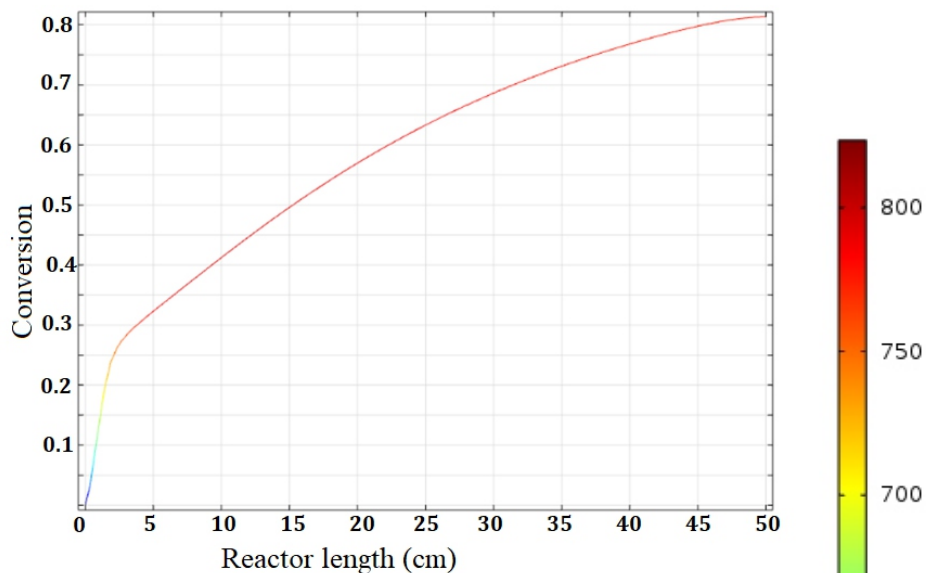


Fig.12: Effect of feed velocity on conversion of HI ($T_1 = 773\text{ K}$, $T_r = 500\text{ K}$, $x_{10} = 0.95$, $\varepsilon = 0.3$, $p_0 = 303975\text{ Pa}$).

Effect of flow direction of molten salt

Fig.13 shows the conversion of HI decomposition inside the membrane reactor for co-current and counter-current flow of molten salt with respect to the feed flow. It is observed that a higher conversion of $\sim 83\%$ is achieved in co-current flow

(a) Co-current flow



(b) Counter-current flow

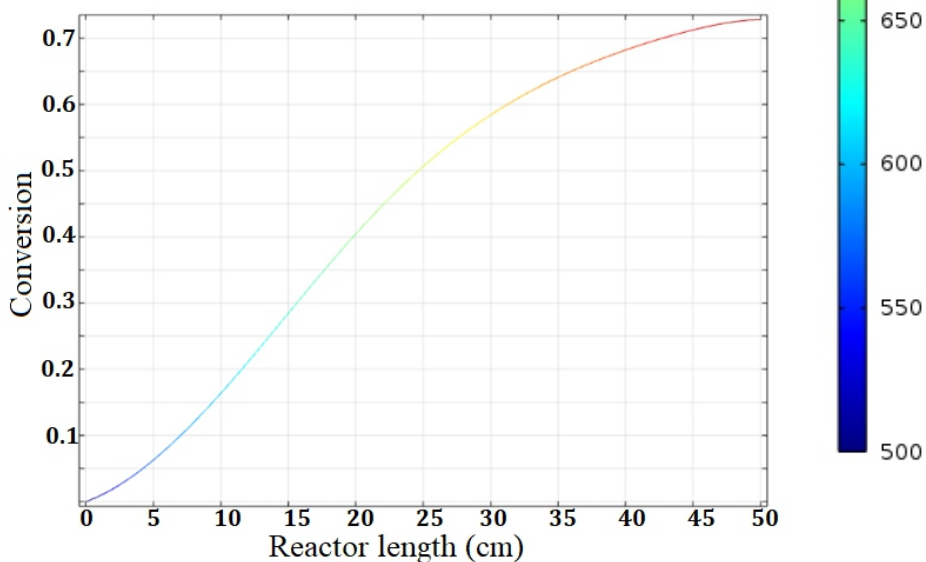


Fig.13: Effect of flow patterns on conversion of HI ($T_1 = 773\text{ K}$, $T_f = 500\text{ K}$, $x_{10} = 0.95$, $\epsilon = 0.3$, $p_0 = 303975\text{ Pa}$, $u_0 = 0.0005\text{ m/s}$).

compared to a conversion of ~73% in counter-current flow. This is because in co-current flow, there is a higher temperature near the inlet of the reactor (where concentration of HI is higher) which leads to enhanced reaction rate and conversion increases. This can also be seen in the curve (Fig.13(a)), in which the temperature of gas mixture remains higher at the inlet of the reactor, in case of co-current flow. For counter-current flow, since the molten salt enters from opposite end, the HI in the feed remains at a lower temperature (as can be seen in curve in Fig.13(b)) which leads to a lower overall conversion. Similar trend can be seen in temperature contours shown in Fig.14. Fig.15 shows the mole fraction of HI inside the membrane reactor for both the flow patterns. It can be seen that in case of co-current flow the mole fraction of HI is lower inside the membrane reactor as compared to counter-current flow due to reasons already mentioned above.

Effect of outer radius of membrane tube

Fig.16 shows that there is an increase in conversion as outer radius of membrane tube increases. The conversion increases from 64% to 83% on increasing membrane tube radius from 1.8 cm to 3.6 cm. This is because of increased membrane surface area and hence increase in hydrogen

permeation due to increase in outer radius. As the targeted conversion is 80%, the optimum outer radius in this case will be 3.6 cm.

Optimum parameters for molten salt heated membrane reactor

A final simulation was carried out using packed bed configuration of a membrane reactor taking into account various considerations and results obtained as mentioned in previous sections, with following parameters:

- Feed velocity = 0.0005 m/s
- Molten salt inlet temperature = 773 K
- Outlet pressure = 3 bar
- Membrane tube outer radius = 3.6 cm
- Reactor length = 50 cm
- Feed temperature = 500 K
- Feed Composition: 95% HI
- Packed bed porosity = 0.3

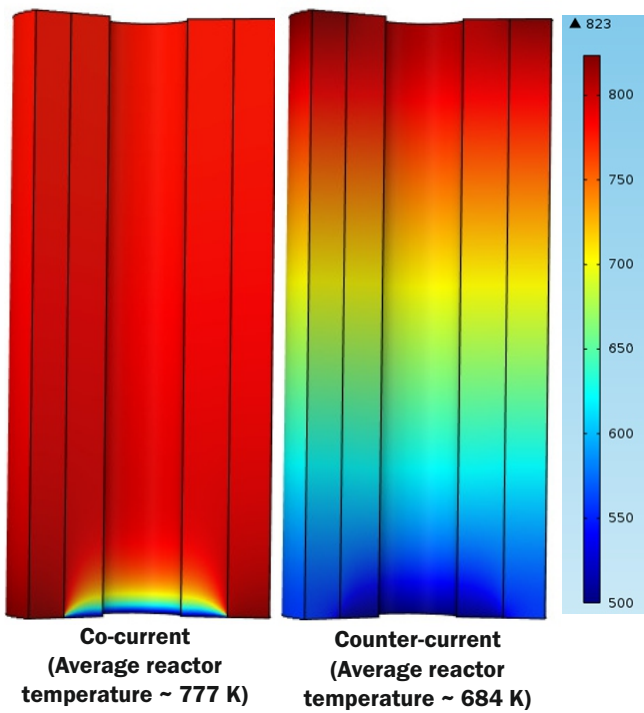


Fig.14: Contours of temperature inside the membrane reactor for co-current and counter-current flow ($T_i = 773\text{ K}$, $T_r = 500\text{ K}$, $x_{i0} = 0.95$, $\epsilon = 0.3$, $p_0 = 303975\text{ Pa}$, $u_0 = 0.0005\text{ m/s}$).

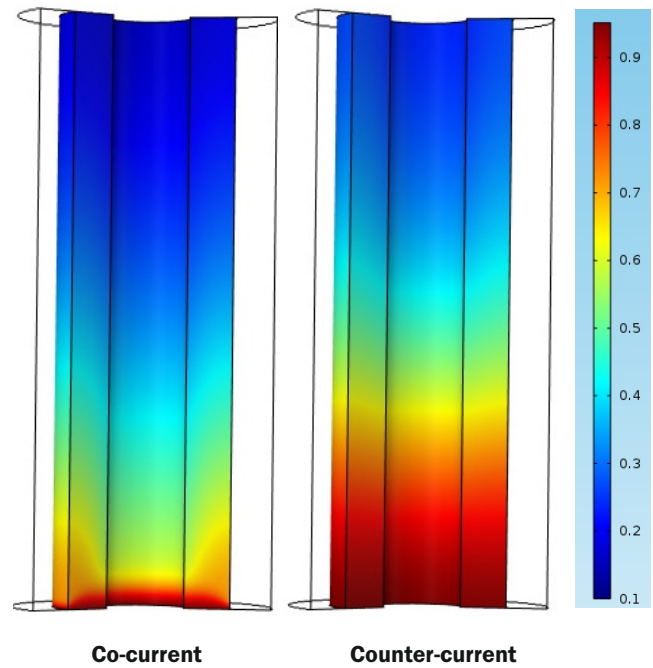


Fig.15: HI mole fraction profile inside the membrane reactor for co-current and counter-current flow ($T_i = 773\text{ K}$, $T_r = 500\text{ K}$, $x_{i0} = 0.95$, $\epsilon = 0.3$, $p_0 = 303975\text{ Pa}$, $u_0 = 0.0005\text{ m/s}$).

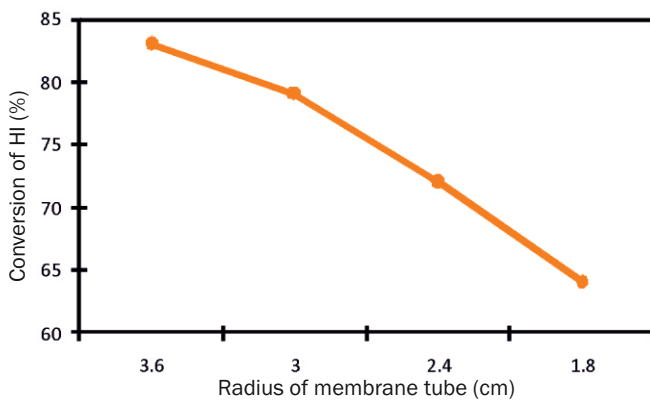


Fig.16: Effect of membrane tube radius on conversion of HI ($T_i = 773\text{ K}$, $T_r = 500\text{ K}$, $x_{i0} = 0.95$, $\epsilon = 0.3$, $p_0 = 3,03,975\text{ Pa}$, $u_0 = 0.0005\text{ m/s}$).

The conversion obtained for simulation of this design was 83%. The contours of mole fractions of HI, H_2 and I_2 for this simulation are shown in Fig.17. The hydrogen mole fraction first increases near the inlet and then decreases to become constant near the outlet. This is because near the inlet, hydrogen is produced due to HI decomposition and it permeates out from the membrane throughout the reactor length and its mole fraction decreases. The mole fraction of iodine increases along the reactor length as it is produced by reaction, with a higher mole fraction near the walls where hydrogen permeates out. It becomes constant near the outlet confirming that the entire reactor length as well the membrane surface area is sufficient to achieve the maximum conversion possible in this configuration.

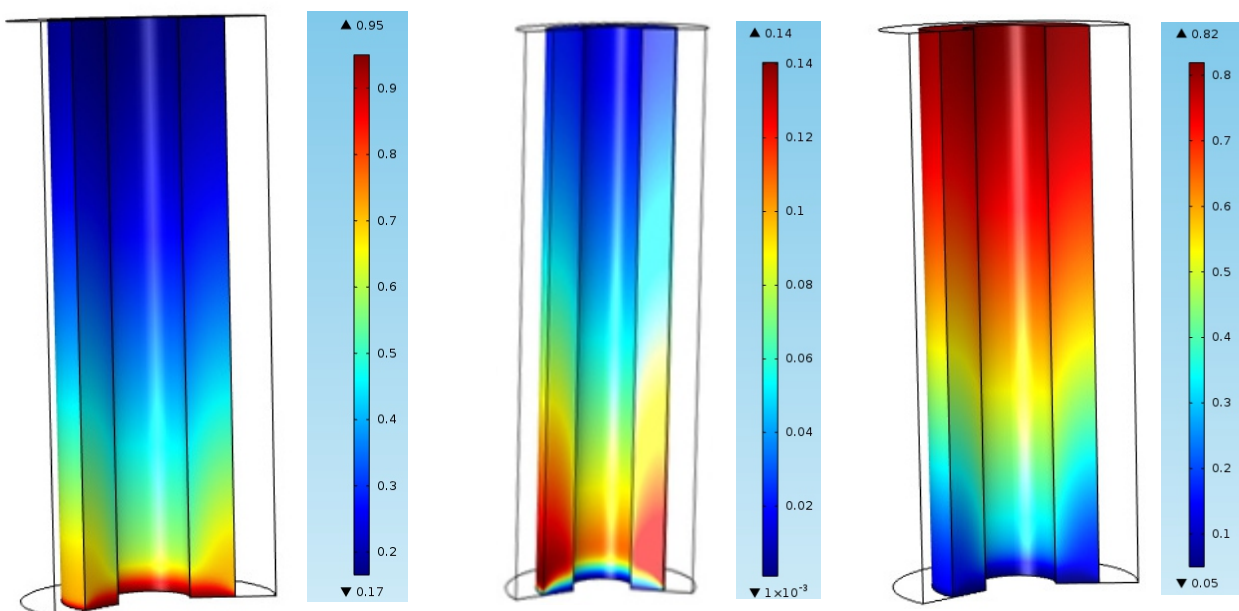


Fig.17: Contours of mole fraction of HI, H_2 and I_2 inside the membrane reactor at optimum parameters.

Conclusions

A CFD model of molten salt heated packed bed membrane reactor for HI decomposition is reported. The computational approach used in the model was validated with the literature data. Subsequently, the validated model was used for parametric analysis which provides important insights into the effect of various operating conditions on the performance of membrane reactor for HI decomposition reaction. The optimum molten salt inlet temperature was found to be ~ 773 K because as the temperature increases further, it has minimal effect on the conversion, while posing materials challenges. With increase in pressure, the conversion was found to increase. It was found that co-current flow of molten salt with respect to feed flow gives a higher conversion as compared to counter-current flow. The optimum parameters were found to be: feed velocity = 0.0005 m/s; molten salt inlet temperature = 773 K; outlet pressure = 3 bar; membrane tube outer radius = 3.6 cm; reactor length = 50 cm. A conversion of $\sim 83\%$ was achieved with these parameters at a HI throughput of ~ 400 ml/min. It was found that membrane reactor enhanced the conversion at least by $\sim 60\%$ above & beyond that obtained in a conventional packed bed reactor. The CFD model embedding all the transport phenomena, reported in this study can be used as a virtual prototyping tool to screen potential design alternatives.

Acknowledgements

The authors acknowledge the requisite COMSOL computing support and technical guidance provided by Dr. K.K. Singh, Chemical Engineering Division (ChED), BARC.

References

- [1] J. E. Murphy, J. P. O'Connell, "Process simulations of HI decomposition via reactive distillation in the sulfur-iodine cycle for hydrogen manufacture", *Int. J. Hydrog. Energy*, 37 (2012), pp 4002-4011.
- [2] T. D.B. Nguyen, Y-K. Gho, W. C. Cho, K. S. Kang, S. U. Jeong, C. H. Kim, C-S. Park, K-K. Bae, "Kinetics and modeling of hydrogen iodide decomposition for a bench-scale sulfur-iodine cycle", *Appl. Energy*, 115 (2014) 531-539.
- [3] S. Kar, R.C. Bindal, S. Prabhakar, P.K. Tewari, "The application of membrane reactor technology in hydrogen production using S-I thermochemical process: A roadmap", *Int. J. Hydrog. Energy*, 37 (2012), pp 3612-3620.
- [4] O. Yoshinao, K. Toshiya, M. Susumu, K. Wakichi, T. Yoshio, F. Kinjiro, "Kinetics of the catalytic decomposition of hydrogen iodide in the magnesium-iodine thermochemical cycle", *Bull. Chem. Soc. Jpn.*, 54 (1981), pp 742-748.
- [5] G.-J. Hwang, K. Onuki, "Simulation study on the catalytic decomposition of hydrogen iodide in a membrane reactor with a silica membrane for the thermochemical water-splitting IS process", *J. Membr. Sci.*, 194 (2001), pp 207-215.
- [6] JANAF Thermochemical Tables, Dow Chemical Company, Midland, 1977.
- [7] N. Goswami, K.K. Singh, S. Kar, R.C. Bindal, P.K. Tewari, Numerical simulations of HI decomposition in packed bed membrane reactors, *Int. J. Hydrog. Energy*, 39 (2014), pp 18182-18193.
- [8] A. Karim, J. Bravo, A. Datye, Non isothermality in packed bed reactors for steam reforming of methanol, *Appl. Catal. A: General*, 282 (2005), pp 101-109.

Notations

A	area of reactor wall	(m ²)
C _p	effective heat capacity of gas mixture	(J/mol.K)
d _p	particle diameter	(m)
D _{ij}	binary diffusivity	(m ² /s)
D _i	Diffusivity of i th species	(m ² /s)
ΔG	change in Gibbs free energy	(kJ/mol)
k	rate constant	(mol m ⁻³ Pa ⁻¹ s ⁻¹)
k _t	effective thermal conductivity	(W/m.K)
K _{I₂}	adsorption equilibrium constant of iodine	(Pa ⁻¹)
K _p	equilibrium constant	
p	pressure	(Pa)
p ₀	pressure at outlet of reactor	(Pa)
Pe	permeance of membrane for hydrogen	(mol/m ² .Pa.s)
Q	heat source	(W/m ³)
Q _w	heat transferred to reaction zone through reactor wall	(W/m ³)
r _{HI}	rate of reaction	(mol m ⁻³ s ⁻¹)
R	universal gas constant	(J/mol.K)
R _i	source term due to reaction for species	(kg/m ² .s)
t	time	(s)
T	temperature of gaseous mixture	(K)
T _f	feed temperature	(K)
T ₁	molten salt inlet temperature	(K)
T ₂	temperature of molten salt	(K)
\vec{u}	velocity vector	(m/s)
u ₀	magnitude of x component of feed velocity	(m/s)
U	overall heat transfer coefficient	(W/m ² .K)
x _j	mole fraction of component j	(j=1 (HI), 2 (H ₂), 3 (I ₂))
x _{j0}	mole fraction of component j at reactor inlet	(j=1 (HI), 2 (H ₂), 3 (I ₂))

Symbols

κ	hydraulic permeability of porous medium	(m ²)
φ _e	equilibrium conversion	(~ 0.21 at 700 K)
ω _j	mass fraction of component j	
η	viscosity of the gaseous mixture	(kg/m.s)
ε	porosity of bed	
ρ	effective density of gas mixture	(kg/m ³)

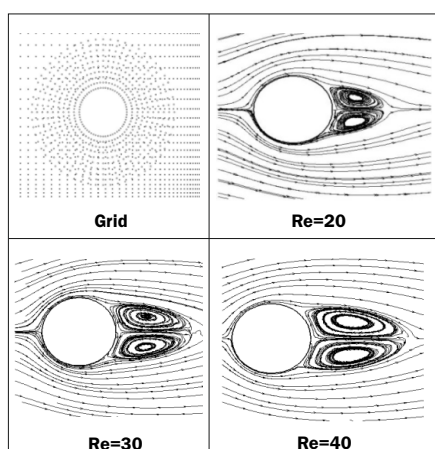
Complex Incompressible Flow Problems

2

Incompressible Flow Solver using Least Square based Artificial Compressibility Method

Mihir Chatterjee*

Chemical Technology Division, Chemical Technology Group, Bhabha Atomic Research Centre (BARC), Trombay – 400085, INDIA



Chimera grid used for computation and streamline plot for flow past a circular cylinder at different Reynolds numbers

ABSTRACT

The objective of the present work is to develop a meshless method based on least square to solve incompressible Navier-Stokes equations. The meshless method based on least square discretization depends on the arbitrary distribution of points called a cloud of points. It requires connectivity and neighbourhood information for every point in the cloud. This study is aimed at applying an upwind differencing scheme in conjunction with the pseudo-compressibility method in meshless framework. Recently meshless methods for several compressible flow algorithms have gained popularity. All meshless numerical methods share a standard feature that no mesh is needed and the solver is capable of operating on an arbitrary distribution of points. For a multibody configuration, clouds of points are generated around every part or component of the body and these clouds around components are then merged to get a distribution of points around it. For completing numerical simulation of Navier-Stokes equations for complex multibody configuration, the generation of an appropriate grid becomes the most difficult job. The pseudo or artificial compressibility method was first introduced by Chorin [1] for solving complex incompressible flow problems. During this formulation, a time derivative of pressure is added to the continuity equation, along with the momentum equations, these form a hyperbolic system of equations, which may be marched in pseudo-time to a steady-state solution. In the present work, an attempt has been made to use the Artificial Compressibility Method (ACM) with meshless least square based discretisation for solving incompressible Navier-Stokes equations. The central idea behind this work is to solve incompressible flow problems using an arbitrary distribution of points or clouds constructed around a geometry applying any available method of grid generation. The advantage of this least square based meshless pseudo-compressibility method is that it is often used to solve incompressible flow problems around complex geometry where the task of grid generation can be simplified by the generation of a cloud of points around the body and their connectivity information.

KEYWORDS: Navier-Stokes equations, Artificial Compressibility Method

Introduction

In this paper, least square based meshfree method is used to solve incompressible Navier Stokes equations using the Kinetic theory approach motivated by ACM. ACM was first introduced by Chorin [1] and has been used extensively with much success by Kwak and Kiris [2] for solving complex incompressible flow problems. In this formulation, a time derivative of pressure is added to the continuity equation. Together with the momentum equations, these form a hyperbolic system of equations, which can be marched in pseudo-time to a steady-state solution. The method can also be extended to solve time-dependent problems by using sub-iterations in pseudo time at every physical time step to ensure divergence-free velocity field. If only steady state solution to a problem is required, ACM can be a very efficient formulation because it does not require that divergence-free velocity field be obtained at each iteration but only as the solution converges. Hence ACM is a macroscopic incompressible Navier Stokes (NS) solution method. The addition of the time derivative of pressure to the continuity equation creates a hyperbolic system of equations complete with artificial

pressure waves of finite speed. When the solution converges to a steady state, a divergence-free flow field is obtained. Hence many of the well-developed compressible flow algorithms can be utilized for this method.

Ohwada and Asinari [3] have shown the role of kinetic theory in the numerical methods for the Navier-Stokes equation (both compressible and incompressible) with the theory of characteristics for the kinetic equation. They have discussed the relation between ACM and Lattice Boltzmann Method (LBM), which is a kinetic-based method. LBM employs the evolution of microscopic gas models to approximate macroscopic equations of fluid dynamics, as shown by Banda et. al. [4] that yields the solution of Incompressible Navier Stokes Equation (INSE) in the limit $Kn \sim Ma \sim h \rightarrow 0$ while only the limit $Ma \sim h \rightarrow 0$ suffices for ACM. Chatterjee et. al. [5] have used a normal equation approach for incompressible fluid flow using the modified Artificial Compressibility Method (ACM) of Chorin [1] with the least square based discretisation. The present method is based on the principle of Kinetic Theory and ACM using the meshless Kinetic upwind method as adapted by Mahendra et. al. [6]. The main aim of this work is to develop a robust meshfree incompressible flow solver based on kinetic theory.

*Author for Correspondence: Mihir Chatterjee
E-mail: mihir@barc.gov.in

Numerical Methods

Golse [7] has given the detailed derivation of Incompressible Navier-Stokes equations from the renormalized solutions of the Boltzmann equation. In the present case incompressibility condition is being simulated by choice of distribution function. Consider the Boltzmann equation with Bhatnagar-Gross-Kook (BGK) model as

$$\frac{\partial f}{\partial t} + \vec{v} \cdot \frac{\partial f}{\partial \vec{x}} = J_m(f, f_0) = -\frac{(f - f_0)}{t_r} \quad \text{Eqn.1}$$

where f_0 is the Maxwellian. This equation can also be written in a non-dimensional form as

$$St \left[\frac{\partial f}{\partial t} + \vec{v} \cdot \frac{\partial f}{\partial \vec{x}} \right] = -\frac{1}{Kn_L} \frac{(f - f_0)}{\hat{t}_r} \quad \text{Eqn.2}$$

Where $\hat{t}_r = t_r v_{th} / \lambda$ and t_r is the dimensionless relaxation time, $v_{th} = 1/\sqrt{\beta}$ is most probable molecular thermal speed. The dimensionless form contains Strouhal number, $St = L_0/t_0 v_{th}$ and local Knudsen number, $Kn_L = \lambda/L_0$ is defined as the ratio of mean free path, λ and length scale, L_0 .

The distribution function f for simulation of ACM can be expressed as

$$f = \left(\frac{\rho}{\delta}\right) \left(\frac{\beta}{\pi}\right)^{D/2} \exp(-\beta(\vec{v} - \vec{u})^2) \quad \text{Eqn.3}$$

Where D is the degrees of freedom and pressure p is related to artificial density ρ by the artificial equation of state where δ is the artificial compressibility parameter

$$p = \delta \rho \quad \text{Eqn.4}$$

Now after taking moment we get a set of INSE in Cartesian coordinates.

$$\frac{\partial}{\partial \tau} (U) + \frac{\partial}{\partial x} (GX_x + GX_y) + \frac{\partial}{\partial y} (GY_x + GY_y) = 0 \quad \text{Eqn.5}$$

where,

$$U = \begin{bmatrix} p' \\ u \\ v \end{bmatrix}, GX_x = \begin{bmatrix} \delta u \\ u^2 + p' \\ uv \end{bmatrix}, GX_y = \begin{bmatrix} \delta v \\ uv \\ v^2 + p' \end{bmatrix}, GX_v = \begin{bmatrix} 0 \\ \tau_{xx} \\ \tau_{xy} \end{bmatrix}, GY_v = \begin{bmatrix} 0 \\ \tau_{yx} \\ \tau_{yy} \end{bmatrix} \quad \text{Eqn.6}$$

and p' is the pressure normalized with density. GX_x and GX_y are the x and y component of inviscid flux while GX_v and GY_v are the x and y components of viscous flux respectively. This can be interpreted in a formulation similar to the ACM due to Chorin[1], the continuity equation for incompressible flow is modified by adding a time-derivative of pressure term resulting in:

$$\frac{1}{\delta} \frac{\partial p}{\partial t} + \left(\frac{\partial u}{\partial x} + \frac{\partial v}{\partial y} \right) = 0 \quad \text{Eqn.7}$$

As t no longer represents a true physical time in this formulation, now onwards it is replaced with τ that is an auxiliary variable whose role is analogous to that of time in a compressible flow problem. Hence along with x and y momentum equations (Eqn.9) and (Eqn.10), the modified continuity equation (Eqn.8) forms a hyperbolic system of equations.

$$\frac{1}{\delta} \frac{\partial p}{\partial \tau} + \left(\frac{\partial u}{\partial x} + \frac{\partial v}{\partial y} \right) = 0 \quad \text{Eqn.8}$$

$$\frac{\partial u}{\partial \tau} + \frac{\partial}{\partial x} (p' + uu) + \frac{\partial}{\partial y} (uv) + \frac{\partial}{\partial x} \tau_{xx} + \frac{\partial}{\partial y} \tau_{yx} = 0 \quad \text{Eqn.9}$$

$$\frac{\partial v}{\partial \tau} + \frac{\partial}{\partial x} (uv) + \frac{\partial}{\partial y} (p' + vv) + \frac{\partial}{\partial x} \tau_{xy} + \frac{\partial}{\partial y} \tau_{yy} = 0 \quad \text{Eqn.10}$$

Where,

$$\tau_{xx} = -2\nu \frac{\partial u}{\partial x}, \tau_{yy} = -2\nu \frac{\partial v}{\partial y}, \tau_{xy} = \tau_{yx} = -\nu \left(\frac{\partial u}{\partial y} + \frac{\partial v}{\partial x} \right) \quad \text{Eqn.11}$$

In this formulation the Reynolds stress has been approximated as a function of the strain rate tensor, and thus ν represents a sum of the kinematic viscosity and the turbulent eddy viscosity.

Least Square Based Discretization

The present work uses least squares-based discretization due to Ghosh and Deshpande [8], which is a meshless or grid free method. In case of finite difference methods, the above equation is solved by discretizing the various derivatives along the co-ordinate directions. Finite volume method is based on integral form of governing equations. However, if we are given an arbitrary distribution of points without any grid structure associated with these points, it will be difficult to discretize the derivatives. With the least square approach, spatial derivatives f_x, f_y of a function f can be discretized in terms of the data at the neighboring points or nodes. If we consider arbitrary n points (in general it has been observed, for a 2D or 3D calculation a minimum of two neighboring nodes per quadrant are required for the least square based discretization) surrounding a point P_0 as shown in Fig.1.

The Taylor series around P_0 for any quantity f gives us $\Delta f_i = \Delta x_i f_{x_0} + \Delta y_i f_{y_0} + \text{h.o.t.}$ $i=1 \dots n$, h.o.t. = higher order terms where $\Delta x_i = x_i - x_0, \Delta y_i = y_i - y_0$ and $\Delta f_i = f_i - f_0$. Minimizing the square of error E , defined by

$$E = \sum_{i=1}^n (\Delta f_i - \Delta f_{x_0} \Delta x_i - \Delta f_{y_0} \Delta y_i)^2 \quad \text{Eqn.12}$$

gives the following first order accurate least square formulae for the gradients

$$f_{x_0}^{(1)} = \frac{\sum \Delta y_i^2 \sum \Delta x_i \Delta f_i - \sum \Delta x_i \Delta y_i \sum \Delta y_i \Delta f_i}{\sum \Delta x_i^2 \sum \Delta y_i^2 - (\sum \Delta x_i \Delta y_i)^2} \quad \text{Eqn.13}$$

$$f_{y_0}^{(1)} = \frac{\sum \Delta x_i^2 \sum \Delta y_i \Delta f_i - \sum \Delta x_i \Delta y_i \sum \Delta x_i \Delta f_i}{\sum \Delta x_i^2 \sum \Delta y_i^2 - (\sum \Delta x_i \Delta y_i)^2} \quad \text{Eqn.14}$$

where Σ represents the summation over all points in the neighborhood $N(P_0)$ of P_0 . The formulae given in (Eqn. 13) and (Eqn. 14) can now be used to obtain the point values of f_{x_0} and f_{y_0} throughout the field with incorporation of upwinding.

Incorporation of Upwind Scheme

In the present work upwinding is enforced in least square based discretization method by stencil subdivision. Consider a 2-D linear hyperbolic partial differential equation for scalar f .

$$\frac{\partial f}{\partial t} + v_1 \frac{\partial f}{\partial x} + v_2 \frac{\partial f}{\partial y} = 0 \quad \text{Eqn.15}$$

The exact solution to this equation is given by

$$f(t + \Delta t, x, y, v_1, v_2) = f(t, x - v_1 \Delta t, y - v_2 \Delta t, v_1, v_2) \quad \text{Eqn.16}$$

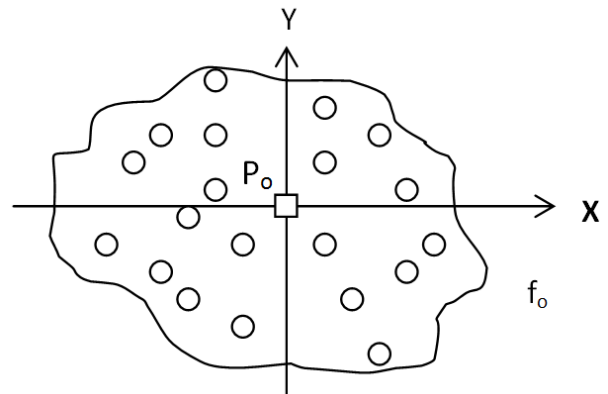


Fig.1: Typical connectivity around point P_0 .

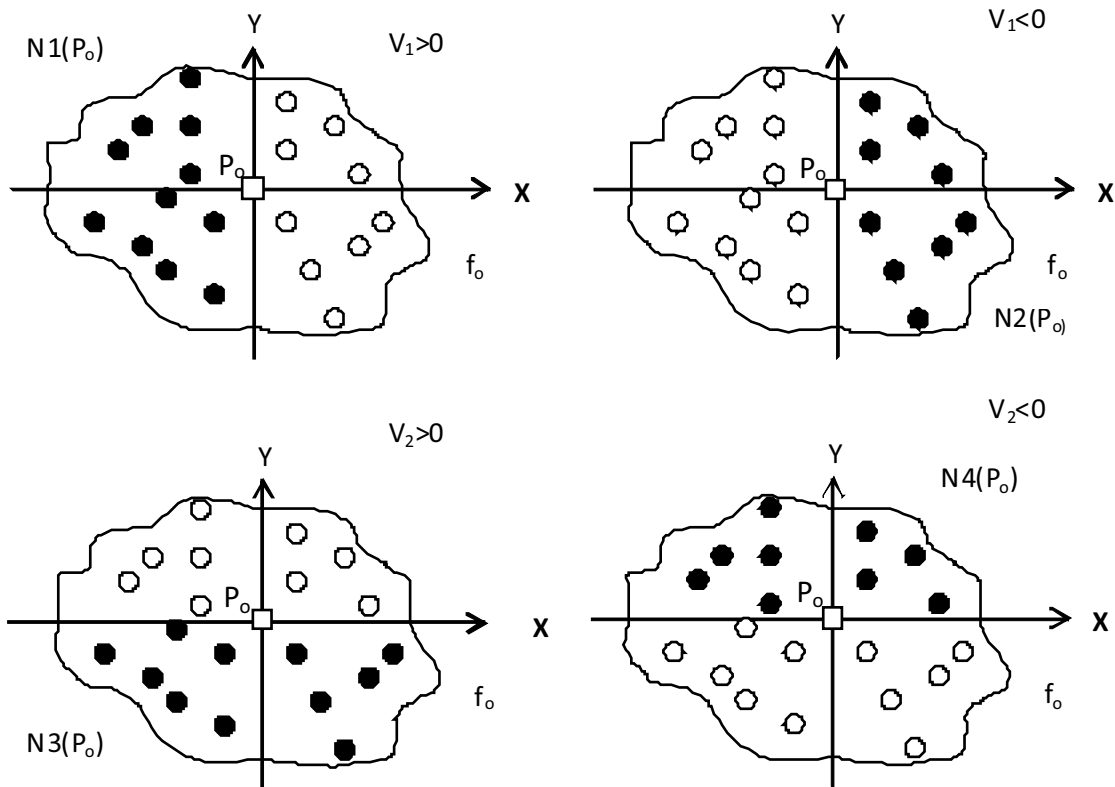


Fig.2: Stencil splitting for Upwinding.

The propagation of information to node P_o depends upon location of node P_i relative to P_o and the signs of v_1 and v_2 . If $v_1 > 0$ then only the nodes to the left of P_o will influence the solution at P_o . Similarly, if $v_1 < 0$ then only the nodes to the right of P_o will influence the solution at P_o . Similar arguments show that for $v_2 > 0$ the node below P_o and for $v_2 < 0$ the node above P_o will influence the solution at P_o . For developing any upwind scheme this signal propagation property should be considered. Now replacing the spatial derivative in (Eqn.15) by discrete least square approximation we get

$$\frac{\partial U}{\partial t} + \frac{v_1 + |v_1|}{2} \{f_{x_0}\}_{N1(P_o)} + \frac{v_1 - |v_1|}{2} \{f_{x_0}\}_{N2(P_o)} + \frac{v_2 + |v_2|}{2} \{f_{y_0}\}_{N3(P_o)} + \frac{v_2 - |v_2|}{2} \{f_{y_0}\}_{N4(P_o)} = 0 \quad \text{Eqn.17}$$

Where coefficient $\frac{v_1 + |v_1|}{2}$ of the term $\{f_{x_0}^{(1)}\}_{N1(P_o)}$ which appears in (Eqn.17) is always positive for $v_1 > 0$, while it is zero for $v_1 < 0$. This indicates that least square evaluation of derivative

at node P_o for $v_1 > 0$ should use data at nodes to the left of P_o i.e. based on stencil $N1(P_o)$ and is represented as $\{f_{x_0}^1\}_{N1(P_o)}$ for $v_1 > 0$, $\{f_{x_0}^1\}_{N2(P_o)}$ for $v_1 < 0$, $\{f_{y_0}^1\}_{N3(P_o)}$ for $v_2 > 0$, $\{f_{y_0}^1\}_{N4(P_o)}$ for $v_2 < 0$.

Therefore, based on first order least square update formulation we get the final state update formula for artificial compressibility as follows

$$U^{n+1} = U^n - \Delta\tau \left[\begin{aligned} &\frac{v_1 + |v_1|}{2} \left\{ \frac{\partial GX}{\partial x} \right\}_{N1(P_o)} + \frac{v_1 - |v_1|}{2} \left\{ \frac{\partial GX}{\partial x} \right\}_{N2(P_o)} \\ &+ \frac{v_2 + |v_2|}{2} \left\{ \frac{\partial GY}{\partial y} \right\}_{N3(P_o)} + \frac{v_2 - |v_2|}{2} \left\{ \frac{\partial GY}{\partial y} \right\}_{N4(P_o)} \end{aligned} \right] \quad \text{Eqn.18}$$

Where,

$$\left\{ \frac{\partial (GX)}{\partial x} \right\}_{N1(P_o)} = \left[\frac{\sum_i \Delta y_i^2 \sum_i \Delta x_i \Delta (GX)_i^n - \sum_i \Delta x_i \Delta y_i \sum_i \Delta y_i \Delta (GX)_i^n}{\sum_i \Delta x_i^2 \sum_i \Delta y_i^2 - (\sum_i \Delta x_i \Delta y_i)^2} \right]_{\in N1(P_o)} \quad \text{Eqn.19}$$

$$\left\{ \frac{\partial (GX)}{\partial x} \right\}_{N2(P_o)} = \left[\frac{\sum_i \Delta y_i^2 \sum_i \Delta x_i \Delta (GX)_i^n - \sum_i \Delta x_i \Delta y_i \sum_i \Delta y_i \Delta (GX)_i^n}{\sum_i \Delta x_i^2 \sum_i \Delta y_i^2 - (\sum_i \Delta x_i \Delta y_i)^2} \right]_{\in N2(P_o)} \quad \text{Eqn.20}$$

$$\left\{ \frac{\partial (GY)}{\partial x} \right\}_{N3(P_o)} = \left[\frac{\sum_i \Delta x_i^2 \sum_i \Delta y_i \Delta (GY)_i^n - \sum_i \Delta x_i \Delta y_i \sum_i \Delta x_i \Delta (GY)_i^n}{\sum_i \Delta x_i^2 \sum_i \Delta y_i^2 - (\sum_i \Delta x_i \Delta y_i)^2} \right]_{\in N3(P_o)} \quad \text{Eqn.21}$$

$$\left\{ \frac{\partial (GY)}{\partial x} \right\}_{N4(P_o)} = \left[\frac{\sum_i \Delta x_i^2 \sum_i \Delta y_i \Delta (GY)_i^n - \sum_i \Delta x_i \Delta y_i \sum_i \Delta x_i \Delta (GY)_i^n}{\sum_i \Delta x_i^2 \sum_i \Delta y_i^2 - (\sum_i \Delta x_i \Delta y_i)^2} \right]_{\in N4(P_o)} \quad \text{Eqn.22}$$

where $\Delta(GX) = (GX)_i - (GX)_j$ and $\Delta(GY) = (GY)_i - (GY)_j$, and $GX (=GX_i + GX_j)$ and $GY (=GY_i + GY_j)$ represent the split fluxes for incompressible flow.

Code Validation

The benchmark problem of flow past a circular cylinder and backward facing step have been chosen in the present study to validate the code. In principle, the concept of mesh-free least square-based discretization works well for “any mesh” system, in which the nodes can be either regularly or irregularly distributed. This provides the present mesh free method geometric flexibility.

Flow Past Circular Cylinder

The nodes in the neighborhood of the circular cylinder are generated under the cylindrical coordinate system as shown in Fig.3a. This cylindrical mesh is fused with an underlying Cartesian mesh and a Chimera grid is appropriately generated. In the present study, we have performed numerical simulation at a series of Reynolds number from 20 to 40 with various flow patterns in the steady state. In all cases, a pair of vortices develop behind the cylinder and is perfectly aligned as

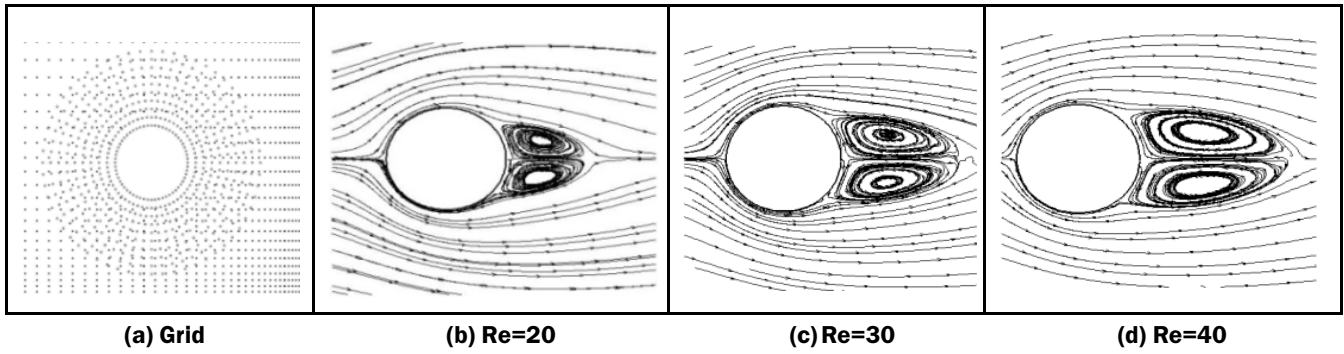


Fig.3: Chimera grid used for computation and streamline plot for flow past a circular cylinder at different Reynolds numbers.

shown in Fig.3 for different Reynolds number. This is consistent with the experimental observation.

Some quantitative parameters for the re-circulating region, such as the length of the re-circulating region L_{sep} , from the rearmost point of the cylinder to the end of the wake, separation angle θ_{sep} are shown in the Fig.4. The results from the present calculation as well as the result of the other researchers are listed in table 1 for the test case of Reynolds number of 20 and 40. Here C_d is the drag coefficient. All these flow parameters agree well with the results of previous studies for the Reynolds number studied.

Backward Facing Step Problem

Fluid flows in channels with flow separation and reattachment of the boundary layers are encountered in many flow problems like heat exchangers and ducts. Among this type of flow problems, a backward facing step can be regarded as having a simple geometry while retaining rich flow physics manifested by flow separation, flow reattachment and multiple recirculating zones in the channel depending on the Reynolds number. The geometrical parameters are step height, channel height and channel length. This problem has been used as a validation test case. The challenge in modelling this problem comes from the fact that the sizes of the separation zones downstream of the step are very sensitive to the pressure gradient in the flow, especially when the boundary layer is separated. If separation is present, a pressure wave traveling with finite speed will cause a change in the local pressure gradient, which will affect the location of the flow separation. It has been observed that this change in separated flow will cause a feed back to the pressure field, possibly preventing convergence to a steady state. The geometry used in the calculation is shown in Fig.5, where 's' is the height of the step. The entrance channel width is equal to the step height and its length is double the step height. The total length of the channel from the step is 30s.

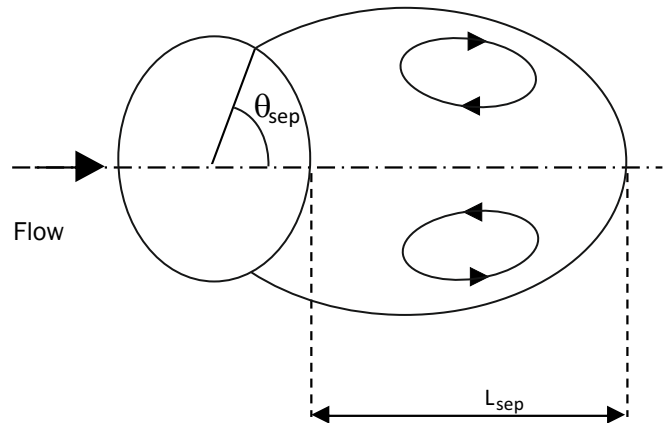


Fig.4: Characteristic parameters of the cylinder wake.

In a very important study Yee et al. [13] observed the spurious behavior of the numerical schemes. They showed that for backward facing step flow when a coarse grid mesh is used, one can obtain a spurious oscillating numerical solution. Erturk [14] have reported that when a finer mesh was used, the oscillating behavior of the numerical solution disappeared and it was possible to obtain a steady solution. They stated that when finer grids are used, the Mesh Reynolds number defined as $Re_m = u\Delta h/\nu$ decreases and this improves the numerical stability characteristics of the numerical scheme used, and allows high Reynolds number flows computable. In the present study, a fine unstructured mesh is used in order to obtain steady state numerical solutions. A part of the unstructured grid used for computation is shown in Fig.6.

At the inflow boundary, it is assumed that the flow is fully developed plane Poiseuille flow between parallel plates such that a parabolic velocity profile is prescribed throughout the calculation, and the static pressure is allowed to change. No

Table 1: Comparison of parameters for flow past circular cylinder.

Source	Re=20			Re=40		
	L_{sep}	q_{sep}	C_d	L_{sep}	q_{sep}	C_d
Dennis and Chang [9]	0.94	43.7	2.05	2.35	53.8	1.522
Takami and Keller [10]	0.935	43.7	2.05	2.32	53.6	1.536
Tuann and Olson [11]	0.9	44.1	2.25	2.1	54.8	1.675
Ding et. al. [12]	0.93	44.1	2.18	2.20	53.5	1.713
Present	0.94	43.7	2.08	2.11	54.4	1.795



Fig.5: Outline of the backward facing step problem.

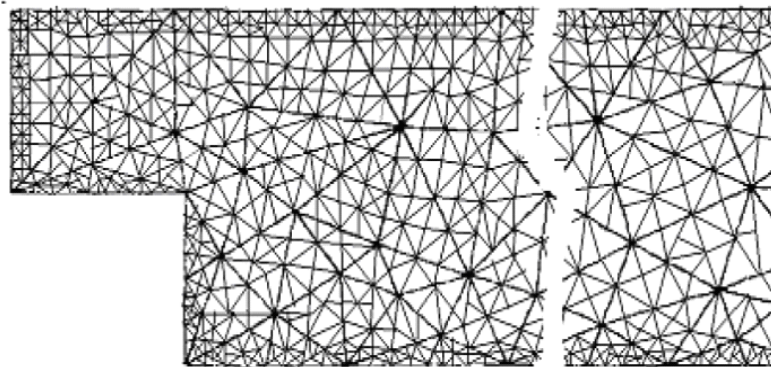


Fig.6: Outline of the backward facing step problem.

slip boundary condition is prescribed at the top and bottom wall. Two step heights downstream from the inflow a two to one expansion is encountered. The outflow boundary extends to 30 step heights downstream of the step. At this exit boundary a outflow boundary condition has been used. The flow was calculated using a grid of total 24600 points. The grid is unstructured and clustered near the side boundary for better resolution of the flow features to be captured.

The streamline plots for different Reynolds numbers are shown in Fig.7. It is observed from the plots that as the Reynolds number increases the length of the primary separation zone x_1 also increases. At Reynolds number = 400 a secondary separation zone has been developed at the top wall boundary.

A set of experimental and numerical solutions found in the literature has been compared with the present computational result in order to demonstrate the accuracy of the present numerical solutions. Armaly et al. [15] have experimentally obtained the u -velocity profile at several x -locations (plotted as a fraction of the total length of the configuration S , i.e x/S) for Reynolds number $Re=100$ for a backward facing step. For the same geometry a numerical solution for a steady two-dimensional flow is also presented by Erturk [14]. The u -velocity profiles at the corresponding x -locations drawn to the same scale for this experimental and computed results are shown in the figure 8 and are compared with u -velocity profiles at the same x locations from the simulation with the present method. From Fig.8 it can be seen that the present computed velocity profiles agree well (except at the immediate downstream of the step) with that of experimental results of Armaly et al. [15] and numerical result of Erturk [14]. The difference at the flow separation zone is attributed to the feedback effect of pressure wave.

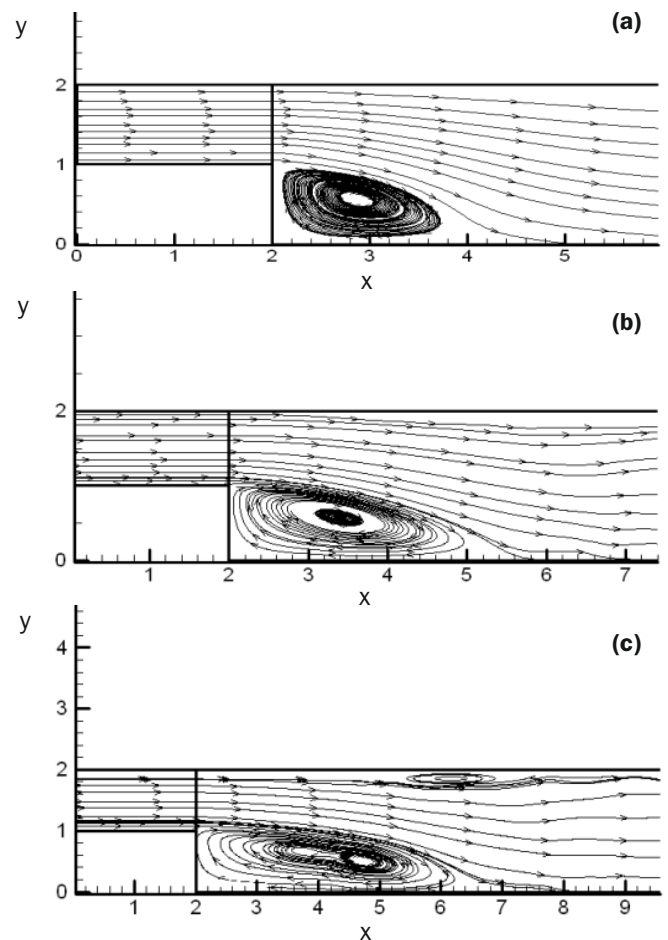


Fig.7: Streamline plot for flow over a backward facing step at Reynolds number a.100 b.200 and c.400.

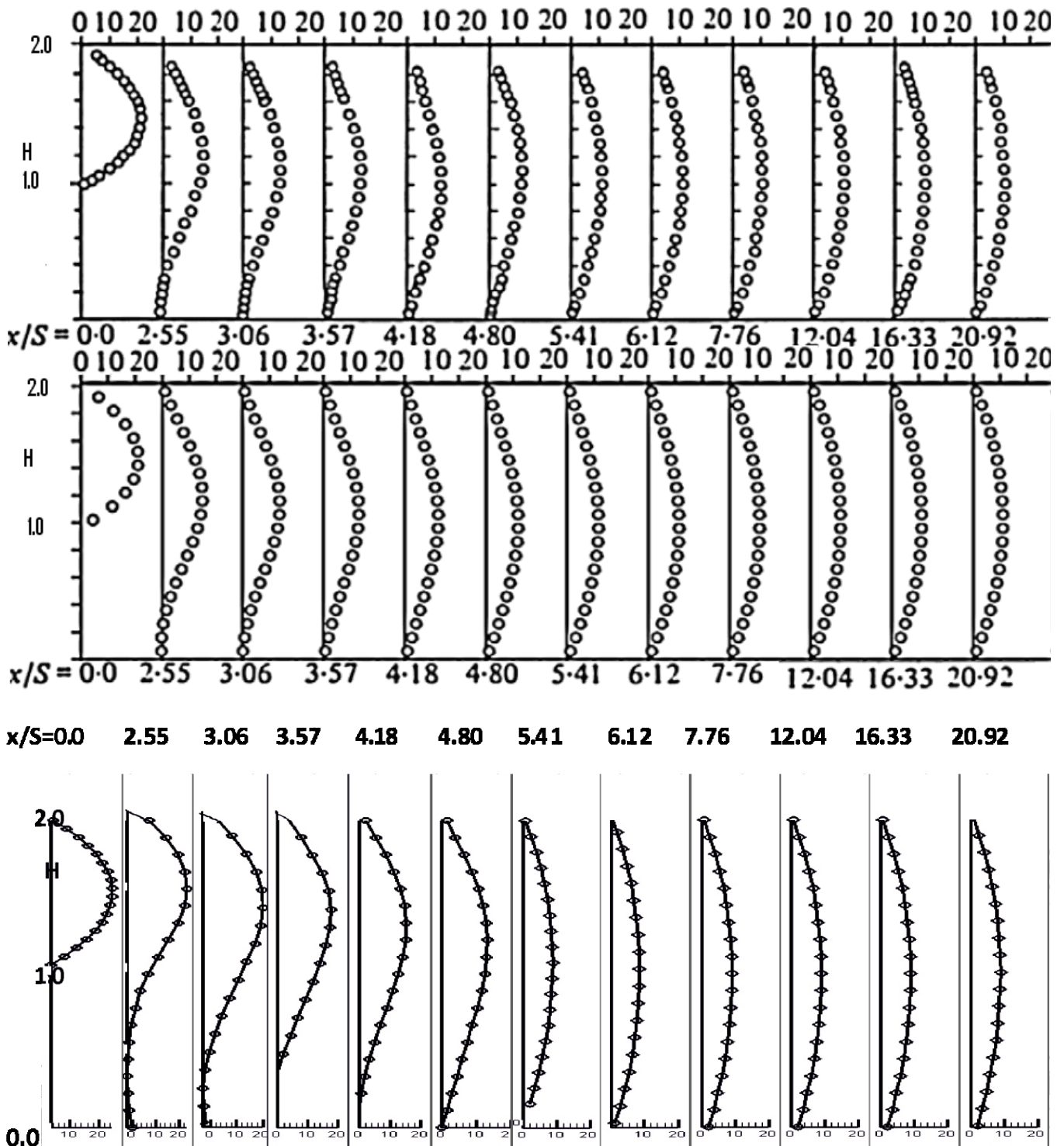


Fig.8: *u*-velocity profiles at various downstream locations for $Re=100$; Top figure Armaly et.al [15], middle figure Erturk [14], bottom figure present study.

Conclusions

A Kinetic Upwinding theory-based approach motivated by the Artificial Compressibility Method for the solution of the incompressible Navier-Stokes equations using meshfree least square based discretization has been developed. Numerical simulations were carried out for two incompressible benchmark flow problems. The obtained numerical results agree well with the results published in literature.

Acknowledgements

The author acknowledges the requisite technical support provided by M. S. Deshpande, Head, Chemical Technology Division (ChTD), BARC; Vinay Kumar, Scientific Officer (G), ChTD and Chandrajit Singh Chauhan, Scientific Officer (D), ChTD.

References

[1] Chorin A. J. “Numerical Solution of the Navier-Stokes Equations”, *Mathematics and Computers*, 22(1968), 742-762.

[2] Kwak D., Kiris C. “Computational Challenges of Viscous incompressible Flows”, *Computers and Fluids*, 34(2005) 283-299.

[3] Ohwada T, Asinari P., “Artificial Compressibility Method Revisited, Asymptotic Numerical Method for Incompressible Navier-Stokes Equations”, *Journal of Computational Physics*, 229(5)(2010)1698-1723.

[4] Banda M. K., Junk M., Klar A. “Kinetic-based Numerical Schemes for Incompressible Navier–Stokes Equations”, *Computers and Fluids*, 35(2006)879–887.

[5] Chatterjee M., Mahendra A. K., Sanyal A., Gouthaman G, “A Mesh Free Method for Simulations of Incompressible Fluid Flow”, *Computer Modeling in Engineering & Sciences*, 83 (4)(2012)385-402.

[6] Mahendra A. K., Singh R. K., Gouthaman G, “Meshless Kinetic Upwind Method for Compressible, Viscous Rotating Flows”, *Computers and Fluids*, 46(1)(2010)325-332.

[7] Golse F. “From the Boltzmann Equation to the Incompressible Navier-Stokes Equations”, *Proceedings of Symposia of Applied Mathematics*, 65(2007)355-366.

[8] Ghosh A. K., Deshpande S. M., “Least Squares Kinetic Upwind Method for Inviscid Compressible Flows”, *AIAA Paper 95 (1995)*, 1001-1011.

[9] Dennis S. C. R., Chang G. Z., “Numerical Solutions for Steady Flow Past a Circular Cylinder at Reynolds Number up to 100”, *Journal of Fluid Mechanics*, 42(1970)471-489.

[10] Takami H., Keller H. B., “Steady Two-dimensional Viscous Flow of an Incompressible Fluid Past a Circular Cylinder”, *Physics of Fluids 12 (Suppl II) (1969)II-51-63*.

[11] Tuann S. Y.; Olson M. D., “Numerical Studies of the Flow around a Circular Cylinder by a Finite Element Method”, *Computers and Fluids*, 6(1978) 219-240.

[12] Ding H., Shu C., Yeo K. S., Xu D., “Simulation of Incompressible Viscous Flows Past a Circular Cylinder by Hybrid FD Scheme and Meshless Least Square-based Finite Difference Method” *Computer Methods in Applied Mechanical Engineering*, 193(2004)727-744.

[13] Yee H. C., Torezyski J. R., Mortan S. A., Visbal M. R., “On Spurious Behavior of CFD Simulations”, *International Journal for Numerical Methods in Fluids*, 30 (1999)675-711.

[14] Erturk E., “Numerical Solutions of 2-D Steady Incompressible Flow over a Backward-Facing Step, Part I: High Reynolds Number Solutions”, *Computers and Fluids*, 37 (2008) 633-655.

[15] Armaly B. F., Durst F., Periera J. C. F., Schonung B., “Experimental and Theoretical Investigation of Backward-facing Step Flow”, *Journal of Fluid Mechanics*, 127(1983)473-496.

Notations		
Symbol	Description	Unit
β	$M/2RT$	s^2/m^2
δ	Artificial compressibility parameter	Pa. m^3/Kg
Δf_i	$f_i - f_o$	-
Δx_i	$x_i - x_o$	m
Δy_i	$y_i - y_o$	m
θ_{sep}	Separation angle	Degree
λ	Mean free path	m
τ_{ij}	Components of shear stress on the i^{th} plane in j^{th} direction	Pa
ρ	Artificial density	Kg/m^3
τ	Pseudo time	-
ν	Sum of the kinematic viscosity and the turbulent eddy viscosity	m^2/s
C_d	Dimensionless Drag coefficient	-
D	Degrees of freedom	-
E	Error	-
f	Distribution function for ACM	-
f_o	Maxwellian probability distribution function	-
$f_{x_o}^{(1)}$	First order accurate least square formula for x derivative of function f at point P_o	-
$f_{y_o}^{(1)}$	First order accurate least square formula for y derivative of function f at point P_o	-
$G X_I$	x component of inviscid flux	-
$G X_V$	x component of viscous flux	-
$G Y_I$	y component of inviscid flux	-
$G Y_V$	y component of viscous flux	-
h	Mesh spacing	m
Kn	Dimensionless Knudsen Number	-
L_c	Length scale	m
L_{sep}	Length of the re-circulating region	m
Ma	Dimensionless Mach Number	-
p	Pressure	Pa
R	Universal gas Constant	$J/(K.mole)$
Re	Dimensionless Reynolds Number	-
s	Step height	m
S	Total length of backward facing step configuration	m
St	Dimensionless Strouhal number	-
t	Time	s
T	Temperature in absolute scale	K
t_R	Dimensionless relaxation time	-
u	x component of velocity	m/s
U	State vector	-
v	y component of velocity	m/s
v_{th}	Most probable molecular thermal speed	m/s

CFD Modeling

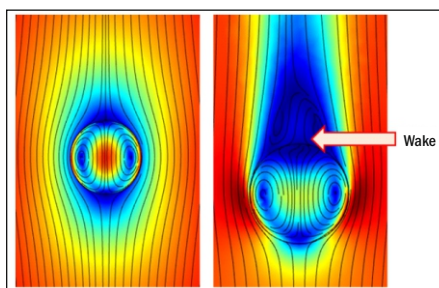
3

CFD Modeling of Fundamental Phenomena Relevant to Solvent Extraction: An Overview

K. K. Singh^{*1,2}, R. K. Chaurasiya^{1,2}, S. Sarkar^{1,2}, N. Sen^{1,2} and S. Mukhopadhyay^{1,2}

¹Chemical Engineering Division, Bhabha Atomic Research Centre (BARC), Trombay – 400085, INDIA

²Homi Bhabha National Institute, Anushaktinagar, Mumbai, – 400094, INDIA



Streamlines inside and outside the drop at $Re_p = 0.289$ (left) and, $Re_p = 254$ (right)

ABSTRACT

Solvent extraction is the most important separation process in the nuclear fuel cycle. Different types of solvent extraction equipment are used in different processes used for separation and purification of nuclear materials. Detailed insights into liquid-liquid two-phase flow and mass transfer phenomena are needed for efficient design of solvent extraction equipment to achieve process intensification. CFD modeling of solvent extraction is increasingly being used to have such detailed insights. In equipment-level CFD modeling, the governing equations that need to be solved require appropriate closure equations. These closure equations, such as the equations to estimate drag coefficient or mass transfer coefficient, are usually empirical in nature. Thus, accuracy of equipment-level CFD models depends on the accuracy of the closure equations. To reduce the empiricism in equipment-level CFD models, the closure equations can be obtained in a more fundamental manner by carrying out droplet-level CFD modeling of underlying phenomena. This article provides an overview of CFD modeling of different phenomena relevant to solvent extraction targeted at generation of CFD-based closure equations. The article also provides an overview of CFD modeling of fundamental phenomena relevant to microfluidic solvent extraction which is being explored for intensification of solvent extraction processes.

KEYWORDS: Breakage, CFD, Coalescence, Drag, Drop, Microfluidics, Slug, Solvent Extraction

Introduction

Solvent extraction plays a very important role in the nuclear fuel cycle starting from production of nuclear pure uranium from its ore to spent nuclear fuel reprocessing. The processes for production of other nuclear materials such as zirconium, thorium etc. also involve solvent extraction as the key processing step [1,2]. Depending upon specific process requirements, different solvent extraction equipment such as mixer-settler, air pulsed column, rotating disc contactor, annular centrifugal extractor are used for carrying out solvent extraction. These equipment basically differ in the mode of providing energy to generate liquid-liquid dispersion to ensure fast mass transfer. However, the similarity in their functioning is that all involve liquid-liquid two-phase turbulent flow, breakage and coalescence of droplets, and interphase mass transfer. Owing to the complexity of the phenomena prevalent inside solvent extraction equipment, the approach to design solvent extraction equipment has been based on experimentation at bench-scale, pilot-scale setups and using empirical correlations reported in literature over the years [3]. This design approach leads to equipment having high design margins. With more and more thrust being given on process intensification, it is necessary to design efficient contactors with bare minimum design margins. However, this makes a thorough and fundamental understanding of the functioning of the equipment a prerequisite.

Computational Fluid Dynamics (CFD) modeling is the most useful tool to understand the flow physics in solvent extraction equipment [4]. There are different levels of CFD models of solvent extraction equipment. The simplest is the one in which drop diameter is assumed to be known and uniform and CFD simulations are targeted to obtain the flow field of the continuous phase and dispersed phase and spatial distribution and average volume fraction (hold-up) of the dispersed phase. These simulations typically involve solving continuity equations and momentum equations of the two phases along with an appropriate model of turbulence. The two phases exert drag force on each other and, thus, there is a term representing interphase momentum exchange in the momentum equations of both phases. To model this term, an appropriate model for drag force is needed. The drag models typically used in CFD models are the drag models reported in literature. Most of these drag models are empirical models based on experiments conducted in simple settings such as a single solid particle settling in a quiescent liquid. The reported drag models usually do not incorporate the physics such as the effect of turbulence on drag force and effect of internal circulations inside the drop on drag force—a phenomenon which is unique to liquid-liquid flows and is not applicable for gas-liquid or solid-liquid flows. In many cases, the results obtained by using these drag models do not match with the experimental observations. This necessitates modification in drag models to ensure better match with experimental data [5]. To get rid of the two-phase CFD models from such empiricism, it is necessary to thoroughly understand the drag phenomenon

*Author for Correspondence: K.K. Singh
E-mail: kksingh@barc.gov.in

for liquid-liquid systems. With highly controlled droplet-level experiments practically ruled out, CFD modeling becomes a very important tool to understand this phenomenon. This is one of the fundamental aspects of liquid-liquid two-phase flow which needs to be understood by carrying out CFD simulations at droplet-level.

The next higher level of CFD modeling of solvent extraction equipment is CFD-PB (Computational Fluid Dynamics–Population Balance) modeling in which the assumption of constant and uniform drop diameter is done away with [6]. The drop diameter is estimated by solving population balance equations along with flow equations. The population balance equations consider convective and dispersive transport of drops, breakage and coalescence of drops. The terms corresponding to breakage and coalescence of drops appear as source or sink terms in the population balance equations. The mathematical description of these terms requires breakage and coalescence kernels. The breakage and coalescence kernels reported in literature are empirical or semi-empirical in nature. Thus, the results of CFD-PB simulations depend on selection of the breakage, coalescence kernels and the constants therein [7]. To rid of the CFD-PB models from empiricism, the empirical or semi-empirical breakage, coalescence kernels should be replaced with fundamentally obtained breakage and coalescence kernels for which CFD simulations dedicated to study breakage and coalescence phenomena under different types of flow fields are required. Thus, study of breakage and coalescence is yet another fundamental aspect that must be studied separately to reduce empiricism in equipment-level CFD-PB models.

The ultimate objective of CFD modeling of solvent extraction equipment is to predict their mass transfer performance. To predict mass transfer, a CFD model which solves species transport equations in both phases along with flow and population balance equations should be used. Such a model is computationally very expensive and in literature only very few such studies have been reported [8]. The other way to predict mass transfer performance is by using axial dispersion model in which the inputs of hydrodynamics variables may come from empirical correlations or from the results of CFD simulations [9,10]. In either approach of mass transfer modeling, an appropriate model to estimate mass transfer coefficient for interphase mass transfer is needed. The models reported to estimate mass transfer coefficient are once again empirical in nature [11]. To reduce empiricism in mass transfer modeling, the mass transfer coefficient should be estimated from fundamental principles. Thus, using CFD models to understand interphase mass transfer for a single drop or a couple of drops and utilizing the resulting data to obtain CFD-based mass transfer coefficient models for use in equipment-level CFD models is necessary.

Of late, there has been significant research on microfluidic solvent extraction. Carrying out microfluidic solvent extraction leads to process intensification and can be used for variety of applications in the field of solvent extraction including extraction of radionuclides [12,13]. In microfluidic solvent extraction, two flowing immiscible liquid phases are brought into contact at a microfluidic junction. Depending on the flow rates of the phases, their physical properties and the design of microfluidic junction, different kinds of flow patterns may result. Slug flow, droplet flow, core-annular flow, parallel flow are some of the typical flow patterns which are obtained in microfluidic solvent extraction. The flow pattern which is likely to result when two immiscible flowing liquids are contacted at a microfluidic junction, the size of the dispersed phase (slug size,

droplet size), their velocities in the microchannels and interphase mass transfer coefficients are the aspects relevant to microfluidic extraction which need to be understood [14,15]. CFD modeling can be carried out to investigate and understand these aspects of microfluidic solvent extraction.

In this article, we intend to give an overview of the studies which are being carried out at Chemical Engineering Division, BARC to use CFD modeling to understand the above-mentioned fundamental aspects relevant to solvent extraction.

CFD Modeling of Drag Phenomenon

To study the drag phenomenon in liquid-liquid systems, a single droplet surrounded by a flowing continuous phase is considered. A typical computational domain used for CFD modeling is shown in Fig. 1. It comprises a cube with a spherical drop placed at its centre. CFD simulation involves solution of Reynolds Averaged Navier-Stokes (RANS) equations in the continuous phase and Navier-Stokes equations in the drop phase. The key aspect of the modeling is capturing the effect of internal circulation inside the drop on the drag force exerted on it by the continuous phase and to capture the effect of continuous phase turbulence on drag coefficient. To capture the effect of internal circulation on drag coefficient, appropriate interfacial boundary conditions of velocity, shear stress and normal stress are required. Implementation of these interfacial boundary conditions helps capture the effect of internal circulation inside the droplet and its effect on drag force exerted by the continuous phase on the droplet. The governing equations and boundary conditions for flow simulations are described in our previous study [16].

The CFD model is validated by comparing the drag coefficient predicted by the CFD model with the drag coefficient estimated from the correlation analytical solution for creeping flow regime [17, 18]. For higher Reynolds number, validation is done by comparing drag coefficient predicted by the CFD model with drag coefficient estimated from the correlation reported by Harper and Moore [19]. The results of the validation summarized in Table 1 suggest a good agreement between the drag coefficient values predicted by the CFD model ($C_{d,CFD}$) and the same predicted by the analytical model ($C_{d,anal}$) and empirical correlation ($C_{d,corr}$). Fig. 2 shows the streamlines of internal circulation inside the drop and streamlines of the continuous phase outside the drop for two different particle Reynolds numbers. At higher particle Reynolds number, wake formation behind the drop is observed. The CFD model was further extended to estimate the effect of turbulence on drag coefficient. For this, simulations were

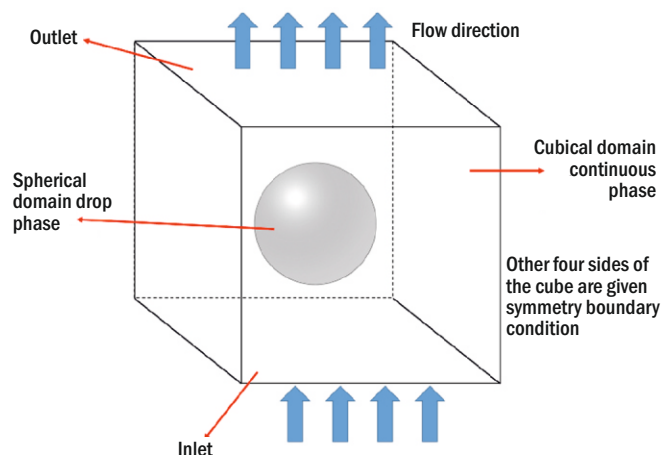


Fig.1: Typical computational domain used for CFD modeling of drag phenomenon.

carried out by introducing a source term in the equation of turbulent kinetic energy using the approach reported in literature to estimate the effect of turbulence on drag on a solid particle and a gas bubble for liquid-solid and gas-liquid systems [20,21]. The results from the CFD simulations were used to prescribe a CFD-based correlation to estimate the drag coefficient. The correlation, given by Eq. (1), has particle (drop) Reynolds number (Re_p), Kolmogorov length scale (λ), drop diameter (d) as the independent variables and predicts drag coefficient (C_d). Particle Reynolds number is defined by Eq. (2) in which ρ_c is the density of the continuous phase, μ_c is the viscosity of the continuous phase and \vec{u}_{slip} is the slip velocity between the drop and the continuous phase.

$$C_d = \frac{(d/\lambda)^3 + 1.5031 Re_p + 103.81}{0.0308 Re_p^2 - 2.0687 Re_p + 95.696} \quad (1)$$

$$Re_p = \frac{d \rho_c |\vec{u}_{slip}|}{\mu_c} \quad (2)$$

The drag coefficient correlation obtained from CFD simulations was implemented in equipment-level two-phase flow simulations of Pulsed Disc and Doughnut Column (PDDC) and a good prediction of dispersed phase holdup was obtained for different operating conditions. Thus, by replacing an empirical drag model with a CFD-based drag model, empiricism was reduced in the equipment-level CFD model. The CFD model to estimate drag coefficient is being further extended to estimate drag coefficient for concentrated liquid-liquid dispersions in which drag coefficient will depend, in addition to particle Reynolds number and Kolmogorov length scale, on dispersed phase holdup also.

Table 1: Comparison of drag coefficient obtained from CFD model with drag coefficient estimated from analytical equation/empirical correlation.

Re_p	C_{d_corr} / C_{d_anal}	C_{d_CFD}	AARE (%)
Creeping flow regime			
0.285	70.19	65.30	6.97
0.568	35.24	32.92	6.60
1.18	16.95	15.35	9.42
2.17	9.21	8.98	2.49
High Reynolds number regime			
120.86	0.46	0.50	8.98
169.20	0.39	0.41	4.88
254.30	0.30	0.33	10.42
Average Absolute Relative Error (AARE)			7.11

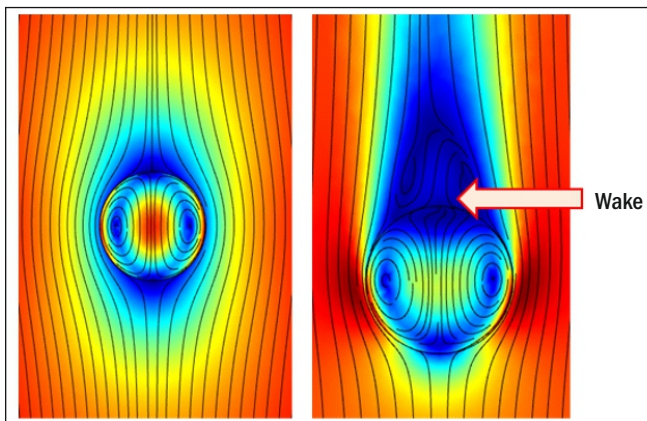


Fig.2: Streamlines inside and outside the drop at $Re_p = 0.289$ (left) and, $Re_p = 254$ (right).

CFD Modeling of Droplet Breakage and Coalescence

As discussed in the introduction section, breakage and coalescence is yet another important aspect which is fundamental to solvent extraction equipment. In a solvent extraction equipment, breakage of droplets can occur in different manners such as breakage due to turbulence and breakage due to shear. The breakage also significantly depends of the flow field. CFD modeling is being used to understand droplet breakage phenomena. To begin with, breakage of dispersed phase to form droplets under simpler settings has been studied. Some of the studies that have been done are studying droplet formation at top-submerged and bottom-submerged nozzles immersed in a quiescent continuous phase [22], drop formation on a single hole in a sieve plate and nozzle plate for quiescent continuous phase [23]. Drop formation under pulsatile flow of the dispersed phase at nozzles immersed in quiescent continuous phase has also been investigated [24]. Such CFD modeling typically involves interface-tracking simulations using methods such as Level Set or Volume of Fluid or Phase-field. The details of the computational models have been provided in our previous works [22,23]. Validation of CFD models has been done using in-house data [25,26] and data reported in literature [27]. Detailed insights are obtained from CFD simulations of drop breakage phenomena. For example, Fig. 3 shows the evolution of drop at a hole in a plate (a hole of a typical sieve plate) immersed in quiescent continuous phase for different velocities of the dispersed phase. The figure shows that the drop diameter and drop detachment height increase and drop detachment time reduces as the velocity of the dispersed phase through the sieve plate hole increases. Increase in drop detachment height with increase in dispersed phase velocity shows gradual transition toward jetting regime at higher velocities.

The studies have helped in understanding the effect of geometry (nozzle diameter, nozzle shape – flat versus sharp tip, diameter of plain hole and nozzle hole in a plate), physical properties (density difference, interfacial tension, contact angle) on diameter of drops produced as a result of breakage of the dispersed phase. Further studies on understanding phenomenon of drop breakage in different types of flow fields of the continuous phase such as counter-current flow, cross-current flow, rotational flow, and pulsatile flow, are going on. Extensive research is still needed to understand the droplet breakage in different types of turbulent flow fields typically observed in solvent extraction contactors.

While several studies have been done on drop breakage and formation, the computational studies on drop coalescence are scant. The coalescence, either interfacial or binary, involves drainage of the film between drop and its bulk phase or between two drops. Resolving of the film during drainage requires very fine mesh and very small time step size which makes CFD modeling of drop-level coalescence phenomenon computationally very challenging. Very few studies on CFD modeling of coalescence phenomenon have been reported [28]. Most of them are for coalescence of a drop with its bulk phase (interfacial coalescence). Studies on binary coalescence are rare. Extensive work is needed to understand various aspects of coalescence phenomenon such as binary coalescence, effect of interface-seeking impurities on coalescence, coalescence in pulsatile flow as is observed in the disengagement sections of pulsed columns etc.

CFD Modeling to Estimate Mass Transfer Coefficient

The CFD model described above for studying drag phenomenon can be extend to study mass transfer

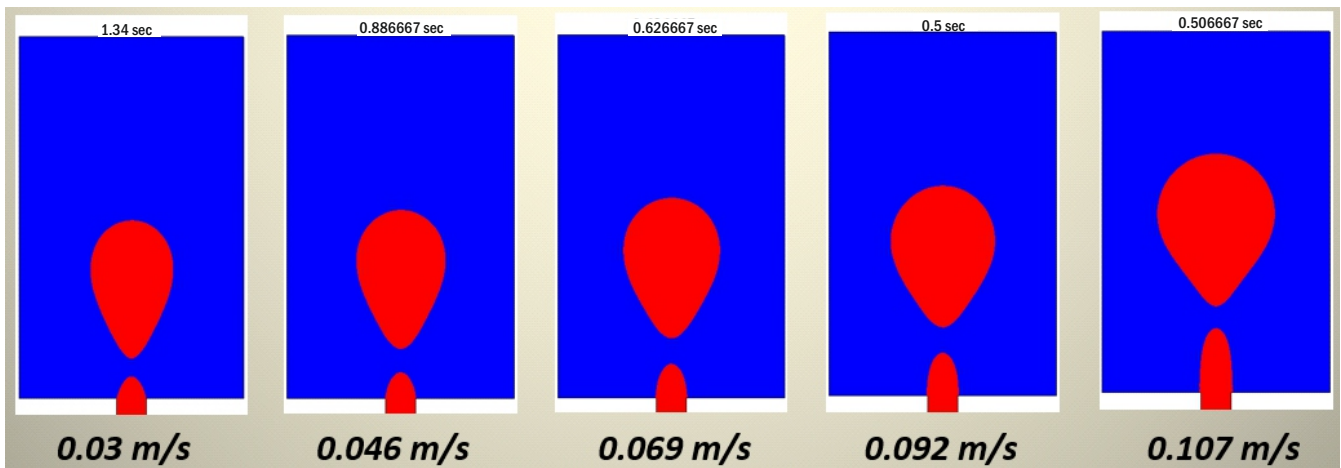


Fig.3: CFD modeling of drop formation at a hole in a plate immersed in a quiescent continuous phase for different velocities of the dispersed phase.

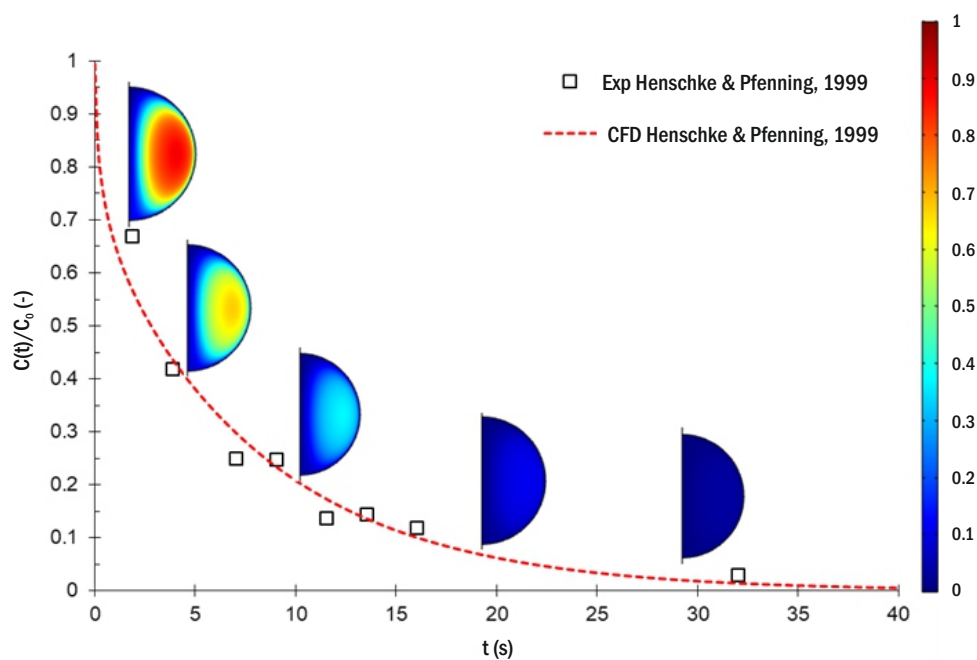


Fig.4: Comparison of CFD-predicted and reported variations of the normalized average concentration of the solute in a drop with time.

phenomenon also. For this, species transport equation needs to be solved additionally in the continuous phase and the drop phase after applying appropriate boundary conditions (concentration jump and continuity of mass transfer flux) at the liquid-liquid interface. The detailed description of the CFD modeling for estimation of mass transfer coefficient is provided in our previous study [16]. The model predicts the change in concentration of a solute inside the drop with time due to its mass transfer to the continuous phase flowing past the drop. The concentration-time profile can be further processed to estimate mass transfer coefficient and hence Sherwood number. The model has been validated by comparing the concentration-time profile obtained from the model with the same reported in the literature [29], as shown in Fig. 4 which also shows the dimensionless solute concentration profiles in one half of the drop at different instants of time. It may be noted that concentration of the solute in the drop gradually reduces with time. As there is a circulation inside the drop, mass transfer near the interface and center of the drop is convection controlled but at the center of the circulation inside the drop, mass transfer is mainly

diffusion controlled as the convective transport is minimum there. Hence, the slowest variation of concentration inside the droplet is observed in the vicinity of the center of the circulation inside the drop.

The model has been used to study the effect of shape of droplets on mass transfer. For this, comparison was done between spherical droplets, symmetrical ellipsoidal droplets and asymmetrical ellipsoidal droplets. Such simulations reveal some interesting results. For example, in some cases, ellipsoidal drops are found to have two internal circulation vortices in one half of the drop. Presence of secondary circulation vortex is found to enhance the mass transfer rate. The CFD model for estimating mass transfer was further used for studying mass transfer in pulsatile flow of the continuous phase. Pulsatile flow is important for air pulsed columns. The results of the simulations show that pulsatile flow of continuous phase leads to significant enhancement of mass transfer compared to the case of steady flow of the continuous phase. The results from CFD simulations were used to obtain a correlation to estimate Sherwood number (Sh) with particle

Reynolds number (Re_p), Schmidt number (Sc) as the independent variables for mass transfer from a spherical droplet. The correlation is given by Eq. (3). The values of the physical properties used to estimate particle Reynolds number and Schmidt number are the geometrical means of the physical properties of the two phases. The same correlation is found to be suitable for pulsatile flow of the continuous phase if pulsing velocity is also taken into account for calculating particle Reynolds number. The CFD-based correlation for estimating Sherwood number was implemented in axial dispersion model to simulate extraction of uranium in a pulsed disc and doughnut column. The predicted concentration profiles and end concentrations were found to be more accurate when CFD based correlation for Sherwood number was used compared to the case when an empirical model for estimating Sherwood number was used.

$$Sh = 2 + 0.00085Re_p^{1.13}Sc^{0.98} \quad (3)$$

CFD Modeling for Microfluidic Solvent Extraction

As mentioned earlier, there is lot of research going on in the field of microfluidic extraction, which is basically a process intensification tool. Several studies have been reported on microfluidic extraction of nuclear materials [30-34]. While majority of these studies have been experimental in nature, numerical simulations find applications in understanding various aspects relevant to solvent extraction in microchannel. In a typical microfluidic extraction system, a flowing aqueous phase is contacted with a flowing organic phase at a microfluidic junction. When the two phases come in contact at the microfluidic junction, depending on the geometry and material of construction of the junction, one of the phases may get dispersed in the continuum of the other. Depending on the flow rates, design of the microfluidic junction (T-junction, Y-junction etc.), physical properties of the two liquid phases (viscosity and interfacial tension) different types of flow patterns may emerge. Some typical flow patterns are slug flow, droplet flow, finely dispersed flow, slug and droplet flow, core-annular flow and parallel flow. Slug flow, droplet flow and finely dispersed flow are dispersed flow patterns in which dispersed phase breaks down in discrete entities. Parallel and core-annular flow are non-dispersive flow patterns in which two phases do not mix but flow along the microchannel with a continuous liquid-liquid interface. CFD modeling can be used to understand different aspects of microfluidic extraction. It can be used to find out the kind of flow pattern and size of the dispersed phase entities that will be generated at a microfluidic junction for a given liquid-liquid system, geometry of the microfluidic junction and flow rates of the liquids. It can also be used to estimate the velocity of the slugs/drops flowing in the microchannel and to estimate the interphase mass transfer coefficients. Prediction of the flow pattern, size of the dispersed phase (drop diameter/slug length) and mass transfer coefficients can help predict the mass transfer expected in a microfluidic extraction system.

To predict the flow pattern expected at a microfluidic junction, interphase capturing/tracking simulations are required. This typically involves solving the continuity and momentum equations while using an interface-capturing/tracking method such as Volume of Fluid (VOF)/level-set/phase-field/Arbitrary Lagrangian-Eulerian framework [35]. Further, to quantify interphase mass transfer inside the microchannel, simulations can be done for the fixed liquid-liquid interface if it is known priori. The dispersed entities (slug/drops) are periodic in nature. Thus, single unit cell approach can be used in which a periodic domain comprising a single

drop or slug and continuous phase surrounding it can be used after applying proper boundary conditions at the periodic boundaries, at the interface between the two-phases and the other boundaries defining the computational domain [36,37]. Simulations typically involve solving Navier-Stokes equations for the two phases (continuous phase, slug/drop phase) followed by solution of species transport equations in the two phases with one way coupling between hydrodynamics and mass transfer. Applications of appropriate boundary conditions at the liquid-liquid interface helps in capturing internal circulation inside the drop/slug. The velocity of the slug/drop can be found out by finding the mixture velocity for which the drag force exerted on the slug/drop becomes zero as in a microchannel the drops/slugs eventually move at a constant speed [36]. With slug/drop size, slug/drop velocity and interphase mass transfer coefficients known, it is possible to estimate the mass transfer expected from a given microfluidic extraction system [38].

Simulations to predict the liquid-liquid flow pattern expected at a microfluidic junction have been carried out and validated with reported data [35]. Simulations of slug flow and droplet flow in microchannels have also been carried out and validated with in-house and reported experimental data. Fig. 5(a) and Fig. 5(b) show typical flow field obtained from CFD simulations of droplet flow and slug flow, respectively, in a circular microchannel. Internal circulations inside the slug/drop can be observed clearly.

Simulations in case of non-dispersive microfluidic liquid-liquid flows such as core-annular flow (CAF) or parallel flow (PF) are easier, as tracking of liquid-liquid interface is not required in such flows. The position of the interface can be obtained analytically [39]. CFD modeling of such non-dispersive flows has been carried out to fundamentally understand the phenomenon of liquid-liquid mass transfer in such flows [39]. Fig. 5(c) shows typical velocity field obtained from CFD simulations of core-annular flow in microchannel. CFD model of flow and mass transfer in CAF was used to perform parametric analysis and the resultant data were used for obtaining correlations to estimate Sherwood numbers for the core (Sh_c) and annulus (Sh_a) for liquid-liquid mass transfer in CAF. The correlations are given by Eqs. (4) and (5) where z is

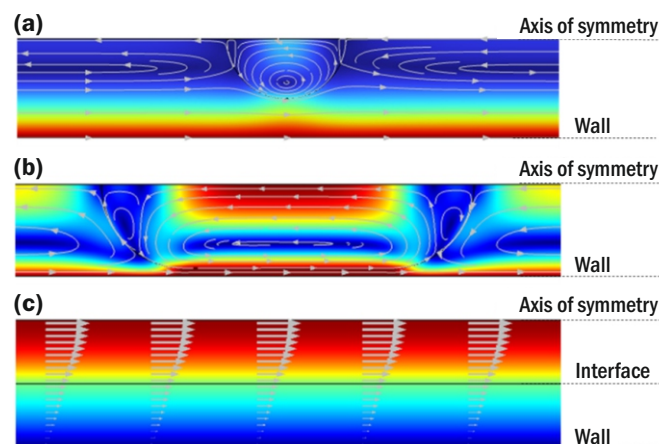


Fig.5: Typical velocity profiles and streamlines/ velocity vectors in (a) droplet flow and (b) slug flow (c) core-annular flow as obtained from CFD simulations carried out to study flow field and mass transfer in microchannels ((a) and (b): velocity field in droplet frame of reference using unit cell approach; c: velocity field in lab frame of reference; blue and red colors represent zero and maximum velocity magnitude respectively in rainbow color scale; geometries are axisymmetric).

axial position, D_{hc} and D_{ha} are hydraulic diameter for the core and annulus respectively, Re_c and Re_a are the Reynolds numbers for core and annulus respectively and Sc_c and Sc_a are the Schmidt numbers for the core and the annulus respectively.

$$Sh_c = 1.0901 Re_c^{0.5053} \left(\frac{z}{D_{hc}} \right)^{-0.5053} Sc_c^{0.5053} \quad (4)$$

$$Sh_a = 0.4401 Re_a^{0.4512} \left(\frac{z}{D_{ha}} \right)^{-0.4512} Sc_a^{0.4512} \quad (5)$$

Similar correlations are being obtained to estimate Sherwood number in droplet and slug flow regimes based on the regression of data resulting from parametric analysis done using validated CFD models for simulating hydrodynamics and mass transfer in droplet and slug flow regimes.

Conclusions

The present article provides an overview of how CFD can be used as an effective tool to simulate and understand the fundamental phenomena relevant to solvent extraction. Such CFD studies typically involve simulations at the level of a single droplet. The results from such simulations can be used to obtain the CFD-based laws/correlation/equations to replace the empirical correlations which are typically used as closure equations in equipment-level CFD simulations of solvent extraction equipment. Thus, apart from understanding fundamental phenomena relevant to solvent extraction, CFD modeling of fundamental phenomena relevant to solvent extraction eventually helps in reducing empiricism in equipment-level CFD models. CFD simulations of such phenomena are also very useful as conducting experimental studies at a single drop level is usually difficult.

CFD simulations have been carried out to understand the phenomenon of drag in liquid-liquid system in which the effect of internal circulation inside the droplet and turbulence in the continuous phase on drag coefficient has been captured. A CFD-based drag model has been obtained and implemented in equipment-level CFD model. Similarly, CFD studies have been performed to understand the phenomena of drop formation at nozzles and holes in plates submerged in quiescent continuous phase. However, further studies are required to understand the drop formation and droplet breakage in complex flow conditions of the continuous phase. Mass transfer from a single droplet has been studied in detail by developing a CFD model which captures the effect of internal circulation inside the droplet on mass transfer. A CFD-based correlation has been obtained to estimate Sherwood number for mass transfer from a spherical droplet under steady and pulsatile flow of the continuous phase. This CFD-based correlation has been implemented in equipment-level mass transfer models and is found to work well. Effect of shape of the droplet on mass transfer has also been studied using CFD. However, further studies are needed to understand mass transfer in presence of Marangoni convection and mass transfer from deformable droplets.

Extensive work has been carried out to understand liquid-liquid two-phase flow and mass transfer in microchannels which are being explored for intensification of solvent extraction processes. CFD simulations have been carried out to fundamentally understand liquid-liquid two-phase flow hydrodynamics and mass transfer in different flow regimes (slug flow, droplet flow, core-annular flow) in microchannels. Further understanding is required to quantify the extent of mass transfer during formation of slugs and droplets at microfluidic junctions through computationally

more challenging models. The quantitative data resulting from such CFD simulations can help design efficient microfluidic systems for different separation tasks.

References

- [1] H. Singh, and C.K. Gupta, Mineral Processing and Extractive Metallurgy Review, 2000, 21 (1-5), 307.
- [2] R. Natarajan, Progress in Nuclear Energy, 2017, 101, 118.
- [3] R. Yadav, and A.W. Patwardhan, Chemical Engineering Journal, 2008, 138(1-3), 389.
- [4] K.K. Singh, S. Sarkar, N. Sen, S. Mukhopadhyay, and K.T. Shenoy, BARC Newsletter, 2021, Nov.-Dec., 45.
- [5] N. Sen, K.K. Singh, A.W. Patwardhan, S. Mukhopadhyay, and K.T. Shenoy, Separation Science & Technology, 2016, 51(17), 2790.
- [6] S. Sarkar, K.K. Singh, S.M. Mahajani, and K.T. Shenoy, Solvent Extraction and Ion Exchange, 2020, 38(5), 536.
- [7] K.K. Singh, S.M. Mahajani, K.T. Shenoy, and S.K. Ghosh, Industrial Engineering Chemistry Research, 2009, 48(17): 8121-8133.
- [8] N. Sen, K.K. Singh, A.W. Patwardhan, S. Mukhopadhyay, and K.T. Shenoy, CFD modelling to predict mass transfer in pulsed sieve plate extraction columns. 12th International Conference on Computational Fluid Dynamics in the Oil & Gas, Metallurgical and Process Industries (CFD-2017), 30 May- 1 June (2017), Trondheim, Norway.
- [9] J.-Q. Liu, S.-W. Li, Y.-Y. Wang, Q. Zhang, and S. Jing, Solvent Extraction and Ion Exchange, 2017, 3, 187-198.
- [10] S. Sarkar, K.K. Singh, and K.T. Shenoy, BARC Newsletter, 2017, 360, 18.
- [11] K. Gonda, and T. Matsuda, Journal of Nuclear Science and Technology, 1986, 23(10), 883.
- [12] N. Sen, M. Darekar, P. Sirsat, K.K. Singh, S. Mukhopadhyay, S.R. Shirsath, and K.T. Shenoy, Separation and Purification Technology, 2019, 227, 1156641.
- [13] D. Tsaoulidis, V. Dore, P. Angeli, N.V. Plechkova, and K.R. Seddon, Chemical Engineering Journal, 2013, 227, 151.
- [14] M.N. Kashid, D.W. Agar, and S. Turek, Chemical Engineering Science, 62(18-20), 5102.
- [15] J. Yin, and S. Kuhn, Chemical Engineering and Processing: Process Intensifications, 2023, 190, 109414.
- [16] S. Sarkar, K.K. Singh, and K.T. Shenoy, Chemical Engineering Science, 2023, 267, 118240.
- [17] J.S. Hadamard, Seances Acad. Sci. Paris, 1911, 152, 1735.
- [18] W. Rybczynski, Bull. Acad. Sci. Cracovie A, 1911, 1, 40.
- [19] J.F. Harper, and D.W. Moore, Journal of Fluid Mechanics, 1968, 32(2), 367-391.
- [20] A.R. Khopkar, and V.V. Ranade, AIChE Journal, 2006, 52(5), 1654.
- [21] A.R. Khopkar, G.R. Kasat, A.B. Pandit, and V.V. Ranade, Industrial and Engineering Chemistry Research, 2006, 45(12), 4416.
- [22] A. Roy, N. Sen, K.K. Singh, K.T. Shenoy, and R.B. Grover, Solvent Extraction & Ion Exchange, 2019, 37(2), 191.
- [23] N. Sen, K.K. Singh, S. Mukhopadhyay, and K.T. Shenoy, Chemical Engineering Communications, 2019, 206(10), 1317.
- [24] S. Agarwal, N. Sen, G. Sugilal, and K.K. Singh, Comparison of drop formation at sieve plate hole under pulsatile and non-pulsatile flow: a CFD study, 15th Biennial DAE-BRNS Symposium on Nuclear and

Radiochemistry (NUCAR-2021), 22-26 February (2022), DAE Convention Centre, Anushaktinagar, Mumbai, India.

[25] A. Roy, M. Darekar, K.K. Singh, and K.T. Shenoy, Nuclear Engineering & Technology, 2019, 51(3), 761.

[26] A. Roy, M. Darekar, K.K. Singh, K.T. Shenoy, and R.B. Grover, Nuclear Science & Techniques, 2018, 29(6), 88.

[27] A. Soleymani, A. Laari, and I. Turunen, Chemical Engineering Research and Design, 2008, 86(7), 731.

[28] F. Gebauer, M. W. Hlawitschka, and H.-J. Bart, Chinese Journal of Chemical Engineering, 2016, 24(2), 249.

[29] M. Henschke, and A. Pfennig, AIChE Journal, 1999, 45(10), 2079.

[30] N. Sen, K.K. Singh, S. Mukhopadhyay, and K.T. Shenoy, Chemical Engineering Research and Design, 2022, 177, 83.

[31] C. Mariet, A. Vansteene, M. Losno, J. Pellé, J.P. Jasmin, A. Bruchet, and G. Hellé, Micro and Nano Engineering, 2019, 3, 7.

[32] A. Abbasi, A. Rahbar-Kelishami, and M.J. Ghasemi, Journal of Rare Earths, 2018, 36(11), 1198.

[33] M. Darekar, K.K. Singh, P. Sapkale, A.K. Goswami, S. Mukhopadhyay, and K.T. Shenoy, Chemical Engineering and Processing-Process Intensification, 2018, 132, 65.

[34] D. Tsaoulidis, and P. Angeli, Chemical Engineering Journal, 2015, 262, 785-793.

[35] K.K. Singh, K.T. Shenoy, H. Rao, and S.K. Ghosh, Numerical simulation of liquid-liquid two-phase flow at microfluidic junctions, 3rd European Conference on Microfluidics (μ Flu'12), 3-5 December (2012), Heidelberg, Germany.

[36] D. Mikaelian, B. Haut, and B. Scheid, Microfluidics and Nanofluidics, 2015, 19, 523.

[37] J. Rivero-Rodriguez, and B. Scheid, Journal of Fluid Mechanics, 2019, 869, 110.

[38] R.K. Chaurasiya, K.K. Singh, S. Chakraborty, S. Mukhopadhyay, and S. Sarkar. Conceptual design of process for solvent extraction of uranium using core-annular flow in microchannels, International Solvent Extraction Conference (ISEC-2022), 26-30 September (2022), Gothenburg, Sweden.

[39] R.K. Chaurasiya, and K.K. Singh, Chemical Engineering Science, 2022, 249, 117295.

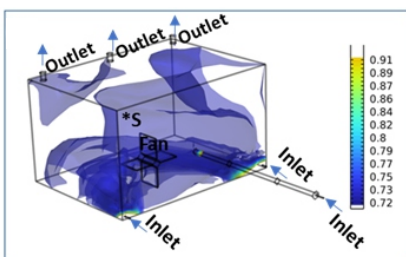
Carbon Nanotube Fiber

4

CFD-enabled Optimization for Highly Efficient Purging in Glovebox used for CNT Fiber Production

Rajath Alexander*, Amit Kaushal and Kinshuk Dasgupta

Glass & Advanced Materials Division, Bhabha Atomic Research Centre (BARC), Trombay – 400085, INDIA



Iso-surface plot of argon concentration

ABSTRACT

Glovebox is an important and necessary instrument required for the processing and handling of dangerous and highly reactive materials. Purging of glovebox with inert gas is necessary for the safe operation, but this is a highly inefficient process owing to the channeling and dead zone formation. In this work we have carried out computational fluid dynamics (CFD) simulation of a glove box used for carbon nanotube fiber (CNT fiber) production to understand the flow profile. The flow profile was used to optimize the inlet and the outlet locations in the glovebox. The CFD-enabled strategic placement of inlet and outlet in the glove box helps in lowering the gas requirement by 40%. The effect of rotating fan in the glove box was also investigated. The rotating fan helped in mixing the inert gas with existing air in the glovebox and eliminated the dead zone formation thereby enhancing the purging efficiency. The parameters from the CFD simulation were also successfully validated using experiments in actual glove box.

KEYWORDS: Computational Fluid Dynamics (CFD), Carbon nanotube fiber, Glovebox

Introduction

Glovebox is an ineluctable instrument in recent times in the field of engineering for the fabrication of advanced materials, which requires stringent environmental control for processing. Glovebox makes handling and processing of dangerous and reactive material possible. Radioactive material like plutonium is exclusively processed in the glovebox for fuel fabrication and processes involved in reprocessing of fuel [1]. One of the major commercial applications of the glovebox is its use in the fabrication of Li-ion batteries. Glovebox for making the battery is operated at a highly stringent condition where oxygen and moisture is maintained at less than 1 ppm [2]. Gloveboxes are maintained in an inert atmosphere by purging inert gas like argon and nitrogen when handling reactive material [2]. Glovebox is also maintained at a slight positive pressure to prevent the ingress of atmospheric gas. The positive pressure is necessary as rubber gloves tend to permeate gases [3]. The glovebox achieves a high level of purity by recirculating the inert gas through a regenerative system [4]. In the regenerative system, inert gas is passed through heated getter material like copper.

The glovebox used for the synthesis of CNT fiber is maintained at atmospheric pressure in comparison to other gloveboxes which are maintained generally at positive pressure. Some glovebox are also maintained in negative pressure when handling toxic and radioactive material as it prevents the leakage in the environment [5]. The glovebox that operating at positive pressure requires continuous purging of inert gas to maintain safe working conditions. The glovebox used for the synthesis of CNT fiber requires to be evacuated after every production run for the collection of CNT fiber and for

servicing the system. This working procedure makes the consumption of argon gas extremely high compared to conventional gloveboxes where the processed material can be recovered without evacuating the entire glovebox through an anti-chamber. This makes argon gas the most expensive consumable in the synthesis of CNT fiber.

In this work, we have utilized computational fluid dynamics (CFD) to lower argon consumption by improving purging efficiency by optimizing inlet and outlet locations. The feasibility of using a fan for enhancing purging efficiency was also assessed.

Experimental Section

The CFD analysis was carried out on a glove with dimensions of 1200 mm length, 900 mm width, and 700 mm height with an attached horizontal tube furnace. The tube size in the furnace is 1000 mm in length and 45 mm in diameter. The flow in the system was modeled using k-ε turbulence model along with Reynolds Average Navier Stokes equations. The governing equations of the model are given below in Eqs (1-7):

$$\rho(\mathbf{u} \cdot \nabla) \mathbf{u} = \nabla \cdot [-p\mathbf{I} + \mathbf{K}] + \mathbf{F} \quad (1)$$

$$\nabla \cdot (\rho \mathbf{u}) = 0 \quad (2)$$

$$\mathbf{K} = (\mu + \mu_T)(\nabla \mathbf{u} + (\nabla \mathbf{u})^T) - \frac{2}{3}(\mu + \mu_T)(\nabla \cdot \mathbf{u})\mathbf{I} - \frac{2}{3}\rho k \mathbf{I} \quad (3)$$

$$\rho(\mathbf{u} \cdot \nabla) k = \nabla \cdot \left[\left(\mu + \frac{\mu_T}{\sigma_k} \right) \nabla k \right] + P_k - \rho \epsilon \quad (4)$$

$$\rho(\mathbf{u} \cdot \nabla) \epsilon = \nabla \cdot \left[\left(\mu + \frac{\mu_T}{\sigma_\epsilon} \right) \nabla \epsilon \right] + C_{\epsilon 1} \frac{\epsilon}{k} P_k - C_{\epsilon 2} \rho \frac{\epsilon^2}{k} \quad (5)$$

$$\mu_T = \rho C_\mu \frac{k^2}{\epsilon} \quad (6)$$

$$P_k = \mu_T \left[\nabla \mathbf{u} : (\nabla \mathbf{u} + (\nabla \mathbf{u})^T) - \frac{2}{3}(\nabla \cdot \mathbf{u})^2 \right] - \frac{2}{3}\rho k \nabla \cdot \mathbf{u} \quad (7)$$

*Author for Correspondence: Rajath Alexander
E-mail: alexander@barc.gov.in

The change in the composition of gases in the glovebox was modeled using species transport equation. The governing equation is given below in Eq (8).

$$\rho \frac{\partial}{\partial x} (\omega_i) + \rho(\mathbf{u} \cdot \nabla) \omega_i = \nabla \cdot (\rho D_{T,i} \nabla \omega_i + \rho \omega_i D_{T,i} \frac{\nabla M}{M}) \quad (8)$$

$$Sc_T = \left(0.58852 + 0.228 \left(\frac{v_T}{v} \right) - 0.0441 \left(\frac{v_T}{v} \right) \left[1 - e^{-\frac{5.165}{(v_T/v)}} \right] \right)^{-1} \quad (9)$$

$$D_{T,i} = \frac{v_T}{Sc_c} e^{(-\Gamma)} + D_{T,w} e^{(-1/\Gamma)} \quad (10)$$

$$\Gamma = \frac{0.01(l^*)^4}{(1+5l^*)} \quad (11)$$

The glovebox was purged with 80 LPM of argon and the reactor tube was purged with 4 LPM of argon. The gas was sent using a mass flow controller. The oxygen level in the system was validated using a zirconium dioxide oxygen sensor.

Result and Discussion

Single inlet outlet design

The CFD simulation result of the glove box with one inlet and one outlet is shown in Fig.1(a). It can be seen that the velocity is higher near the inlet and reduces drastically in other regions, especially in the corners away from the inlet and

outlet. This can cause variations of oxygen purge time at various locations in the glove box. The streamline showing the path of the gas flow with the highest mass flow rate is given in Fig.1(b). It can be seen that the majority of gas form a single vortex without sweeping most of the volume before exiting through the outlet. This will cause the purging gas to not evacuate the gas in the majority of the region in the glove box effectively. The argon distribution in the glovebox after 20 mins of purging is given in Fig.1(c). It can be seen that the argon mole fraction in the glove box is highly non-uniform. The iso-surface plot (Fig.1(d)) shows the region with the highest purging gas content (argon mole fraction) in the initial stage of purging (20 min). It can be seen that a channel between the inlet and the outlet with argon content is present indicating high channeling. The reduction of oxygen content in the location of the oxygen sensor is given in Fig.1(e). The oxygen content from CFD and sensor reading are close to each other reaffirming the accuracy of the CFD model. It can be seen that it takes around 2 h to reach 2 vol% which is the safe working level of the glove box. The high channeling in the glovebox has been seen from the CFD simulation causing the volume of the purging gas utilized to be 35 times the volume of the glove box. This indicates the high inefficiency of the process.

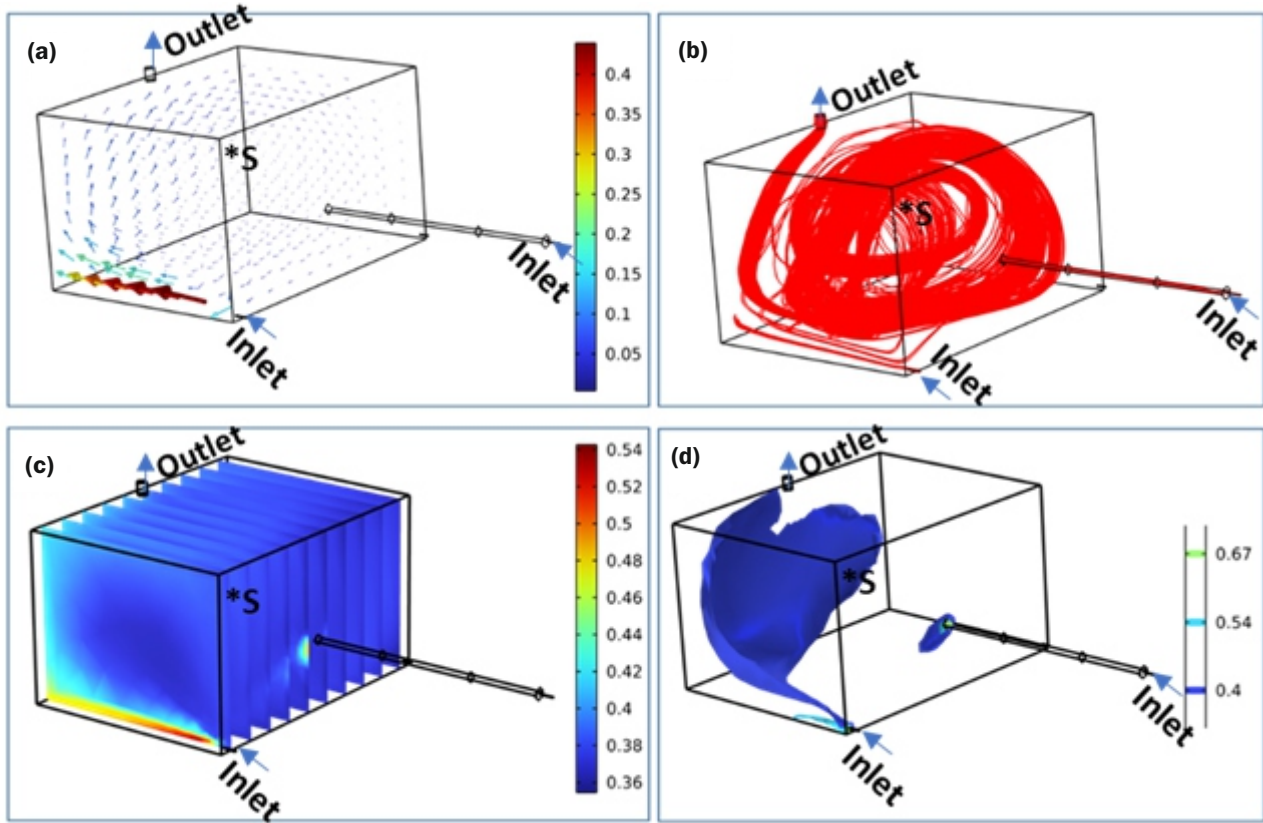
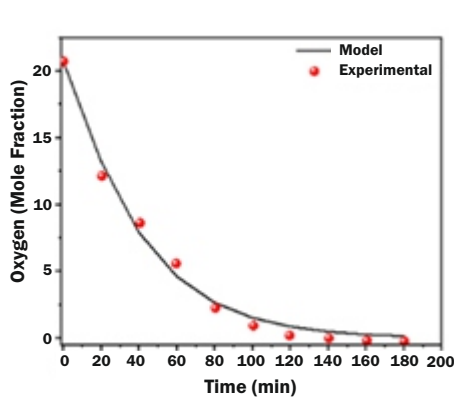


Fig.1: (a) Velocity profile in the system (S = Sensor Location). (b) Streamline of flux of argon in the system. (c) Argon concentration (mole fraction) in the glove. (d) Iso-surface plot of argon concentration. (e) Change in oxygen vol % with time.



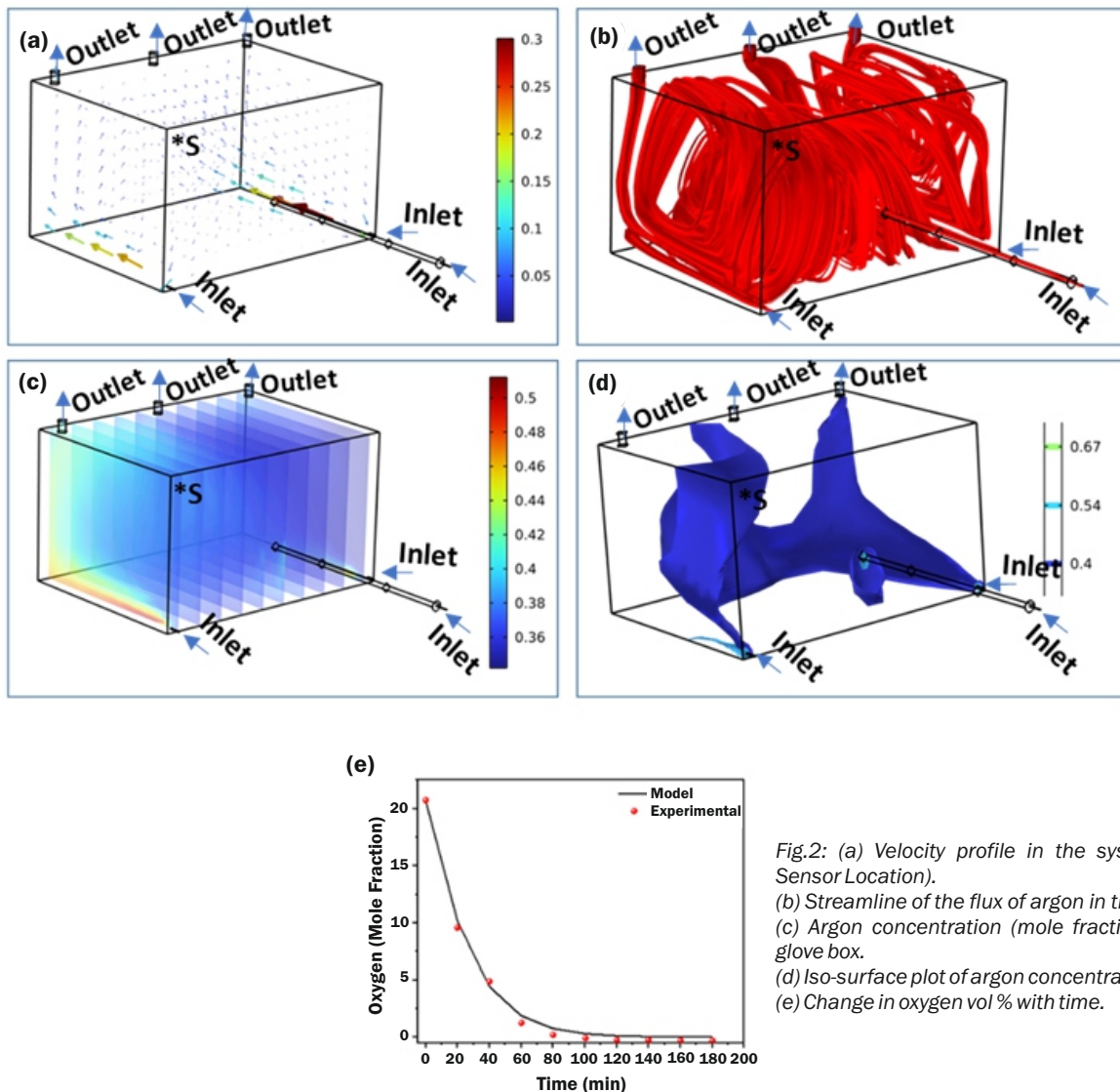


Fig.2: (a) Velocity profile in the system (S = Sensor Location).
 (b) Streamline of the flux of argon in the system,
 (c) Argon concentration (mole fraction) in the glove box.
 (d) Iso-surface plot of argon concentration.
 (e) Change in oxygen vol % with time.

Two inlet and three outlet design

To reduce channeling and dead zone as seen in the glovebox with one inlet and outlet, the glovebox box with two inlets and three outlets was utilized. The results of CFD simulation of the glovebox with two inlets and three outlets are shown in Fig.2(a). It can be seen from the velocity profile that even though maximum velocity is lower due to splitting the velocity from one inlet to two, the region which had negligible velocity in a single inlet case now has significantly higher velocity indicating better-distributed flow. The streamlines of purging gas are given in Fig.2(b). It can be seen that multiple vortices are formed when multiple inlets and outlets are utilized. The presence of more vortex will ensure superior mixing of purging gas with initially present air in the glovebox. The argon content in the glove box in the initial stage of purging (20 min) is shown in Fig.2(c). It can be seen that argon gas distribution is not homogenous. The iso-surface (Fig.2(d)) showing the highest argon content region indicates channeling between the inlets and the outlets. In multiple inlet outlet designs, despite channeling there exist multiple paths for the gas to exit which can cause enhanced purging. The oxygen percentage at the sensor location shown in Fig.2(e) indicates that required oxygen level of 2 vol% is attained in 120 min which requires 22 times volume of gas than volume of glovebox.

Rotating fan design

As seen from the results for multi-inlet outlet design, there is a significant improvement in purging efficiency. This

efficiency might further increase with an increase in the number of inlets and outlets. To achieve superior purging we have utilized a rotating fan inside the glovebox. The rotating fan was aimed to reduce the channeling and dead zone in the glovebox by enhancing the mixing in the glovebox. A four-blade impeller rotating at an rpm of 10 rpm was kept inside the glove box and experimental was performed. In CFD the rotating impeller was incorporated into the model using a moving mesh. The velocity profile (Fig.3(a)) indicates a substantial increase in velocity in the region other than the inlets. The streamlines (Fig.3(b)) of gas in the glovebox show the elimination of channeling and dead zone in the glovebox. The argon content in the glove box in the initial stage of purging is shown in Fig.3(c). It can be seen that argon gas is well distributed in the glovebox. The iso-surface of argon in the glovebox is also shown in Fig.3(d) also indicates homogenous argon concentration in the glovebox. The oxygen percentage at the sensor location shown in Fig.3(e) indicates that required oxygen level of 2 vol% is attained in 1 h which requires 17.5 times volume of gas than volume of glovebox.

Conclusions

Computation fluid dynamics was used for determining the flow profile and oxygen, argon distribution inside a glovebox with the objective of reducing the consumption of argon used as the purging gas. Channeling and large dead zone created high inefficiency in purging when only one inlet and outlet were used. The channeling and dead zone in the glove box were reduced by introducing the purging gas through two inlets and

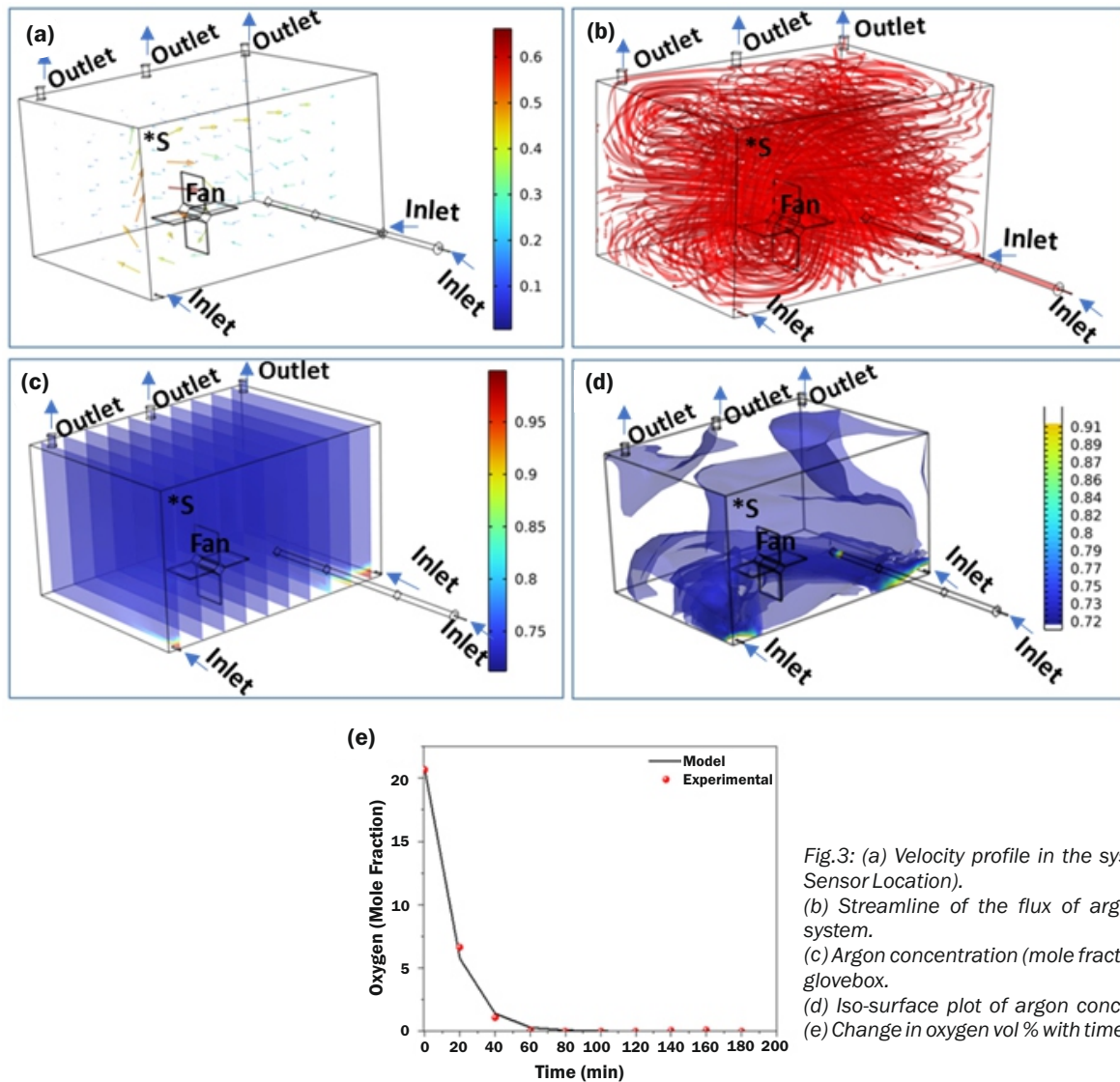


Fig.3: (a) Velocity profile in the system (S = Sensor Location).
 (b) Streamline of the flux of argon in the system.
 (c) Argon concentration (mole fraction) in the glovebox.
 (d) Iso-surface plot of argon concentration.
 (e) Change in oxygen vol % with time.

taking it out through 3 outlets. Multiple inlets and outlets also increased the number of vortices in the glovebox which enhanced the mixing and improved the purging efficiency. The introduction of a rotating fan in the glovebox further enhanced the efficiency of the purging by improving the mixing, it reduced the purging requirement by ~50 % from the initial configuration having one inlet and outlet.

References

[1] M. Rentetzi, “Determining Nuclear Fingerprints: Glove Boxes, Radiation Protection, and the International Atomic Energy Agency”, *Endeavour*, 41 (2017) 39-50.
 [2] K. Tokumitsu, H. Fujimoto, A. Mabuchi, T. Kasuh, “High capacity carbon anode for Li-ion battery: A theoretical explanation”, *Carbon*, 37 (1999) 1599-1605.
 [3] N. Vahdat, J.S. Johnson, A. Neidhardt, J. Cheng, D. Weitzman, “Permeation of Chemicals Through Glove Box Glove Materials”, *Applied Occupational and Environmental Hygiene*, 10 (1995) 943-950.
 [4] M.S. Hu, *The Design and Development of Control System for High Vacuum Deoxygenated and Water-Removal Glove Box with Cycling Cleaning and Regeneration*, Applied Modern Control, Intech Open, 2018.
 [5] T. Fujita, K. Ohtani, M. Hayashi, M. Kozeki, T. Ide, K. Sakuno, “Earthquake resistance test of full-scale glove box”, *Trans. 10th SMIRT*, k2 (1989) 877-882.

Notations	
ρ	Density (kg/m ³)
μ	Dynamic viscosity (kg/m.s)
\mathbf{u}	Velocity vector (m/s)
p	Pressure (Pa)
\mathbf{F}	Body force (N.m ⁻³)
μ_T	Turbulent dynamic viscosity (kg/m.s)
ν	Kinematic viscosity (m ² /s)
ν_T	Turbulent kinematic viscosity (m ² /s)
k	Turbulent kinetic energy (m ² .s ⁻²)
$C_\mu, C_{\epsilon_1}, C_{\epsilon_2}, \sigma_k, \sigma_\epsilon$	Model constant (0.09, 1.44, 1.92, 1.0, 1.3)
ϵ	Turbulent dissipation rate (m/s ³)
D_{τ_i}	Turbulent diffusion coefficient (m ² /s) of i th species (i; 1= Nitrogen, 2= Oxygen, and 3= Argon)
Sc_T	Turbulent Schmidt number
l^*	Characteristic length (m)
ω_i	Mass fraction of i th species (i; 1= Nitrogen, 2= Oxygen, and 3= Argon)
M	Molar mass (kg)

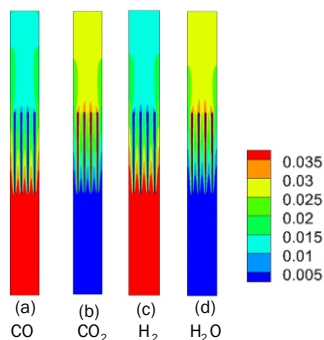
Hydrogen Recombiner

5

Hydrogen Recombiner CFD Model: Development, Benchmarking and Performance Evaluation

Bhuvaneshwar Gera*, Pavan K. Sharma, Vishnu Verma and Jayanta Chattopadhyay

Reactor Safety Division, Bhabha Atomic Research Centre (BARC), Trombay – 400085, INDIA



Mole fraction contours of various species
(CO= 4% (v/v) & H₂=4% (v/v) at inlet)

ABSTRACT

A significant quantity of hydrogen may be released into the containment of water cooled nuclear power reactors in case of postulated loss of coolant accident followed by non-availability of emergency core cooling system and moderator cooling in PHWR. This hydrogen gets distributed in the containment and may form combustible mixture with the available air. As a part of accident management program, hydrogen recombiners are being deployed worldwide in all water-cooled power reactors to manage the hydrogen concentration inside containment. The recombiners must be evaluated for their performance under various conditions such as their placement at various positions, their efficacy in presence of CO gas. Detailed experimental and modeling work of recombination process is required for their performance evaluation under different conditions. In this work, development of recombinder model and its integration to general purpose CFD code is reported. The developed model has been benchmarked against national and international experimental data. The benchmarked model has been further used to evaluate performance of recombinder under different conditions.

KEYWORDS: Hydrogen recombinder, Computational Fluid Dynamics (CFD)

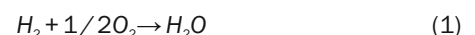
Introduction

Passive Autocatalytic Recombiners (PARs) are installed in water-cooled nuclear power reactor containments to manage the combustible gas released during a postulated severe accident condition. In a loss of coolant accident with unavailability of emergency core cooling system and moderator cooling system, the high temperature Zircaloy cladding oxidizes with available steam and hydrogen is formed. The generated hydrogen gets distributed in the containment and depending on the concentration of air, steam and hydrogen and available small ignition source, uncontrolled combustion can occur in the containment building, which represents a threat to the integrity of the last radiological barrier. Various techniques have been developed by industries depending upon the requirements to mitigate the hydrogen consequences such as pre-inerting, post-accident inerting, electrically operated recombinder, catalytic recombinder, igniters, mixing by use of fans and layout/geometry which promote mixing etc. Catalytic recombination of hydrogen with oxygen is the most popular method adopted by many countries (IAEA-TECDOC-1196) [1]. PARs are passive as they are self-starting and self-feeding having no moving parts and no external energy is required. Plate type PAR consists of a vertical channel where plates coated with catalyst are arranged in parallel. Platinum or palladium are used as catalyst as they are noble metals and have the ability to adsorb hydrogen and oxygen. The recombination reaction occurs spontaneously at the catalyst surfaces and the heat of reaction produces a natural convection flow through the enclosure. Water vapor as a product of reaction along with remaining hydrogen air mixture

moves upward because of buoyancy and fresh hydrogen air mixture enters through the bottom inlet section (Bachelierie et al., 2003) [2]. Most of the PARs are plate type; CFD modelling of plate type PAR, validation with national and international data and integration of CFD model with general purpose CFD code have been discussed in the subsequent sections. Recombiner performance has also been evaluated for (i) placing it near to wall or central region (ii) placing it at different elevations and (iii) presence of carbon monoxide (CO) in addition to H₂.

Mathematical Model of Plate Type Recombiner

For PAR modelling, the interaction of reaction kinetics, heat transfer and associated fluid flow in the catalytic recombinder and radiation heat loss from plates to surroundings are modeled. The simplified geometry of plate type PAR is shown in Fig.1. The governing mass, momentum, energy and conservation equations for hydrogen, oxygen, nitrogen and water vapor have been solved. Surface reaction takes places at catalytic plates. This reaction can be modeled by detailed reaction mechanism as mentioned by Deutschmann and another one proposed by Kasemo both reported by Appel et al., 2004 [3]. However, detailed reaction mechanism is computationally expensive, hence in present work the reaction has been modeled as a one-step reaction mechanism as proposed by Schefer, 1982 [4].



Where reaction rate (k) in kmol/m²/s is given as

$$k = 14 \exp(-14.9 \times 10^6 / R_u T) [H_2] \quad (2)$$

Where R_u is Universal gas constant, (8314 J/kmol K), T is Absolute temperature of the mixture, (K) and $[H_2]$ is Molar Concentration of Hydrogen, [mol/m³]. The above reaction

*Author for Correspondence: Bhuvaneshwar Gera
E-mail: bgera@barc.gov.in

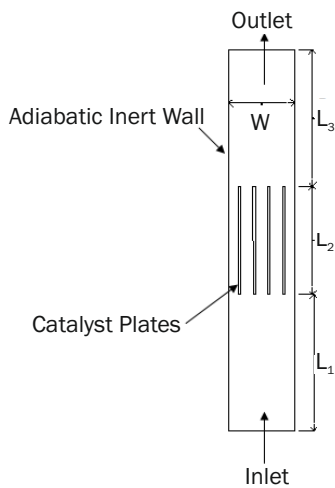


Fig.1: Simplified geometry of Plate Type PAR for 3D CFD computation.

provides additional source term for energy equation. The heat of reaction of the above reaction is 119.96 MJ/kg. The equation also provides source term in species transport equation for water vapour and sink term in species transport equations for hydrogen and oxygen. All these source or sink terms were applied at the very first fluid cell adjacent to solid plate. The high energy output from the reaction results in a considerable heat transmission from surfaces by convection and radiation to environment. Catalyst plates have been modelled as conducting walls to model the conjugate heat transfer in solid plates. The external wall has been modelled as no-slip adiabatic wall (Gera et al., 2011a [5]).

Benchmarking of Plate Type PAR Model

Plate type PAR model has been benchmarked with experimental data of REKO test facility (Reinecke et al., 2004) [6]. REKO test facility consists of a vertical flow channel with a rectangular cross-section 46 mm wide (W) and 146 mm deep. The channel is 504 mm long ($L_1+L_2+L_3$ (Fig.1)) with about 180 mm of channel length above the catalyst plates (L_3 (Fig.1)). For the reported experiments four plates made of stainless steel and coated with wash coat/platinum catalyst material were arranged in parallel inside the flow channel. The plates used were 1.5 mm thick and 143 mm long (L_2 (Fig.1)) and 146 mm deep.

Experiments have been performed for different inlet flow velocities (0.25, 0.50, and 0.80 m/s) at different inlet temperatures (298, 343 and 383 K). Inlet hydrogen concentrations were varied between 0.5 and 4% v/v. Fig.2 and 3 show the comparison of numerical results with experimental data for hydrogen mole fraction and catalyst plate temperature, respectively. Results are compared for two different inlet hydrogen concentration of 2% and 4% having inlet temperature of 343 K and velocity as 0.8 m/s. Results are found to be in good agreement with the experimental data. Fig.3 shows the temperature and hydrogen concentration contour plots for air hydrogen mixture of 2% v/v hydrogen concentration entering at 383 K for REKO test facility.

Mathematical Model for Integration of Recombiner with Containment model

A detailed analysis is required to optimize the passive autocatalytic recombiner locations and their numbers in nuclear containment. Recently, use of enhanced Computational Fluid Dynamics (CFD) model has shown significant improvements towards modelling such phenomena. But integration of detailed catalytic recombiner modelling with hydrogen distribution CFD code is complex. This is because the mesh size requirement to fully resolve the recombiner plates requires a very fine mesh size inside the recombiner channels (of the order of 0.1 mm) whereas for containment mesh size requirement is of the order of 100 mm. Thus, a simplified approach is required to model recombiner with containment CFD model. Numerous experiments have been performed on various types of recombiners to study the aspects like efficiency, start-up condition, hydrogen conversion rate, effect of operating pressure, temperature and other inlet conditions. Based on these experiments, empirical correlations have been developed to compute the hydrogen removal rate of particular make recombiners. These correlations describe the hydrogen consumption rate for a reference PAR type as a function of gas composition, temperature and pressure. The hydrogen consumption rates proposed by the different manufacturers are given by the empirical correlations (Bachelierie et al., 2003) [2]. For solution, as a simplified approach to integrate the recombiner model with containment CFD calculation, these correlations can be used to define localized volumetric sink of hydrogen, oxygen and source of energy and water vapour in the CFD codes. The transient Navier-Stokes equation with the energy

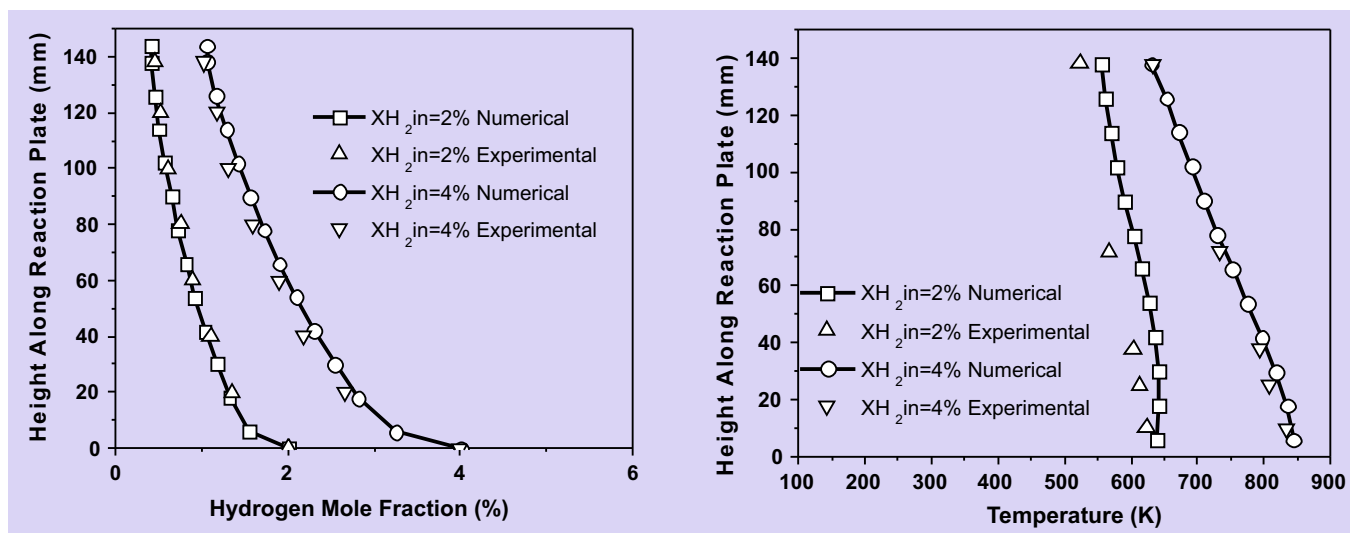


Fig.2: Steady state average hydrogen mole fraction in the recombiner section of REKO facility (left), catalyst surface temperature along the catalytic plate (right), (Inlet hydrogen mole fraction 2% & 4% and inlet temperature 343 K).

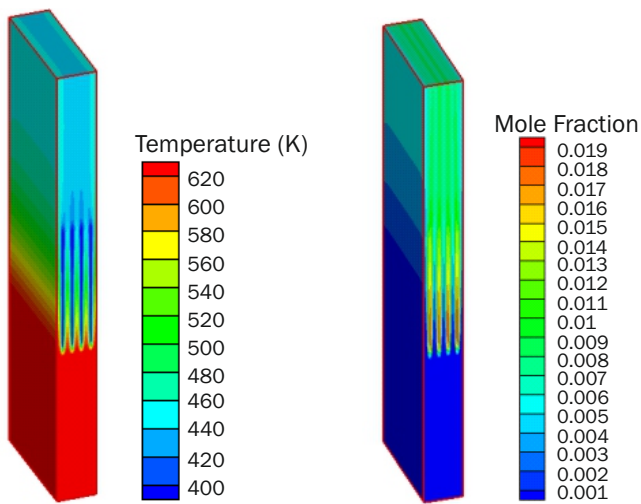


Fig.3: Temperature contours (left) and hydrogen mole fraction contour (right) for simulation performed for REKO facility (Inlet hydrogen mole fraction 2% v/v and inlet temperature 383 K).

and species transport was solved using commercial CFD software (CFD-ACE+, 2009) [7]. To model the mixture behaviour of hydrogen, air and steam, a continuum approach was used, in which only one velocity field was defined using the average density of gas mixture. The independent behaviour of hydrogen, oxygen and steam was considered using species transport equation. The recombiner section was modelled as fluid medium. The hydrogen conversion was modelled by means of the empirical correlation. It was assumed that the entire heat generated because of recombination is taken by solid plates and then transferred to fluid in the recombiner section by natural convection. First the hydrogen conversion rate was evaluated based on the reported manufacturer's correlation then it was used to obtain the solid plate temperature based on heat balance. Then the heat convected by fluid mixture through the recombiner section was computed and has been used as source term in energy equation at recombiner section. Based on the hydrogen conversion rate corresponding sink term for hydrogen and oxygen and source term for steam was incorporated through user coding. Recombiner boundaries have been modelled as adiabatic no-slip wall (Gera et al., 2011b [8]).

Benchmarking of Integrated Recombiner Model

The integrated recombiner model was benchmarked with PARIS-1 (PAR interaction studies) model geometry. As part of this study, two PARs of the AREVA design were considered in a 2D rectangular domain as shown in Fig.4. Height of PAR (h) was 1 m, and width (w) was 0.2 m. PAR entry and exit section widths were also equal to 0.2 m. There were two PARs located in the containment. The main purpose of the benchmark simulation was to observe the containment atmosphere mixing phenomena during a postulated severe-accident scenario. The results were compared with the CFD results obtained by Babić et al. (2006) [9].

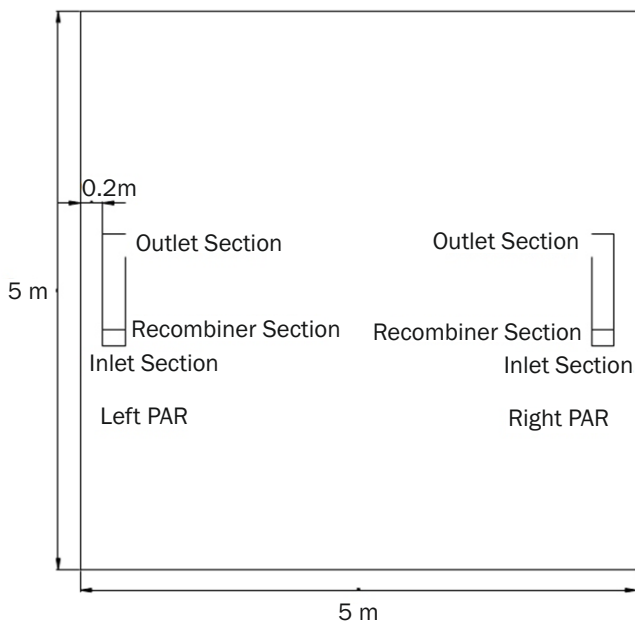


Fig.4: PARIS-1 model geometry with 2 PARs.

Fig.5 shows the amount of total hydrogen and the pressure variation in the representative containment. As the hydrogen is consumed energy gets generated because of recombination process. A low pressure region is created at the recombiner section and hydrogen moves from bottom of the recombiner section towards top outlet. Fig.6 shows the hydrogen mass fraction contour inside the representative containment at 20 and 300 seconds. Initially the hydrogen concentration is high, the reaction rate is fast hence consumption of hydrogen mass is rapid and there is fast pressure rise. The rate of hydrogen

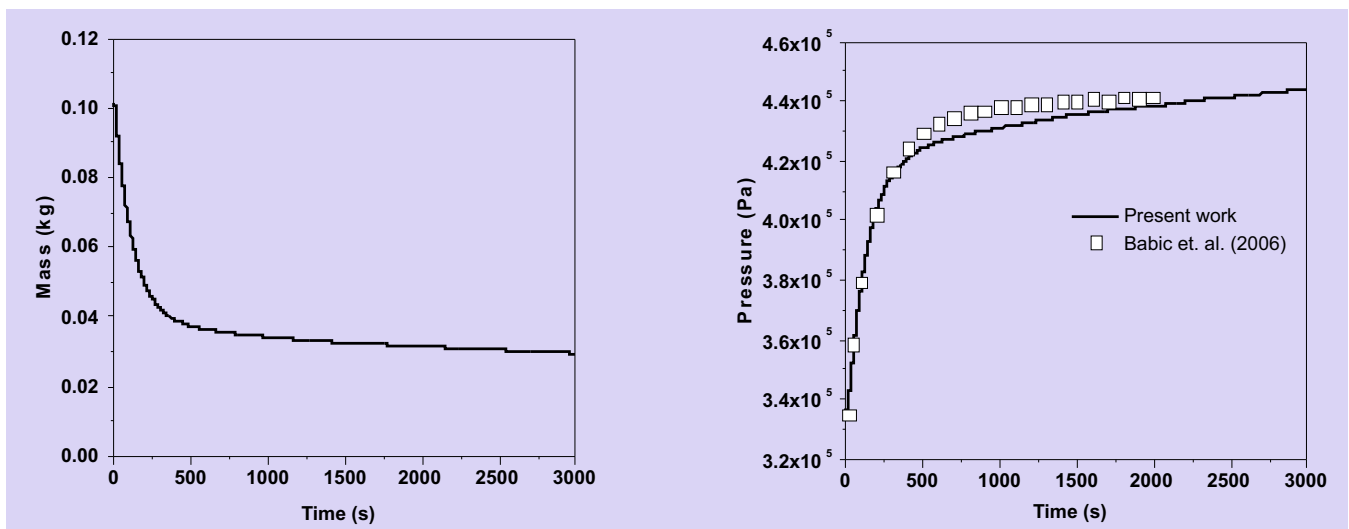


Fig.5: Average hydrogen mass (left) and average pressure (right) in the representative containment.

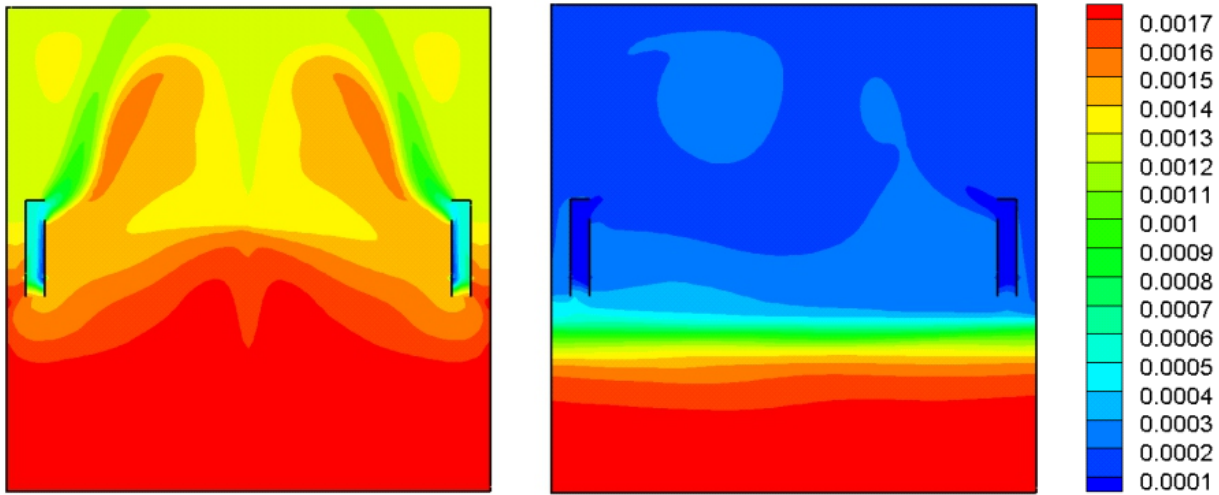


Fig.6: Hydrogen mass fraction at 20 s (left) and 300 s (right).

consumption and rate of pressure rise decreases as the hydrogen is consumed. After 300 seconds the upper region has low density due to high temperature. The cold unconsumed hydrogen remains in lower part and diffuses slowly towards PAR.

Benchmarking with National Data

The numerical approach was validated against experiment conducted at Hydrogen Recombiner Test Facility (HRTF) at Tarapur. HRTF is a cylindrical vessel of diameter 2.98 m with torospherical heads. Its total height is 9.12 m. The geometry and mesh of the vessel with PAR and injection pipe is shown in Fig.7. The PAR box has the dimensions 1.02 m (height) X 0.88 m (length) X 0.425 m (width) and is oriented above the injection pipe such that the length dimension is along the pipe direction. The recombiner box has been modelled as no-slip walls and is interacting with the vessel through top and bottom open section. As a part of validation, hydrogen injection experiment corresponding to 7.5% (v/v) of vessel volume was considered. The top and bottom sections of recombiner box are open and all sidewalls have been considered as no slip wall. No heat or mass transfer (steam condensation) occurs on the vessel walls. The simulation was

carried out and the results were predicted in terms of total hydrogen concentration variation at the inlet and the outlet with respect to time. These results were then compared with the results obtained from experiment performed at the test facility. As is seen from the Fig.8, there is good agreement in the rate at which hydrogen is getting consumed which is indicative of the rate of reaction between the experiment and CFD model. Due to proprietary nature of HRTF data, Y-axis numerical values are not shown. Thus, one can safely say that this particular CFD model can predict the reaction rate without much deviation from the experimental result.

Effect of Recombiner Placement

As part of the regulatory approval for the installation of PARs in the nuclear containment, it has been highlighted that the basis for number and location of the PARs is based on lumped parameter analysis, where effect of turbulence and buoyancy cannot be accurately modelled. It is required to have detailed assessment of the realistic flow fields around the PAR so that the adequacy of the location of the PARs can be confirmed. PARs are generally qualified in small to medium scale facilities worldwide. However, due to the fixed “recombiner size to vessel volume ratio” in these tests, the behaviour of the recombiner in large-sized containment volumes cannot be accurately predicted. It is required to understand the PAR behaviour in a large size room and to investigate the zone of influence of a PAR. Detailed CFD calculations in this regard will help to optimize the location of the PARs in different compartments of the containment. In the present section CFD simulations have been performed to evaluate the PAR performance in 210 m³ enclosure and PAR was positioned at centre or side location. CFD simulations have also been performed to evaluate the PAR performance in 2250 m³ enclosure and PAR was positioned at side location at top, bottom or central position. Different cases were studied by varying (i) computational volume (ii) hydrogen injection duration corresponding to total hydrogen concentration (iii) recombiner position (side wall and center region) (iv) effect of placing recombiner at different heights.

Case 1: Injection of hydrogen in 210 m³ enclosure having 60% (v/v) steam and rest air. Initial pressure and temperature 2.0E+05 Pa and 388 K. Recombiner is placed at the center of enclosure. Total mass of 2.1 kg of hydrogen was injected in 1800 s (this corresponds to 8% v/v uniform hydrogen concentration in the volume if hydrogen is properly mixed in the volume).

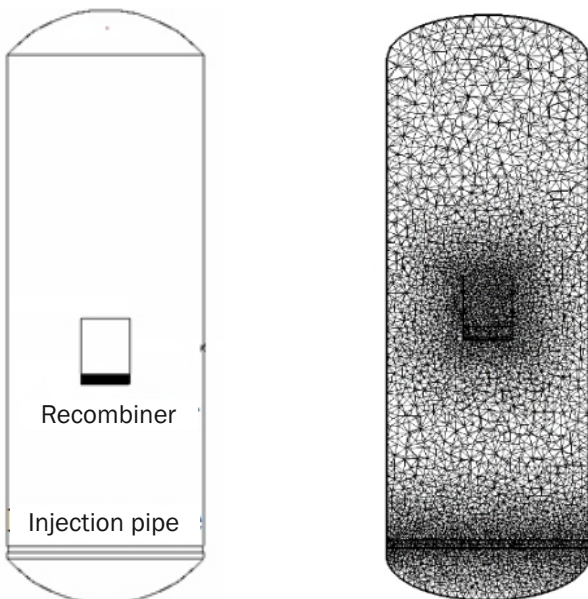


Fig.7: HRTF geometry (left) and mesh (right), PAR at center configuration.

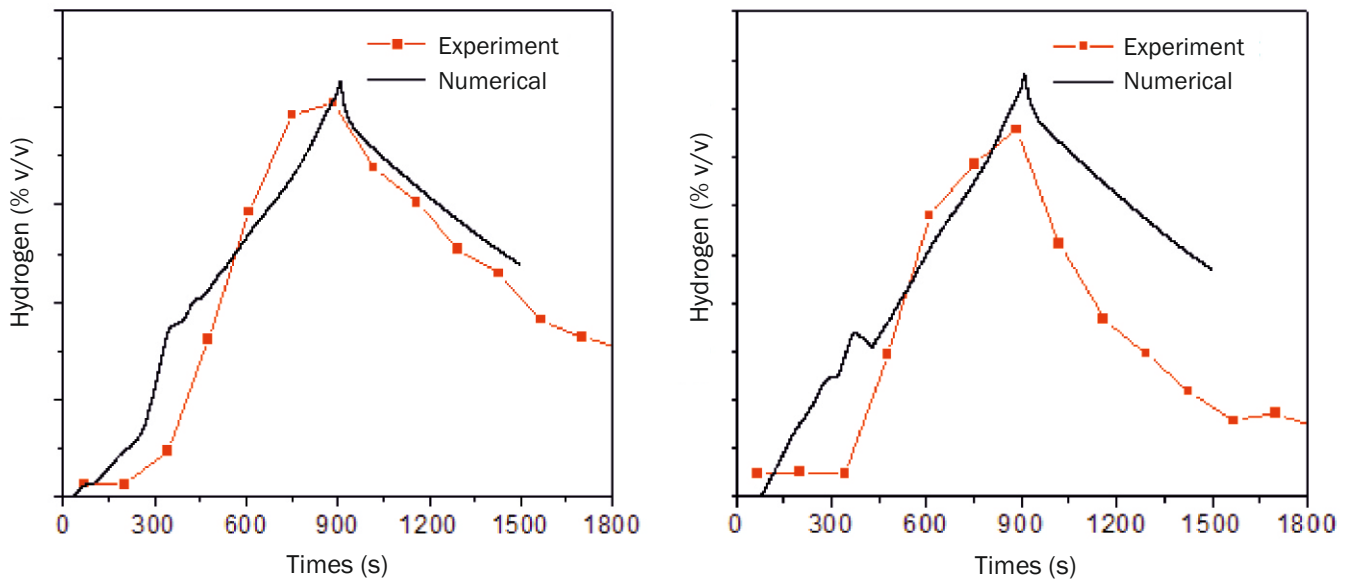


Fig.8: Temporal variation of the hydrogen concentration at PAR inlet (left) and outlet (right).

Case 2: Recombiner is placed at the side location in the enclosure. Other conditions are similar to Case 1.

Case 3: Injection of hydrogen in 2250 m³ enclosure having 60% (v/v) steam and rest air. Initial pressure is 2.0E+05 Pa and temperature is 388 K. Recombiner is placed at the side location at bottom position in enclosure. Total mass of hydrogen injected 22.3 kg in 1800 s, (this corresponds to 8% v/v uniform hydrogen concentration in the volume if hydrogen is properly mixed in the volume).

Case 4: Recombiner is placed at the side location at middle position in enclosure. Other conditions are similar to Case 3.

Case 5: Recombiner is placed at the side location at top position in enclosure. Other conditions are similar to Case 3.

Recombination of hydrogen and oxygen takes place at recombiner section and due to heat generation natural circulation loop is established in enclosure. The mass of hydrogen decreases with time as the recombination rate and plate temperature increase. The average temperature inside the vessel increases with time as the recombination progresses. Due to this natural circulation hydrogen in the top section of enclosure is depleted at much faster rate than the section below the recombiner. It can also be seen from the Figs.9-10 where contours of mole fraction of hydrogen are seen at different time intervals. The temperature of upper layers is higher. The pressure and temperature inside the vessel increase with time as the recombination process progresses. If

the PAR is placed at side location, its performance is slightly deteriorated as compared to centre location as shown in Fig.11. This can also be seen from Figs.9 and 10. However in actual reactor; most of the PARs are placed near wall. There is slightly delay in reaction to start in side wall placed recombiner (case-2) in comparison to centrally placed recombiner (case-1). All these results show that PAR is able to remove hydrogen in 210 m³ enclosure. After that its performance was evaluated for big enclosure size 2250 m³. The PAR performance is evaluated by placing recombiner at side at three different elevations (case 3 to 5). It was found out that PAR is able to mobilize the gases in such large volumes. In case 3 better mixing is observed, while in case 5 stratified layer is formed with higher concentration of hydrogen near injection level as depicted by Figs.12-13. In case of bottom configuration (Case 3) a better mixing is observed.

Effect of Presence of CO in Addition to H₂

Carbon monoxide (CO) may be generated inside the containment due to molten corium concrete interaction (MCCI) during a severe accident condition when vessel fails and corium comes in contact with raft concrete. The generated CO will interact with passive autocatalytic recombiners (PARs), which are installed inside nuclear reactor containments for H₂ removal. Depending on the conditions, CO may either react with oxygen to form carbon dioxide (CO₂) or act as catalyst poison, reducing the catalyst activity and hence the hydrogen conversion efficiency. CO is catalyst poison for platinum if

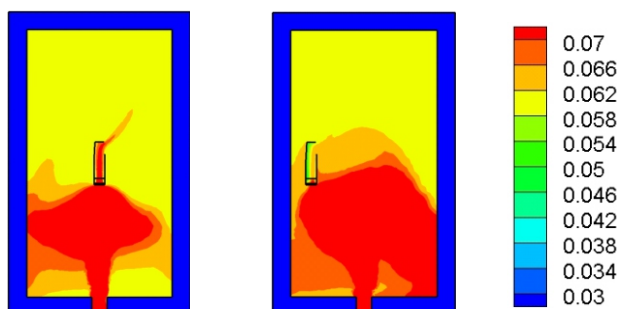


Fig.9: Hydrogen mole fraction contours at 1800 second for case 1 (left) and case 2 (right).

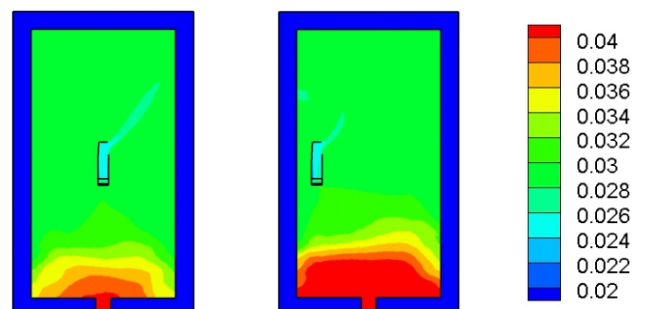


Fig.10: Hydrogen mole fraction contours at 6000 second for case 1 (left) and case 2 (right).

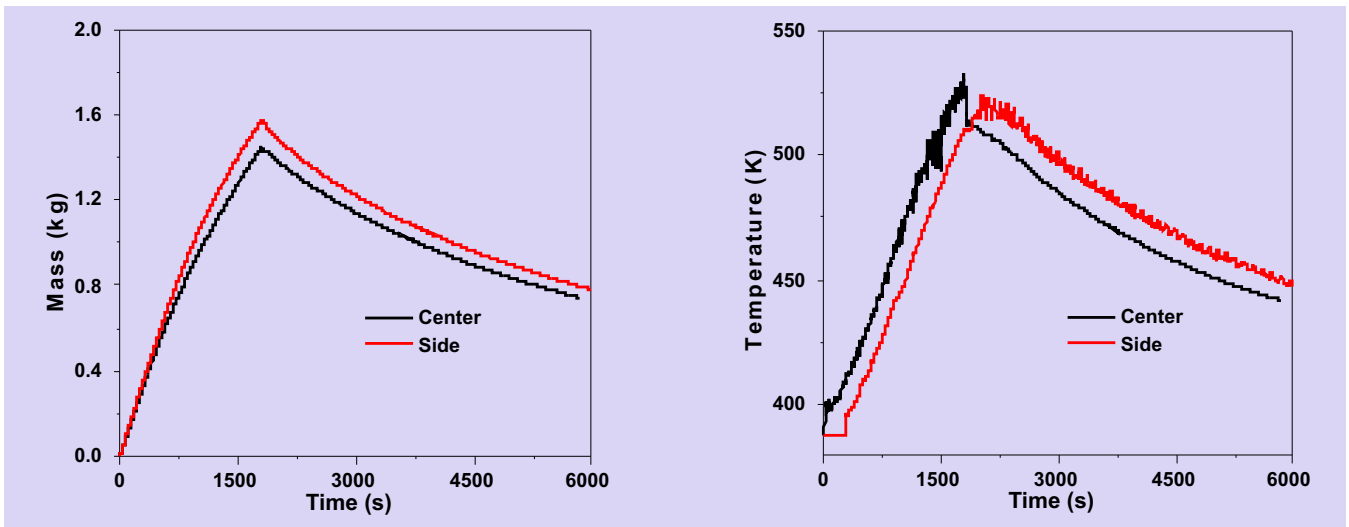


Fig.11: Temporal variation of total hydrogen mass (left) and PAR outlet temperature (right) in enclosure for case 1-2.

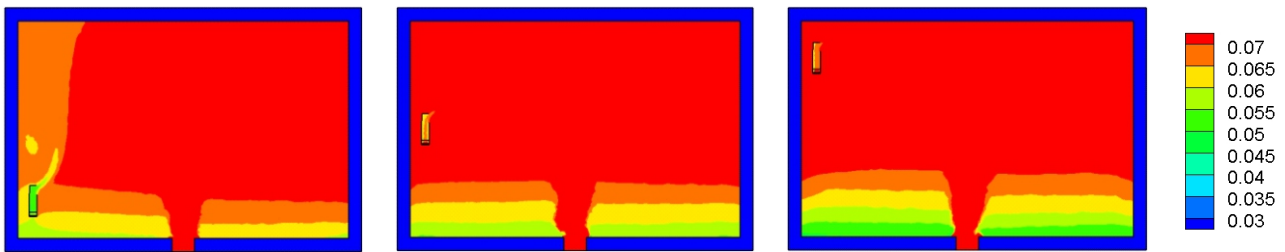


Fig.12: Hydrogen mole fraction contours at 1800 second for case 3-5.

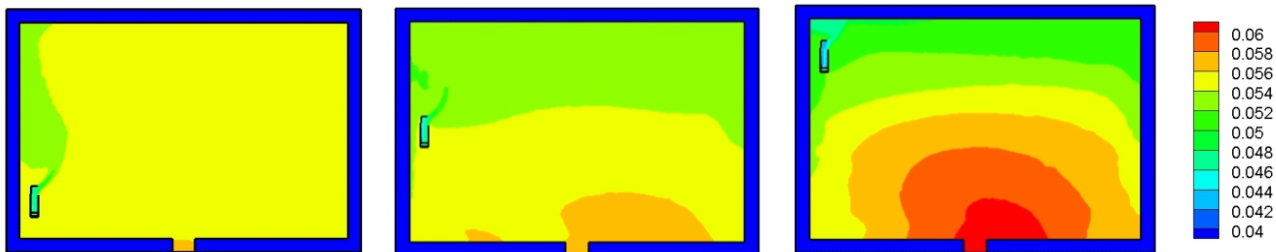


Fig.13: Hydrogen mole fraction contours at 18000 second for case 3-5.

injected before hydrogen, but if hydrogen is injected first, CO gets recombined due to high temperature and its role is to further increase the gas and plate temperature. Thus, CO has the potential to further increase the catalyst plate temperature, which may lead to the self-ignition temperature of combustible mixture. Hence, the effect of CO on catalyst plate temperature and on PAR removal rate needs to be investigated. For the present numerical study, a 2D CFD model has been developed using commercial software CFD-ACE+. Simulations were performed using this model to determine the effect of CO on catalyst plate temperature with 2 & 4 % (v/v) H₂ and 0-4 % (v/v) CO in air at the recombiner inlet for a reported experiment conducted at the REKO-3 test facility (Klauck et al., 2014) [10]. Fig.14 shows the result of the computation and comparison with experimental measurement. In these cases, H₂-air-CO mixture enters at a velocity of 0.5 m/s at 293 K with inlet H₂ concentration of 2 and 4% v/v and CO concentration 0-2% v/v. The results of present computation are in very good agreement

with available data. As the mixture enters in the recombiner section the reaction occurs at the leading edge of the catalyst plate. The reaction rate is highest at the leading edge of the plate. This is manifested by maximum catalyst surface temperature near the leading edge of the plate. As flow takes place over catalytic plate, boundary layer is formed over the plate surface and H₂/CO diffuses from bulk of the mixture towards plates for recombination. With the flow along the catalyst plate, concentration gradient decreases thus reaction rate also decreases along the catalyst plate.

Both the recombination reactions are exothermic and increase the plate temperature. The addition of CO leads to further increase in plate temperature. The maximum temperature of plate is 600 K when H₂ only for 2% v/v at inlet and 720 K for 2% v/v H₂ and 2% v/v CO at inlet. The depletion of H₂ and CO and formation of H₂O and CO₂ are shown in Fig.15 for one of the case. The species boundary layer formation is clear from this Fig.15 (Gera et al., 2023 [11]).

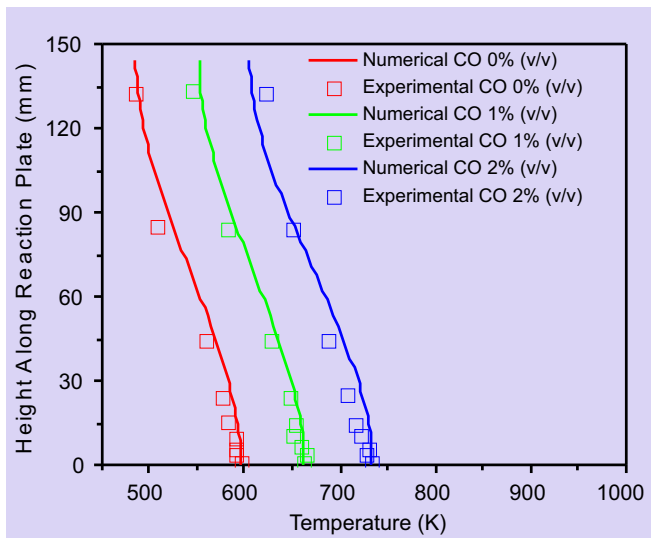


Fig.14: Comparison of computed plate temperatures with experiments for different CO concentration at inlet (H_2 2% (v/v) at inlet).

Conclusions

A CFD model for plate type hydrogen recombiner has been developed and validated against REKO experimental data. The simplified model of PAR has been integrated with general purpose CFD code used for simulating hydrogen distribution and the integrated model is verified with PARIS benchmark. The integrated code has also been validated against national data. The developed model has been utilized to evaluate the recombiner performance for different conditions such as (i) placing it near to wall or central region (ii) effect of placing recombiner at different elevations and (iii) presence of CO in addition to H_2 . It was found that performance of PAR at central region is better than placement of PAR at near wall region. In case of placing PAR at bottom elevation better mixing is observed. It was also found that recombiner maximum plate temperature is further increased by adding CO.

References

- [1] Mitigation of Hydrogen Hazards in Water Cooled Power Reactors, IAEA, Vienna, IAEA-TECDOC-1196, 2001.
- [2] Bachellerie E., Arnould F., Auglaire M., Boeck B. D., Braillard O., Eckardt B., Ferroni F., Moffet R. "Generic approach for designing and implementing a passive autocatalytic recombiner PAR system in nuclear power plant containments". Nuclear Engineering and Design, 221 (2003) 151-165.
- [3] Appel C., Mantzaras J., Schaeren R., Bombach R., Inauen A. "Catalytic Combustion of Hydrogen-Air Mixtures over Platinum: Validation of Hetero/Homogeneous Chemical Reaction Schemes". Clean Air, 5 (2004) 21-44.
- [4] Schefer R. W. "Catalyzed Combustion of H_2 /Air Mixtures in a Flat Plate Boundary Layer: II. Numerical Model". Combustion and Flame, 45 (1982) 171-190.
- [5] Gera B., Sharma P. K., Singh R. K., Vaze K. K. "CFD Analysis of Passive Autocatalytic Recombiner". Science and Technology of Nuclear Installations, Article ID 862812, Vol 2011 (2011a).
- [6] Reinecke E. A., Tragsdorf I. M., Gierling K. "Studies on Innovative Hydrogen Recombiners as Safety Devices in the Containments of Light Water Reactors". Nuclear Engineering and Design, 230 (2004) 49-59.
- [7] CFD-ACE+ V2009.2, User Manual, ESI CFD Inc., Huntsville, AL 35806.
- [8] Gera B., Sharma P. K., Singh R. K., Vaze K. K. "CFD Analysis of Passive Autocatalytic Recombiner Interaction with Atmosphere". Kerntechnik, 76 (2011b) 98-103.
- [9] Babić M., Kljenak I., Mavko B. "Numerical Study of Interaction between NPP Containment Atmosphere and Passive Autocatalytic Recombiners", Proceedings International Conference Nuclear Energy for New Europe 2006, Slovenia, September 18-21, 2006.
- [10] Klauck M., Reinecke E.A., Kelm S., Meynet N., Bentaib A., Allelein H. J. "Passive autocatalytic recombiners operation in the presence of hydrogen and carbon monoxide: Experimental study and model development". Nuclear Engineering and Design, 266 (2014) 137-147.
- [11] Gera B., Verma V., Chattopadhyay J. "Development and Validation of Diffusion based CFD model for Modelling of hydrogen and Carbon monoxide Recombination in Passive Autocatalytic Recombiner". Nuclear Engineering and Technology, 55 (2023) 3194-3201.

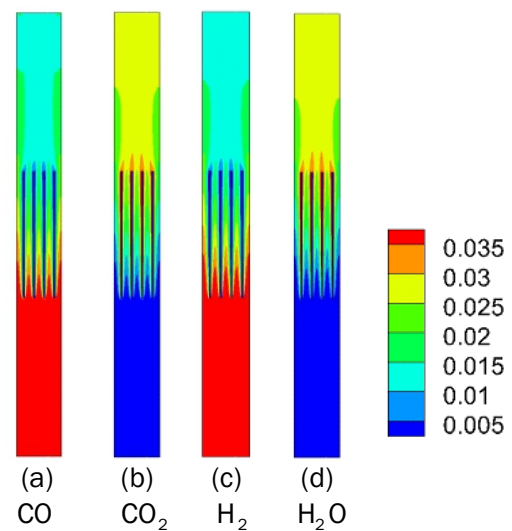


Fig.15: Mole fraction contours of various species ($CO= 4\%$ (v/v) & $H_2=4\%$ (v/v) at inlet).

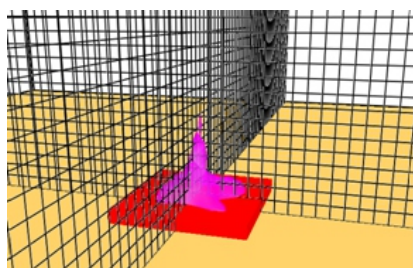
Fire Hazard Analysis

6

CFD based Fire, Explosion and Toxicity Safety Evaluation for Nisargruna Biogas Plant

Pavan K. Sharma*, Vishnu Verma and J. Chattopadhyay

Reactor Safety Division, Bhabha Atomic Research Centre (BARC), Trombay – 400085, INDIA



Biogas (Leak from top) volumetric concentration iso-surface between (LEL - UEL)

ABSTRACT

Fire Hazard Analysis (FHA) of a Nisargruna Biogas plant proposed to be installed at BARC hospital has been carried out to ascertain the adequacy of principles of fire safety and fire protection measures. In absence of any specific regulatory guidance on Biogas plant FHA, the generic safety objective-based FHA has been used. Defence-in-depth based dual failure philosophy has been used to evolve a suitable fire hazard methodology with objective of (i) nearly no loss of life (ii) no catastrophic effect to structure (iii) adequate fire rating (iv) no threat to public building (v) no oxygen deficiency or H₂S toxicity life loss for operator and (vi) acceptable separation distance and safety zone. A range of Design Basis Accidents (DBAs) using Computational Fluid Dynamic (CFD) analysis have been considered and these are found to have no significant life-threatening effect on the occupants in safe zone. The explosion from a hypothetical Beyond Design Basis Accident (BDBA) helps in deciding an acceptable separation distance from occupied public building and a suitable impact barrier for road or hospital canteen window.

KEYWORDS: Nisargruna biogas plant, Fire Hazard Analysis (FHA), Computational Fluid Dynamic (CFD)

Introduction

The Nisargruna technology has been developed at Bhabha Atomic Research Centre (BARC), Mumbai for decentralized processing of the biodegradable waste. The project has tremendous potential to support the ever-depleting energy sector by generating fuel and manure required for soil applications. The technology has evolved in last several years and about 250 such plants are operative in various parts of the country. Biogas related specific fire safety regulations are not available in prescribed codes in India [1]. Old National Building Code (NBC) permits a quantity of 2000 liters of flammable liquid but the new NBC code [2] and Atomic Energy Regulatory Board (AERB) code suggest that a large combustible material presence should be situated at outdoor or in a separate utility building [3]. The Indian Factory Act allows using unlimited quantity of oil/combustible gas for process use, subjected to certain conditions. The basis of use for such quantity is the fulfillment of mandatory nuclear safety objectives demonstrated by FHA. The AERB guideline provides the intent of the safety objectives. The number of biogas plants and accidents are growing [4-7]. Fortunately, only few of them had consequences on humans. Several reasons [8], such as leakages in storage tanks and pipes, accidental effluent discharges, sewage system overflow due to control failures or exceptional downpours, dangerous substance in the biogas raw materials, inadequate risk analysis [9], less attention to safety [10-16] and no learning from past accidents [6,7] are responsible for such accidents. In biogas plant two pertinent fire safety issues creep up. The first one is due to the methane and associated explosion. The second issue is the

conventional fire and its severity due to its quantity. The FHA addresses both these issues.

Overview of FHA Procedure

Nisargruna biogas plant is coming up in a mixed-use area near BARC Hospital, Anushaktinagar. Plant has large exits, internal free space and road which allow fast fire-fighting tender movement. The large open area and sufficiently large exit will help in easier escape for worker, natural ventilation of hot gases in event of fire and minimal chance of high temperature gas built-up and subsequent secondary fire generation. The adequate dimensions also ensure Acceptable Separation Distances (ASD) against biogas explosion. The biogas plant is proposed to be used in a low-pressure continuous utilization fashion without biogas storage and compression. The facility will have strict administrative control for the presence of human and the operation staff.

Being a first of a kind FHA, detailed study of different regulations has been done based on the following points.

(i) International consensus and Design Basis Fire Accident (DBFA) to find its impact on neighbouring structures and people.

(ii) Use of nuclear industry standard FHA approach.

(iii) Technical basis of biogas storage tank leakage.

(iv) CFD calculation of fire rating and Acceptable Separation Distances (ASD).

(v) No credit of first-hand firefighting but credit of fire tender capabilities.

(vi) CFD analysis of fire, explosion and toxicity for biogas release event.

*Author for Correspondence: Pavan K. Sharma
E-mail: pksharma@barc.gov.in

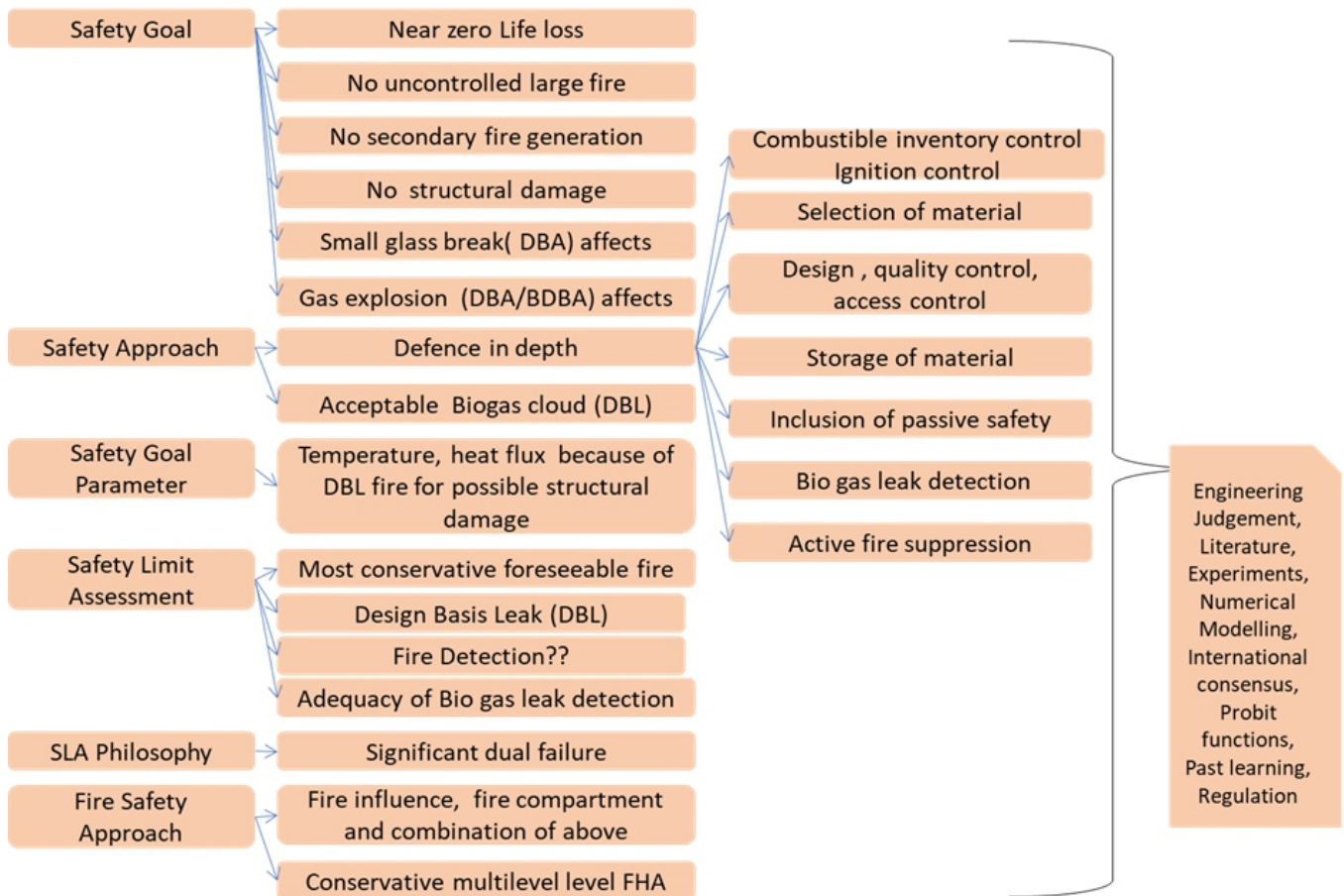


Fig.1: Fire Hazard Analysis philosophy for Nisargruna biogas Plant.

The Fire Hazard Analysis philosophy for Nisargruna biogas plant is shown in Fig.1. The FHA is a mandatory requirement to ascertain the adequacy of principles of fire safety and fire protection measures provided in any plant for safe operational/emergency states of a plant using defense-in-depth approach [17]. In absence of quantitative regulatory procedures/guideline for ASD for biogas plant, a fire hazard analysis procedure has been developed based on (i) dual failure safety analysis and (ii) acceptable individual risk probability values.

These aspects have been used to identify the hazard sources and events (e.g. release of gas) by considering the likelihood of the events and hence, calculate the effects of fire on neighboring objects. Another objective is to determine the

acceptable fire safety distance. The individual harm exposure threshold ($F_t \leq 3.5 \times 10^{-5}$ event per year) has been used for determining ASD and design fire [18,19]. However, the analysis also supports for event with lesser frequency such as gas release with storage tank breakage due to lightning on a highly conservative basis to calculate and quantify the fire risk for non-DAE public properties. Table 1 shows typical failure frequencies of biogas plant components. Category events 10^{-4} to 10^{-6} adopted from AERB SG D-5 which come under the category of multiple failures and rare events are considered as DBAs [20]. The breaking of biogas boundary and subsequent release of biogas into storage building has been considered for DBA. This DBA event may lead to gas fire /explosion as per biogas triangle shown in Fig.2.

Table 1: Typical failure frequencies of biogas plant components.

Event	Probability/frequency
High pressure gas line rupture	$5 \times 10^{-4}/\text{km-yr}$
Lightning strike	$1 \times 10^{-7}/\text{yr}$
Severe earthquake capable of rupturing pipe work	$1 \times 10^{-6}/\text{yr} - 1 \times 10^{-7}/\text{yr}$
Seal fire	Approximately $2 \times 10^{-4}/\text{holder-yr}$
Failure of a return valve on demand	$3 \times 10^{-2}/\text{yr}$
Failure of an excess flow control valve on demand	$1.3 \times 10^{-2}/\text{yr}$
Failure of an automatic shut off valve to close	$1 \times 10^{-2}/\text{demand}$
Failure of a level sensor	50 per 10^6 hrs
Split crown (without ignition)	Approximately $3 \times 10^{-4}/\text{holder-yr}$
Split crown explosions	$3 \times 10^{-5}/\text{holder-yr}$

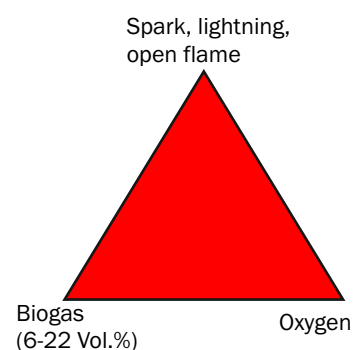


Fig.2: Biogas fire and explosion triangle.

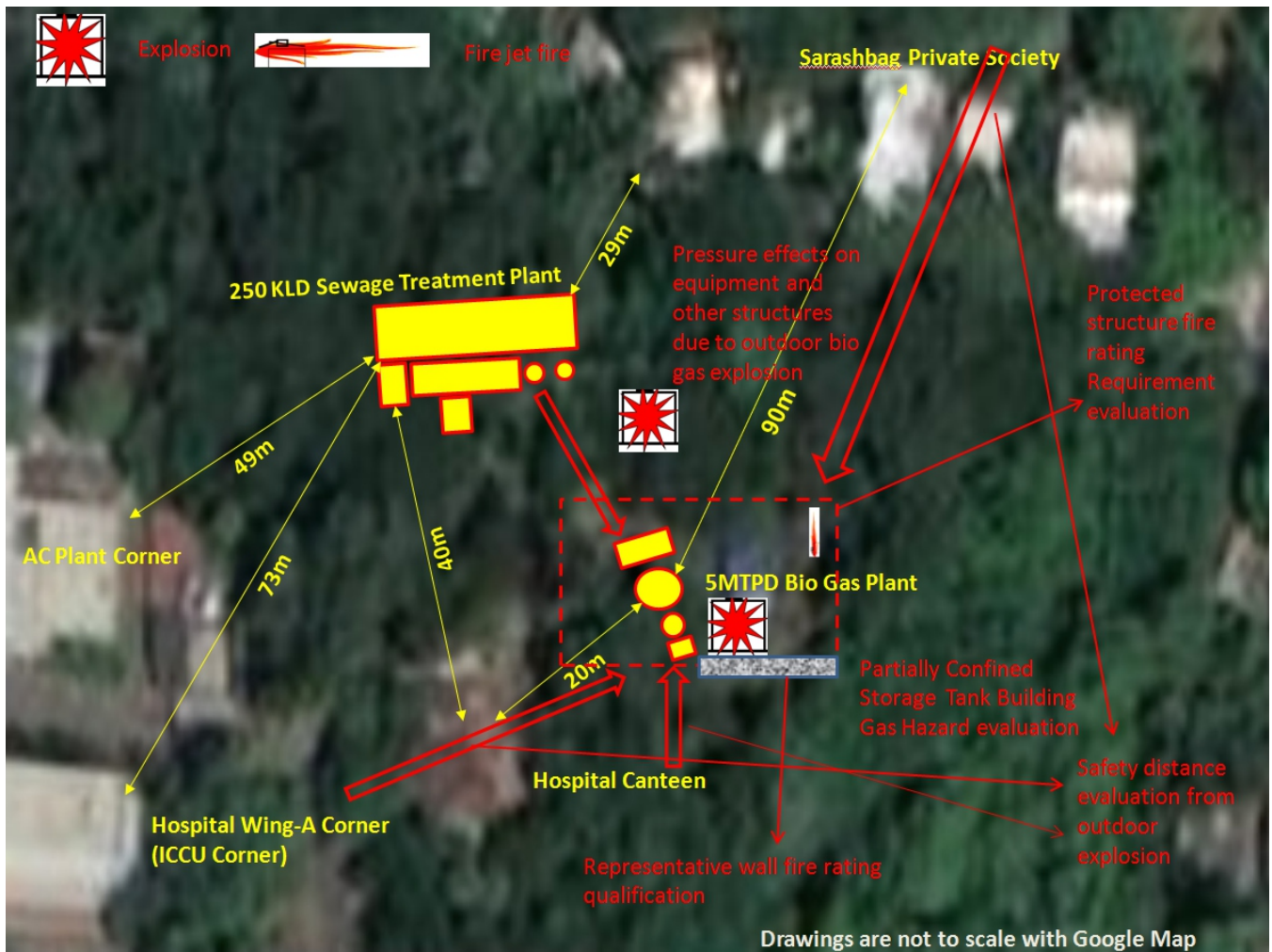


Fig.3: Schematic and fire and explosion concerns for Nisargruna biogas plant.

The Fig.3 depicts the simplified schematic and fire and explosion concern matrix (shown in sign of fire) for the present FHA. The red color star depicts the likely location of the gas explosion event. Each of the objectives i.e. external and internal gas explosion FHA, safety distance calculations and toxicity evaluations are described in the paper.

Biogas Leakage Hazard Evaluation Philosophy

The contemporary review of literature on biogas specific regulation brings some useful pointer for FHA procedure development. In Europe, safety measures against explosion risk are stipulated in Directives 99/92/EC [21]. A crucial topic as per regulations is the classification of plant areas [22]. The hazard classification in terms of various zones can be carried out based on geometrical characterization (extent and volume) of hazardous areas [23] and persistence time and cloud departure time. Hazardous Area Classification (HAC) [24] makes use of the concept of a nominal flammable gas cloud volume (V_z) in prevailing level of ventilation. HAC can be classified in various zones such as

Zone 0 – a place in which an explosive gas atmosphere is present continuously or for long periods or frequently with continuous release.

Zone 1 – a place in which an explosive atmosphere is likely to occur in normal operation occasionally with primary release.

Zone 2 – a place in which an explosive atmosphere is not likely to occur in normal operation but, if it does occur, will persist for a short time only with secondary release.

The volume, V_z , is defined as the volume within which the mean concentration of flammable gas arising from a release will be between 25 % to 50% of the Lower Explosive Limit (LEL). In the standard, the definition of the ‘degree of ventilation’ is applied to releases outdoors as well as indoors. Given the concept of ventilation is meaningless for outdoor releases, the gas cloud volume V_z should be seen as defining the degree of ‘dilution’ rather than ventilation. The standard allows the use of V_z can then be used to indicate where zoning is not required through the concept of negligible extent (NE).

CFD Calculation for Design Basis Accident (DBA) Release

CFD is extensively used in process safety to calculate hazard ranges for flammable and toxic materials, heat flux in fires, explosion overpressures and toxic cloud sizes. A Large Eddy Simulation (LES) based CFD procedure (which uses Navier-Stokes equations) is used to simulate a biogas release from biogas tank which is a DBA event. A release area of 0.25 mm² (0.5 mm diameter) has been considered as a non-vibrating system. The details of CFD/FHA methodology are given elsewhere [25].

CFD analysis has been used to estimate the combustible/explosive cloud size. The release has been simulated in three different configurations (top, bottom and side). Bottom leak does not result in burnable cloud formation as the biogas is a buoyant gas and it will not travel in downward direction. The release from side and bottom results in the formation of burnable cloud of almost equal size. This cloud

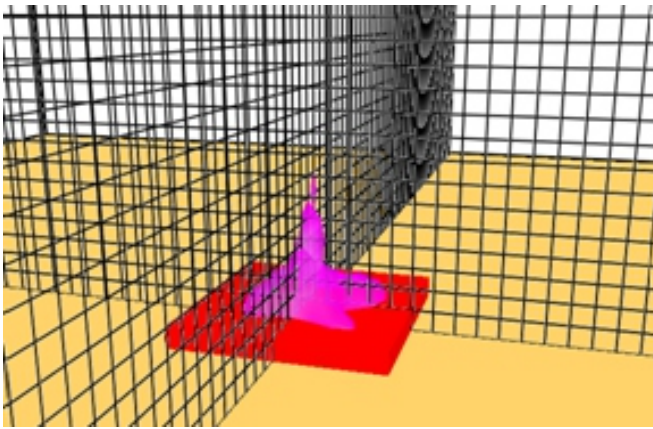


Fig.4: Biogas (Leak from top) volumetric concentration iso-surface between (LEL - UEL).

volume between Lower Explosive Limit (LEL) and Upper Explosive Limit (UEL) for top release (Fig.4) is less than 0.1 m^3 and if ignited may produce small pressure and thermal effect which is insignificant.

Design Basis Leak (DBL) of Biogas and Liquid Petroleum Gas (LPG) for Potential use in Hospital Kitchen

LES CFD analysis (using Navier-Stokes equations) of hospital kitchen has been carried out considering design basis leak of biogas and LPG [25]. Biogas being the lighter than air

makes a buoyant plume and tries to move upwards and strikes with the ceiling and spreads. However, LPG being heavier than air, makes a dense gas dispersion structures and tries to make a cloud in the lower portion of the enclosure. It was found that the volumetric concentration remains less than 5% for biogas release. However, the volumetric concentration for LPG gas release is more than 15 % of lower flammability limits. Fig.5 and 6 show volumetric concentration plot at an instant of time for biogas and LPG gas respectively. Which concludes that biogas is a relatively safer option in comparison to LPG.

BDBA Biogas Release from Storage Tank

LES CFD analysis (using Navier-Stokes equations) for BDBA biogas release from storage tank has been carried out [25] the building consisting biogas storage tank is the biggest safety concern area. In most of the DBA accident the biogas cloud size is insignificant. But in BDBA situations where a much higher quantity is coming out in atmosphere has to be analysed using CFD methodology for various possible leak sizes from the storage building. The green color obstacle is added to represent the storage building wall (in order to capture the realistic mixing around the source) in all large release area situation and in small area releases it is assumed at the domain only. The conservative quantity of combustible /explosive cloud was estimated with the help of clouds size (Fig.7) then, explosion/blast wave estimation were carried out using the experimental data from the literature as shown in Fig.8 [26].

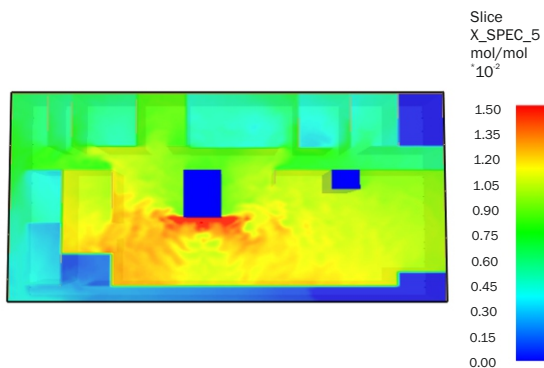


Fig.5: Biogas release volumetric concentration.

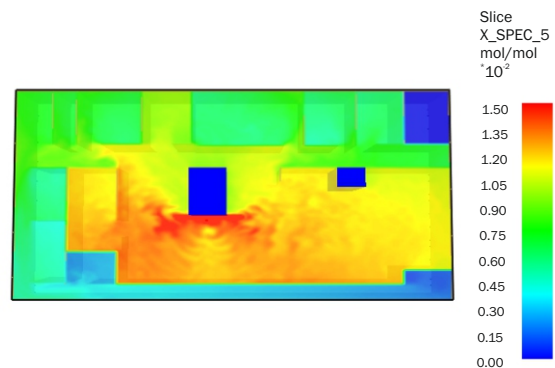


Fig.6: LPG release volumetric concentration.

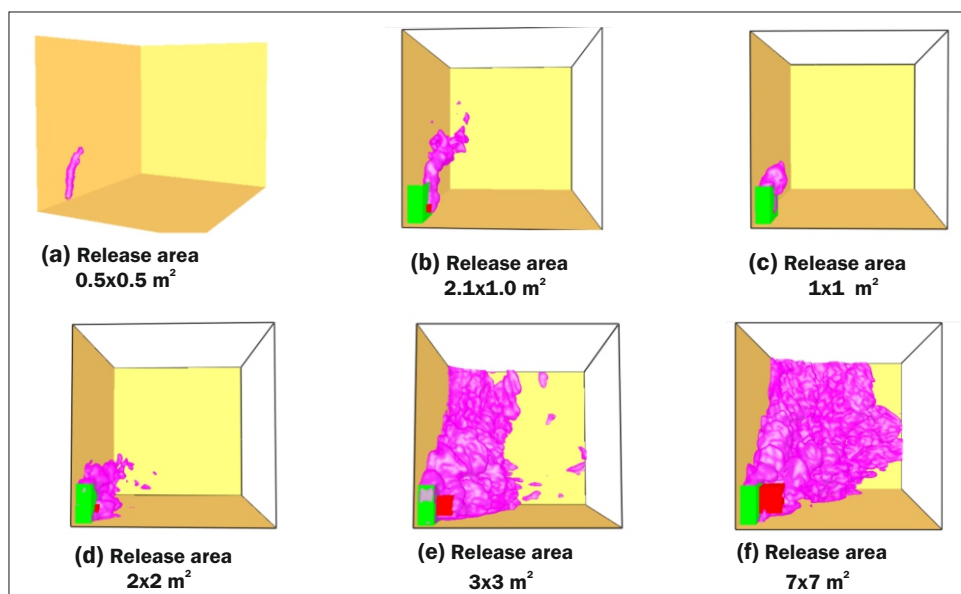


Fig.7: Biogas volumetric concentration cloud between 5% - 15%.

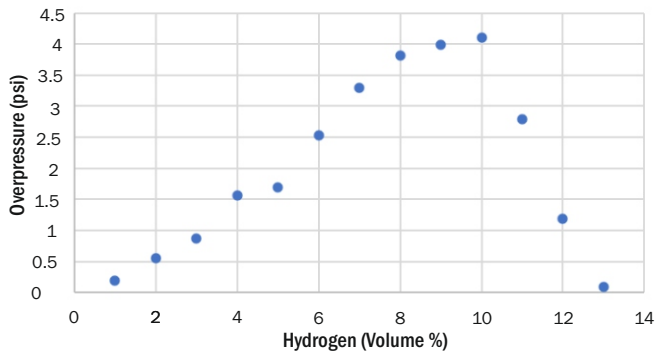


Fig.8: Average overpressure vs. concentration for small volumes of hydrogen.

Fig.8 shows overpressure for different hydrogen concentration cloud size which is generated nearly based on 200 experimental tests performed for volumes ranging from 340 litres to ~1850 litres utilizing spark igniters [26]. The data from the Fig.8 has been used in the present biogas fire hazard analysis with suitable energy severity corrections (biogas equivalent hydrogen).

In present situation, a biogas equivalent hydrogen quantity of about 123 liters is estimated from CFD which reside in biogas explosive cloud. Pressure rise calculation with a linear risk extension approach is as follows.

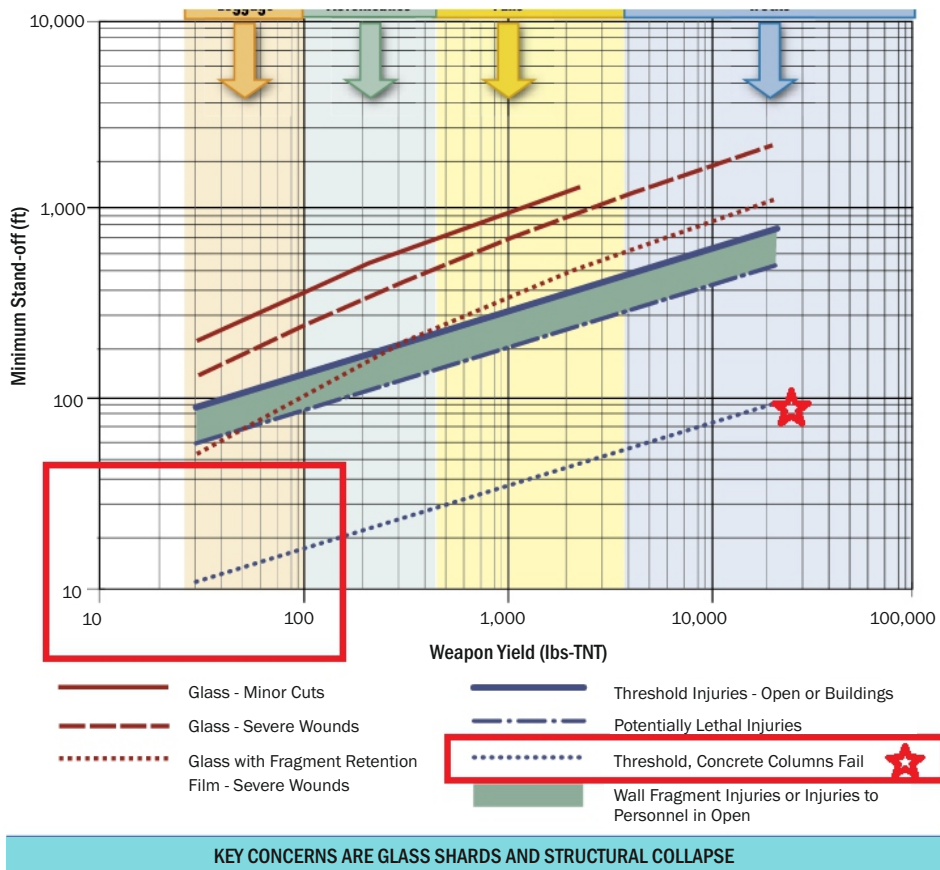
Pressure rise in biogas accident = biogas equivalent hydrogen quantity x pressure rise in reference case/ hydrogen quantity in reference case

$$123 \times 4.25 / 340 = 1.5375 \text{ psi or } 0.106 \text{ bar}$$

The pressure rise is found to be only 0.106 bar and will not pose any threat to building structure near (at least 11 ft away) to the facility. For a moderate damage to happen the overpressure should be more than 2.0 psi. But this kind of pressure rise requires demonstration of the risk in terms of death and ear injury by a Probit (probability + unit) regression analysis. It was established that the probability of death is negligible but ear damage probability is almost 10% and use of ear plug is advised at certain zone for longer stay. The biogas equivalent hydrogen combustion values shown above were used to find out the minimum separation distance in terms of Trinitrotoluene (TNT) equivalent [27]. So, for about 19.22 lb of TNT equivalent the minimum distance for failure of a concrete column is of the order of 11 feet and about 50 ft for glass breakage calculated from the Fig.9. Fig.9 shows safe distance against the explosive yield in TNT for different material of concern. Alternatively, suitable metal plates can also be placed to reduce safe distance for permissible limit against vulnerable location.

Biogas Toxicity Simulations

The concern was addressed for biogas toxicity (almost nonexistent as per designers) by taking a conservative H₂S fraction in biogas. The LES CFD (using Navier-Stokes equations) based H₂S dispersion study was carried out [25]. The biogas toxicity cloud due to H₂S is calculated for a range of DBA and BDBA scenarios by varying the size of break in storage building. The most likely conservative DBA case would be the door with a 2x2 m of size (shown in red color) (Fig.10-a). The iso surface reveal that the toxicity cloud exists only near to the release location except for a larger BDBA scenario (Fig.10-b). It is suggested to create a safety zoning and administrative access control neat the biogas storage area.



KEY CONCERNS ARE GLASS SHARDS AND STRUCTURAL COLLAPSE

Fig.9: Safe distance against the explosive yield in TNT.

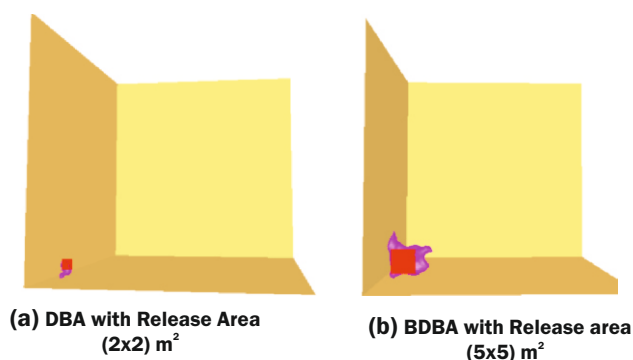


Fig.10: Biogas volumetric concentration cloud between 5% - 15%.

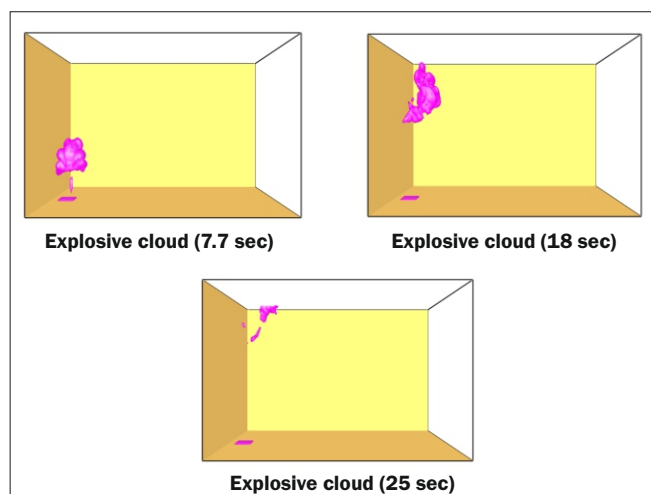


Fig.11: Biogas volumetric concentration cloud between 5% - 15%.

Cloud safe departure time calculation for Nisargruna plant for BDBA

The LES CFD simulation (using Navier-Stokes equations) have been carried out for complete biogas release (Storage tank area) instantaneously and safe departure time is calculated for safe movement of cloud upward [25]. The departure time depends upon the size and quantity of biogas plant. The cloud safe departure time calculation for Nisargruna plant at different instant of time is depicted in Fig.11 (the bottom face square is the injection and top moving iso-surface is the combustible cloud). The cloud covers a safety distance of about 150 m in about 30 second. The cloud moves away from the ground building and will keep on diluting. These purely hypothetical (unlikely) situation simulation results stress upon the need to strict ignition and fire sources control by a strong safety culture which will result in safe departure phenomenon along with passive dilution within a minute to keep the structure around the plant and worker safe. For this cloud size an ASD of 75 m was found to be adequate.

Conclusions

A CFD based first-of-its-kind fire hazard analysis approach of biogas plants against fire, explosion and toxicity related regulatory concerns has been developed. The developed methodology was used to qualify the Nisargruna facility at BARC hospital. The regulatory requirement in terms of explosive cloud size, toxic cloud size, explosion over pressure, acceptable separation distances, safe departure time and safety zoning was established. FHA for a range of DBA and BDBA events concluded no significant life-threatening effect on the occupants in safe zone, public building and

hospital kitchen. The CFD analysis has also depicted the relative safe nature of biogas over LPG. The biogas safety aspects (fire, explosion & toxicity) found to be safe during its utilization in hospital kitchen.

Acknowledgements

The authors thank Dr. Tapan Kumar Ghanty, Director, Bio-science Group, Dr. S.T. Mehetre, SO/F, NA&BTD, Shri Ranjan Kumar, Former Head, TSD, Shri Premchand Jain SO/G, TSD and Shri Manab Raychaudhuri, SO/E, TSD for providing inputs and useful discussions for the analysis.

References

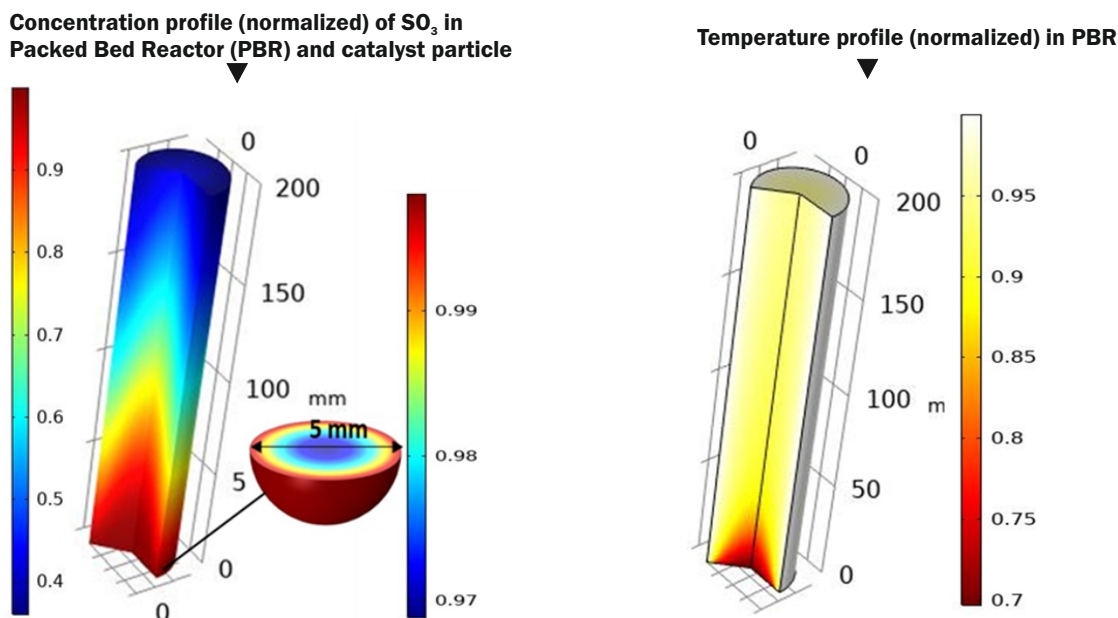
- [1] Guidelines for Substation and Power Distribution System of Buildings, CPWD, 2019.
- [2] IS SP 7-NBC : National Building Code of India, 2016.
- [3] Fire Protection Systems for Nuclear Facilities, AERB Safety Standard No. AERB/NF/SS/FPS (Rev. 1), 2010.
- [4] Casson Moreno V, Papisidero S, Scarponi GE, Guglielmi D, Cozzani V. "Analysis of accidents in biogas production and upgrading". *Renew Energy*. 2016;96:1127-1134.
- [5] Trávníček P, Kotek L. "Risks associated with the production of biogas in Europe". *Process Saf Prog*. 2015;34:172-178.
- [6] Hedlund F.H., Astad J, Nichols J. "Inherent hazards, poor reporting and limited learning in the solid biomass energy sector: a case study of wheel loader igniting wood dust, leading to fatal explosion at wood pellet manufacturer". *Biomass Bioenergy*. 2014;66:450-459.
- [7] Hedlund F. H., Nielsen M. F., Mikkelsen S. H., and Kragh E. K. "Violent explosion after inadvertent mixing of nitric acid and isopropanol - Review 15 years later finds basic accident data corrupted, no evidence of broad learning". *Saf. Sci.*, vol. 70, pp. 255-261, 2014.
- [8] Salvi O, Chaubet C, Evanno S. "Biogas: opportunities to improve safety and safety regulation". *Trans VŠB Tech Univ Ostrava Safety Eng*. 2012;7 (2):36-43.
- [9] Boscolo M, Bregant L, Miani S, Padoano E, Piller M. "An enquiry into the causes of an explosion accident occurred in a biogas plant". *Proc Safety Prog*. 2019;e12063. <https://doi.org/10.1002/prs.12063>
- [10] Hedlund, F. H. "Biomass accident investigations-missed opportunities for learning and accident prevention". In *Proceedings of the 25th European Biomass Conference and Exhibition* (pp. 1804-1814). ETAFlorence Renewable Energies. <https://doi.org/10.5071/25thEUBCE2017-4AV.2.45> Farm plant, Saint-Fargeau, France, (2017).
- [11] Moreno V. C. and Cozzani V. "Major accident hazard in bioenergy production". *J. Loss Prev. Process Ind.*, vol. 35, pp. 135-144, 2015.
- [12] Riviere C. and Marlair. G. "BIOSAFUEL (R), a pre-diagnosis tool of risks pertaining to biofuels chains." *J. Loss Prev. Process Ind.*, vol. 22, no. 2, pp. 228-236, 2009.
- [13] Nair S. "Identifying and managing process risks related to biofuel projects and plants". *HAZARDS XXII- Pap*. 103, no. 156, pp. 331-338, 2011.
- [14] Rivera S. S., Olivares R. D. C., Baziuk P. A., and McLeod J. E. N. "Assessment of Biofuel Accident Risk: A Preliminary Study". in *Proceedings of the World Congress on Engineering*, 2015, vol. 2.
- [15] Scarponi G. E., Guglielmi D., Moreno V. Casson, and Cozzani V. "Assessment of Inherently Safer Alternatives in Biogas Production and Upgrading". *Aiche J.*, vol. 62, no. 8, pp. 2713-2727, 2016.
- [16] Rossen J, Alligevel røg skidt i luften, *Arbejds miljø*, no. 1, pp. 13-16, 1991.

- [17] Sharma, P.K. "The new combined fire confinement and fire influence approach of fire hazard analysis/design safety margin evaluation for NPPs and reprocessing facilities". in: Technical Meeting on the Probabilistic Safety Assessment Framework for External Events, 3–6 August 2015, IAEA Headquarters, Vienna, Austria, 2015.
- [18] Determination of safety distances, IGC Doc 75/07/E, European industrial gases association AISBL.
- [19] API RP 581, Risk-based inspection technology, American Petroleum Institute (API).
- [20] Design basis events for pressurised heavy water reactor, AERB safety guide No. AERB/SG/D-5.
- [21] European Parliament and Council. Directive 1999/92/EC of the 16 December 1999 on minimum requirements for improving the safety and health protection of workers potentially at risk from explosive atmospheres. Official Journal of the European Communities L 23, 28/01/2000. 1999. pp. 57-64.
- [22] IEC (Italian Electrotechnical Committee). IEC 31-35. Explosive atmospheres: Guide for classification of hazardous areas for the presence of gas in application of EN 60079-10-1. 2014. pp. 36-60.
- [23] IEC (International Electrotechnical Commission). EN 60079-10-1. Explosive atmospheres classification of areas: Explosive gas atmospheres. 2009. pp. 50-66.
- [24] "Hazardous area classification of Natural gas installations", IGE/SR/25, Communication 1665, Institute of Gas Engineers, 2000.
- [25] Sharma, P. K. "Modelling of fire with CFD for Nuclear Power Plants (NPPs)". Advances of CFD in nuclear reactor design and safety assessment. In book: Advances of Computational Fluid Dynamics in Nuclear Reactor Design and Safety Assessment (pp.663-727 2019).
- [26] Richardson Erin. "An experimental study of unconfined hydrogen / oxygen and hydrogen /air explosions". Joint Army-Navy-NASA-Air Force (JANNAF) Combustion Conference, 2014. <https://ntrs.nasa.gov/archive/nasa/casi.ntrs.nasa.gov/20150002596.pdf>
- [27] Web: https://www.fema.gov/media-library-data/20130726-1455-20490-7465/fema426_ch4.pdf.

Double-Porosity Modeling

7

SO₃ Decomposition in Tubular-Packed Bed Reactor



S. Sujeesh

Scientific Officer

Chemical Technology Division, Chemical Technology Group

Bhabha Atomic Research Centre (BARC), Trombay - 400 085, INDIA

A ‘multi-scale’ problem-heat and mass transport taking place in the macro-pores(voids) of the catalyst bed & heat, mass transport and reaction occurring in the micropores inside the catalyst particle-has been modeled for catalytic decomposition of SO₃, in a tubular-Packed Bed Reactor.

Hydrogen is considered as an excellent energy carrier, with potential to replace fossil fuels. Iodine-Sulphur (IS) and Hybrid-Sulphur (HyS) water splitting cycles are efficient and widely studied processes for mass production of H₂. Decomposition of sulphuric acid (H₂SO₄) is a three-step and energy intensive process in both, IS and HyS cycles.

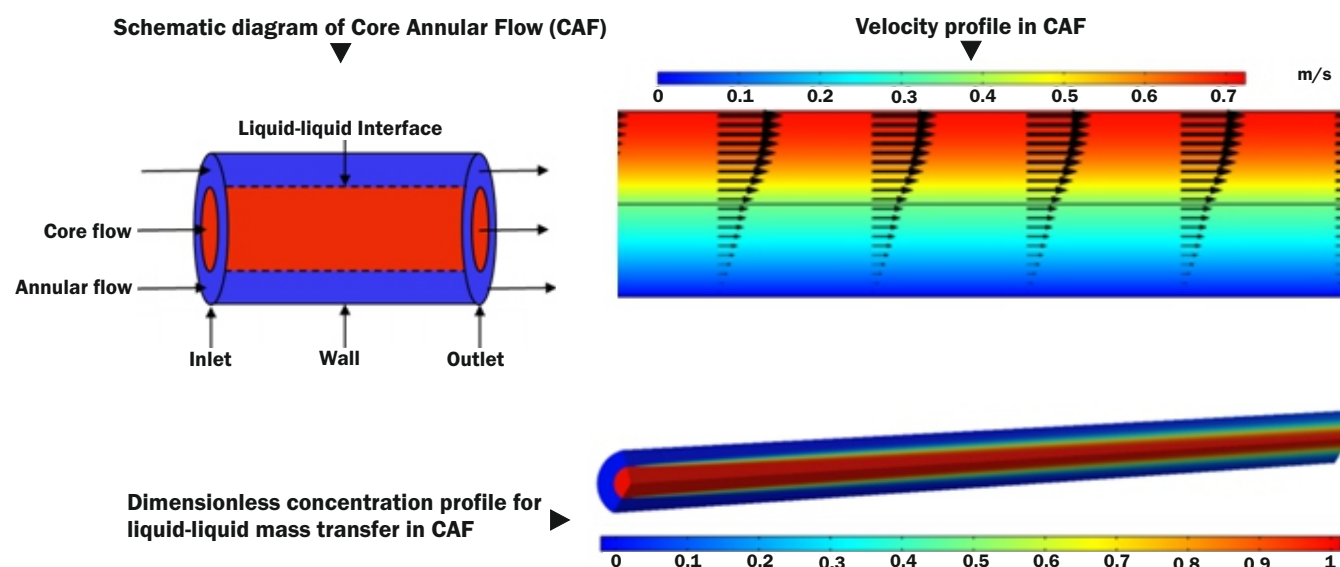
A recent study (Sujeesh et al., *Sulphuric acid decomposition using Cr-Fe₂O₃ catalyst in a tubular Packed Bed Reactor (PBR): Modeling and experimental studies*, *Int. J. of Hydrogen Energy* 2022, 47:11750-11763), shows better experimental prediction with the developed double-porosity model, than isothermal-PBR and plug-flow (1-D) models for catalytic decomposition of SO₃ which is one of the three steps of decomposition of sulphuric acid. Also, multi-scale analysis of the reaction system using the double-porosity model, shows negligible film resistance as compared to pore diffusion resistance. Inside the pores concentration drop near the wall is found to be higher than that near the centre line, which is due to the faster intrinsic reaction kinetics near the high temperature wall than diffusion rate inside the pore.

Modeling of transport phenomena together with SO₃ decomposition reaction in two different porous-domains of a PBR is the novelty of the work. The developed model is useful to maximize the conversion of SO₃ in a PBR by minimizing the heat and mass transfer resistances.

Core Annular Flow in Micro-fluidic Contactor

8

CFD Modeling of Liquid-Liquid Flow and Mass Transfer



Rajnish Kumar Chaurasiya

Doctoral Fellow (DDFS), Homi Bhabha National Institute (HBNI)
 Chemical Engineering Division
 Bhabha Atomic Research Centre (BARC), Trombay - 400 085, INDIA

CFD modeling of Core Annular Flow in a micro-fluidic contactor provides fundamental understanding of liquid-liquid mass transfer, including dependence of dimensionless concentration boundary layer thickness and local Sherwood number on key dimensionless numbers. Correlations for estimating local Sherwood numbers are also obtained.

Micro-fluidic contactors are well known as process intensifying contactors owing to their features such as shorter diffusion length, high specific interfacial area, high overall volumetric mass transfer coefficients. Micro-fluidic contactors have been explored extensively for various liquid-liquid separations including the ones relevant for nuclear fuel cycle. Depending on the operating conditions and design of the micro-fluidic junction, different types of liquid-liquid flow patterns such as slug flow, droplet flow, core annular flow (CAF) may result in a micro-fluidic contactor. In this study (Chaurasiya & Singh, *CFD modelling of mass transfer in liquid-liquid core-annular flow in a microchannel*, *Chem. Eng. Sci.* 2022, 249: 117295), a CFD model to estimate mass transfer coefficient in CAF in a micro-fluidic contactor is reported.

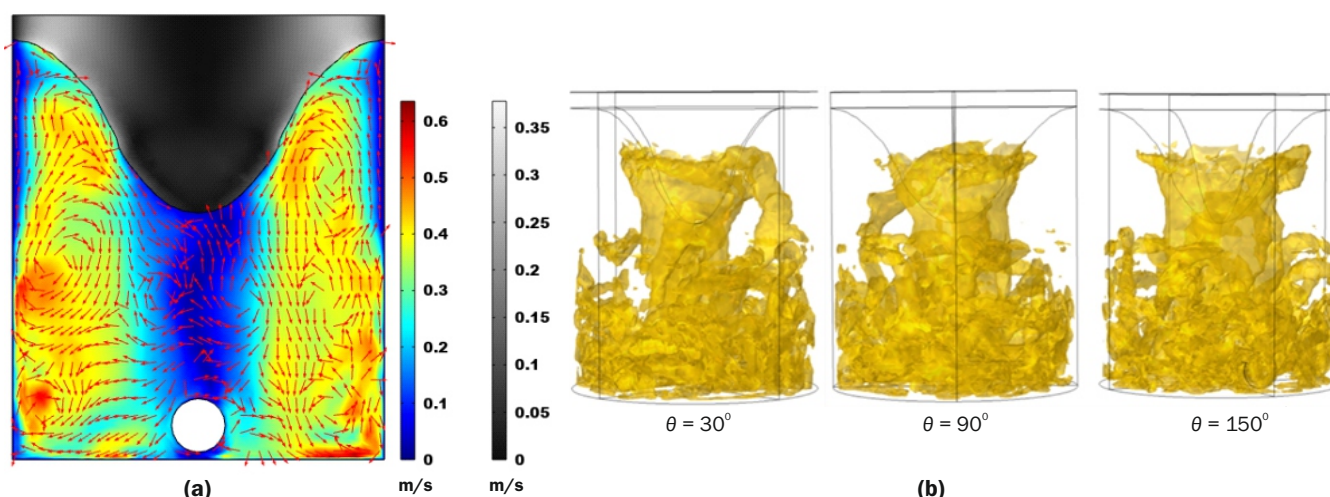
CFD model involves numerical solution of Navier-Stokes and species transport equations with appropriate boundary conditions of velocity and shear stress applied on the liquid-liquid interface. The results of CFD simulations have been used to quantify the variations of dimensionless concentration boundary layer thickness on the core side and annulus side with dimensionless length, Reynolds number, Schmidt number, Graetz number, and distribution coefficient.

Film theory and penetration theory of mass transfer are evaluated for their applicability for liquid-liquid mass transfer in CAF and the latter is found to be suitable to predict the mass transfer coefficient with contact time defined as the ratio of the distance from the leading edge of the microchannel to interfacial velocity. CFD-based correlations to estimate core side and annulus side local Sherwood numbers have been reported. These correlations are useful to estimate overall mass transfer coefficient, which is prerequisite for design of micro-fluidic contactors.

ANN-CFD Modelling

9

A Novel Computational Model to Simulate Flow in a Vortex Mixer



(a) Profiles of axial velocity magnitude and velocity vectors in a vertical central plane passing through the vortex mixer.
 (b) Snapshots of Q-criterion iso-surfaces for different angular positions of the stirrer.

Sourav Sarkar

Scientific Officer

Chemical Engineering Division, Chemical Engineering Group

Bhabha Atomic Research Centre (BARC), Trombay - 400 085, INDIA

A novel ANN-CFD model for simulating flow in a vortex mixer is presented. Combining ANN and CFD model circumvents the need of computationally expensive interface-tracking simulations required to capture the vortex shape.

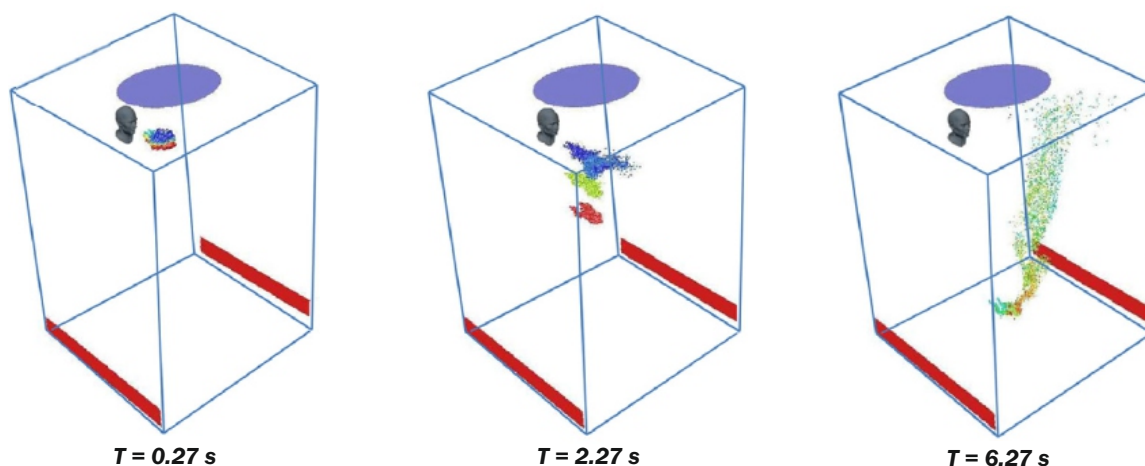
Liquid phase mixing is a very basic unit operation which is extensively used in chemical processes. Conventionally, liquid phase mixing is achieved by using impellers. However, for several applications passive mixing devices which do not require maintenance are indispensable. A vortex mixer, which is basically a vessel contents of which are mixed by a magnetic stirrer, is one such device and has several potential applications.

In a recent study (Sarkar *et al.*, *A novel ANN-CFD model for simulating flow in a vortex mixer*, *Chem. Eng. Sci.* 2023, 260: 117819), a numerical model to simulate flow in a vortex mixer is reported. The presence of vortex makes the simulation of the vortex mixer very challenging and requires a model capable of capturing vortex shape (air-liquid interface). Such interface-tracking simulations are computationally expensive. In this work, a combination of Artificial Neural Network modelling and CFD modelling has been used to circumvent the need of interface-tracking simulations. An ANN is trained and validated using a large set of experimental data of vortex shape acquired using high-speed imaging for different parametric conditions. The trained and validated ANN is used to predict the vortex shape for the cases for which CFD simulations of the vortex mixer are required. The vortex shape predicted by the ANN is incorporated into the computational domain itself, obviating the need of interface-tracking simulations and thereby reducing a two-phase CFD problem to a single-phase CFD problem in which flow fields of the domain representing air and domain representing liquid are solved with appropriate boundary conditions specified at the air-liquid interface. The ANN-CFD model is validated with the reported PIV data. The validated model is used to have detailed insights into the flow physics, including turbulence structures in the vortex mixer.

Eulerian–Lagrangian CFD Modeling

10

Transmission, Evaporation of Cough Droplets Inside an Elevator



Snapshots of the cloud of droplets generated due to coughing action by a person inside an elevator at different instants of time from the start of the coughing action. The color scale is for droplet diameter (dark blue represents the smallest droplets and dark red represents the largest droplets).

Nirvik Sen

Scientific Officer

Chemical Engineering Division, Chemical Engineering Group

Bhabha Atomic Research Centre (BARC), Trombay - 400 085, INDIA

A CFD model is developed to simulate transmission and evaporation of droplets generated due to coughing action. The model is used to understand spread of cough droplets inside an elevator for different scenarios.

Several practices were followed for social distancing during COVID-19 pandemic. These included practices on using elevators also such as only one person should use the elevator at a time, the persons using elevator should stand facing the walls of the elevator etc. To have a more scientific basis of such practices, fundamental studies on how the droplets generated due to coughing or sneezing action move and evaporate in different settings are needed. A pertinent question is what happens if someone coughs inside an elevator. An attempt was made to answer this question by carrying out numerical simulations. For this, a 3D Eulerian-Lagrangian CFD model was developed and used to understand the transmission and evaporation of micron-size droplet generated due to coughing action. Effect of turbulence created by the air puff associated with coughing action was considered. Effect of humidity on evaporation of droplets was also considered. Different possible scenarios varying in presence/absence of fan inside the elevator, number of persons coughing, direction of ejection of cough droplets, ambient relative humidity and temperature were postulated and simulated.

The results obtained showed that in presence of proper ventilation inside the elevator (in the form of a top-mounted fan), most of the ejected cough droplets fall to the ground before impacting other persons standing in the elevator. However, in absence of the fan, droplets sweep through a large volume inside the elevator after getting entrapped in the flow induced by the air puff exhaled during coughing action. An increase in temperature and a reduction in relative humidity increase the fraction of droplets getting evaporated. This work (Sen, Transmission and evaporation of cough droplets in an elevator: Numerical simulations of some possible scenarios, *Physics of Fluids* 2021, 33, 033311) was chosen as the Editor's pick.

INSIGHTS INTO LASER SCIENCE

By Dhruba J. Biswas

A Beginner's Guide to Lasers and Their Applications by Dhruba J. Biswas is an exceptional book that delves into the fascinating world of lasers. With its intuitive approach and accessible language, it opens the doors to laser science for a wide range of readers, including those from various scientific disciplines and curious enthusiasts.

The book begins by acknowledging the monumental impact of lasers on humanity since their invention in 1960. From being initially seen as a solution in search of problems, lasers have permeated almost every field imaginable, as evidenced by the numerous Nobel Prizes awarded for laser-related discoveries. However, most existing books on lasers cater to experts, researchers, or graduate students, leaving a gap for a beginner-friendly resource.

What sets this book apart is its ability to present complex concepts without relying on intricate mathematical explanations. Instead, Biswas employs an intuitive approach, allowing readers with a basic understanding of high school physics to grasp the fundamentals of laser science. The author's aim is to engage a diverse audience, including those in physics, chemistry, engineering, medicine, biology, and any curious individual seeking to explore lasers.

One of the book's notable strengths is its perfect balance between lucid text and clear illustrations. The author successfully maintains technical depth and scientific accuracy while ensuring readability and comprehension. Complex concepts are simplified and complemented by visuals, making it easier for readers to visualize and understand the principles behind lasers.

Adding to the book's appeal are the intriguing anecdotes scattered throughout the text. Drawing from historical events and milestones, these anecdotes not only provide context but also ignite the readers' curiosity. They serve as captivating reminders of the significant role lasers have played in shaping scientific advancements.

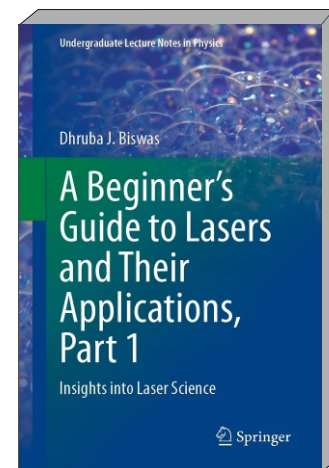
A Beginner's Guide to Lasers and Their Applications, Part-1: Insights into Laser Science

By Dhruba J. Biswas
Former Head

Laser & Plasma Technology Division, BARC

Springer Nature

Date of Publication: 12 May, 2023



"A Beginner's Guide to Lasers and Their Applications" is a remarkable book that bridges the gap between laser science and a broader audience. Dhruba J. Biswas has skillfully crafted a resource that combines clarity, scientific rigor, and captivating storytelling. Whether you are a beginner in the field or simply intrigued by the wonders of lasers, this book is an excellent choice for expanding your knowledge and appreciation of this groundbreaking technology.

RBI Governor visits BARC

India has emerged resilient in the post-COVID period and is widely believed globally to remain as the fastest growing major economy. This is powered by India's sound macroeconomic policy setting and innate growth potential. A desirable national goal and an aspiration of all of us is the expectation that India would become an advanced economy by 2047. It is necessary that technology and research play a very prominent role along with other determinants of growth. Premier national institutions like the BARC have played a pivotal role in India's impressive technological advances over the years. It is now time to aspire for even greater goals, greater heights recognizing that frontier technologies are advancing at a fast pace globally and these advancements in technology offer immense new growth opportunities for our country.

There's a big difference between advanced economies and the emerging market economies in terms of innovations, patents adoption of frontier technologies and knowledge generation due to the rising barriers to technology, differential trade capital flows and labor mobility, driven partly by geopolitical factors. Investment in research and innovation in India is only 0.69 per cent of GDP as compared to 2.8 per cent in the United States of America, 4.3 per cent in Israel and 4.2 per cent in South Korea. Recognizing these emerging challenges, the Indian government has announced the National Education Policy 2020. It has also circulated the draft of the National Science Technology and Innovation Policy in 2020, and has unveiled the National Research Foundation (NRF) very recently to promote research and innovation. The NRF will be an apex body providing high level strategic direction to research in the country at a total estimated cost of Rs. 50,000 crore during the five-year period 2023 to 2028. Through these new initiatives, the Government of India aims at building an all-encompassing open science framework to provide access to scientific data information knowledge and resources to the Indian science technology and innovation ecosystem.

Nuclear power is an important low emission source of electricity and contributes to nearly 10 per cent of global electricity generation. In India, renewable energy is critical to achieving The 'Net Zero' emission transition. Nuclear energy in 2022-23 accounted for 2.8 per cent of total electricity generation in India. Nuclear power must remain among the range of options available to reduce the share of non-fossil fuel in India's energy mix to facilitate the green transition, as highlighted in the report on Currency and Finance 2023 brought out by the Reserve Bank of India. Access to technology and mineral resources at an affordable cost will be very critical.

India should harness its R&D capabilities by capitalising on benefits of globalisation

Shri Shaktikanta Das said in his speech delivered at Graduation Function event in BARC.

The current focus of the Department of Atomic Energy (DAE) can produce far-reaching consequences for our country and these include lasers, plasma research, exploration, mining extraction and utilization of atomic minerals. Increasing dependence on new technologies used in batteries, solar panels and wind turbines, green hydrogen, carbon capture utilization and storage, and e-waste management would require higher expenditure on research and development and strategic collaboration. Currently, there is a high degree of concentration in the supply solar supply chain, which needs to be overcome. A lot of work is already going on in these identified areas and I would like to complement DAE for spearheading and providing the required leadership in this area to our country, which will ensure a safe, secure, resilient and strong India.

The RBI is perhaps among the very few central banks in the world which has got a wide range of responsibilities which spans from monetary policy to regulation of the banking system. Ensuring financial stability and overall economic stability of the country is the primary role of the RBI and we have focused on this with greater attention in the aftermath of the COVID-19 and in other critical scenarios. In the face of all of that, Indian banking system remained stable and resilient, thanks to the work which the RBI along with the banks undertook in the recent years and supported by the government. So, today amidst the global financial market turmoil coupled with a slowing economic growth globally, India's GDP expanded 7.2 per cent last year.



RBI Governor articulates 5-point mantra for SUCCESS

It is very essential that individual countries develop their own capabilities while it is essential to recognise and capitalise on the benefits of globalisation which we have been doing over the past few decades

INSTITUTIONAL PRIDE it is necessary to imbibe institutional pride, which encompasses organisational culture, ethics, values and above all a spirit of a sense of humility in everything that you do in any organisation.

POSITIVE MINDSET it is very essential to have a positive mindset in whatever work we do. One should not be in a situation where there's a feeling that you are not at the core of activities. One should develop keenness to leave a mark in whatever they do.

WORK-LIFE BALANCE do not neglect your family life in the urge to work hard when there are tough assignments. You can give the best results if you have a happy family life.

LEARNING life is all about constant learning, and there is learning to do at every point of time in our career. It comes not just from books alone. It also sometimes comes from the junior most officers in an organisation. It emerges out of a group interaction out of a synthesis of ideas of many you know.

TEAMWORK it's very essential to maintain cordial interpersonal relationship and become a part of a team. The importance of teamwork is very critical in any organisation. The willingness to learn from the team as well as the willingness to work as a part of the team is really very important.



Left: Dr. A.K. Mohanty handing over a memento to Chief Guest Shri Shaktikanta Das.

Bottom: Young Scientific Officers who passed out from 66th Batch of BARC Training School pose for a photograph with Chief Guest, Dr. A.K. Mohanty, Chairman AEC and other senior officials.





trombay
colloquium*
July 27, 2023

From Cosmic Rays to Neutrinos

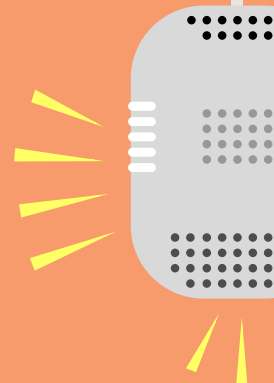
Experimental Particle Physics Research in India

India has a rich history in indigenous development of particle detectors and conducting experiments in the field of cosmic rays and particle physics. D. M. Bose at Kolkata, Piara Singh Gill at Aligarh, and Homi J. Bhabha at Mumbai were the early pioneers. From 1960 onwards, a series of experiments conducted at the deep underground laboratory at Kolar Gold Fields using indigenously developed detectors have put India on the world map of experimental science. India also has an ambitious plan to build a giant 50 kton magnetized iron calorimeter to study the fundamental properties of neutrinos. Many noteworthy developments in the journey of India's particle physics research were covered during the talk.



Prof. Naba K. Mondal

INSA Senior Scientist
Saha Institute of Nuclear Physics, Kolkata



*The Trombay Colloquium is a key window of opportunity for the BARC community to brainstorm with eminent individuals belonging to a wide spectrum of science & technology and allied domains. Prominent scientists and technologists are invited



trombay
colloquium*
August 24, 2023

On the occasion of Birth Centenary of Dr. Homi N. Sethna
Doing and Leading Science in India
Lessons from my Book of Life

What are the key lessons that I have learnt while doing and leading science in India? I learnt that there is nothing like basic science or applied science, only science and its application. Further, only those who say the first or last word in science are remembered. Be bold, chase anomalies. These will open windows to new knowledge. Be borderless, as breakthroughs occur at interfaces. I also learnt that it is the power of ideas that matters and not the power of budget. Message matters, it brings focus, inspires and alliance. Making high-technology work for the poor matters so do science that creates access equality despite income inequality. All these lessons were elaborated with concrete real life examples to the large BARC audience.

Dr. Raghunath Mashelkar
Former Director General
CSIR

to BARC Trombay to deliver captivating talks on emerging domains of science, and the transformative effect of new technological innovations.

BARC

CHINTAN BAITHAK

brainstorming science & technology for cutting edge in-house R&D



@National Green Hydrogen Mission

R&D IN SPOTLIGHT

Iodine-Sulfur process

High temperature intensive.

Thermochemical-cum-electrochemical water splitting.

Metallic closed loop structure.

Demonstrated nuclear hydrogen generation using integrated metallic closed loop process (@150 Nlph).

Copper-Chlorine process

Low temperature intensive.

Thermochemical-cum-electrochemical water splitting.

Metallic closed loop structure.

Demonstrated nuclear hydrogen generation using integrated metallic closed loop process (@5 Nlph).

Alkaline Water Electrolysis.
High Temperature Steam Electrolysis.
Proton Exchange Membrane.
Biological route (nitrogen fixing bacteria: Nostoc PCC7120).
Ammonia decomposition (membrane-assisted reactor).

R&D IN FOCUS



The Bhabha Atomic Research Centre (BARC) over the years has piloted multidisciplinary in-house R&D activities in pursuit of India's National Mission for Green Hydrogen. Many of these activities have already resulted in scalable technology outcomes. A brief update on achievements so far alongside several noteworthy initiatives being pursued in BARC to meet the desired objectives of the mission in the short-term to long term period is presented here.



NOVEL MATERIALS
Ti,CrV alloy, Magnesium, Metal hydrides, WO₃ and (Er, W): BiVO₄ rich 2D heterojunction photoelectrode, Membrane electrodes, Photocatalysts: TiO₂, In₂TiO₇, g-C₃N₄.

TECH TRANSFER
Alkaline Water Electrolyzer.

TECH INCUBATION
PSU oil & gas giant BPCL.

Key resource persons

Dr. A. K. Tyagi, Director, Chemistry Group
Dr. Mrinal R. Pai, Chemistry Group

Contributors

Chemical Technology Group. Chemical Engineering Group. Chemistry Group. Materials Group. Bioscience Group.

Speakers

1. Dr. A. K. Tyagi 2. Dr. Nafees Ahmed V.
3. Smt. Deepa Thomas 4. Dr. Atindra M. Banerjee

@ Crystal Based Detector Program

Chalking out a roadmap for achieving self-sufficiency in advanced single crystal scintillator based radiation detectors, single crystal growth of semiconductor detectors, and lab-grown diamonds. A brief update on several noteworthy initiatives being pursued in BARC to meet the desired objectives of the ambitious program in the short-term to long term period is presented here.

Securing scintillator raw material supplies

Highly important LaBr_3 and CeBr_3 materials to be mass produced locally by leveraging IREL supply base of Lanthanum and Cerium

DAE's technological expertise to assist sustained hi-tech production efforts

Targeted time frame for localization: 5-7 years



1



2



3



4

Speakers

1. Dr. S.M. Yusuf
2. Dr. Ranu Bhatt
3. Dr. Shreyas Pitale
4. Dr. Dheeraj Jain

Producing large diameter scintillator crystals

Proposed DAE-Crystal Growth Center (DAE-CGC) coming up near BARC (F) Visakhapatnam Centre in PPP model

Seamless industry-scientists networks for ensuring quick tech commercialization

Single Crystal Growth of Semiconductor Detectors

In-house manufacturing of HPGe crystal based Gamma detectors

Semiconductor-grade polycrystalline Si production at Heavy Water Board (Talcher)

DAE-CGC to aid efforts for making both HPGe detectors and 10-12 inch diameter Si single crystals

Meeting National Semiconductor Mission mandated goals

Lab-grown diamonds for advanced technology applications

High quality single crystal laboratory grown diamonds (LGDs) and large-area polycrystalline LGD

Water - The elixir of life

BARC water technologies

secure the needs of Border Security Force

Chemical Engineering Group & SIRD Editorial Team

Bhabha Atomic Research Centre, Trombay - 400 085, India

India's premier organization for research and development activities in nuclear energy sector, Bhabha Atomic Research Centre (BARC), continues to expand its pan-India footprint through deployment of new technologies that serve wider societal benefit. The technology for treating seawater to supply clean drinking water, developed in BARC, has now been deployed at Creek Border Outposts, BSF Bhuj, Gujarat.

The two 1000 litres per hour capacity desalination plants - commissioned at BSF Bhuj (at Lakkinala and Lakhpatwari) recently - would now ensure proper supply of clean drinking water to meet the day-to-day requirements of security forces stationed near the international border. The desalination plants - developed based on BARC supplied technology knowhow - were manufactured by a Rajkot-based firm Osmotech Membranes Pvt. Ltd. The membrane based technology incorporated in these plants is equipped to reject high levels of dissolved salts present in seawater to provide clean and safe drinking water.

The facility was formally inaugurated on 1 September, 2023 by Shri Ravi Gandhi, Inspector General, Gujarat Frontier BSF; Shri K. T. Shenoy, Director, Chemical Engineering Group, BARC and Shri A. K. Adak, Head, Desalination & Membrane Technology Division, BARC in the presence of Shri Anant Singh, Deputy Inspector General, BSF Bhuj; Shri Sanjeev Kumar, Commandant, 18 BN, BSF Bhuj; Shri Shreyas Vagadia, Director, M/s. Osmotech Membranes Pvt. Ltd.

Two 1000 litres per hour capacity desalination plants (equipped with BARC technological knowhow), now installed in one of the remotest locations of the country, would ensure proper supply of clean drinking water to serve the needs of India's security forces



Top: Senior personnel of BARC Trombay and BSF preside over a function organized to mark the official commissioning of desalination plant.



Bottom: Inside view of desalination plant commissioned at BSF Bhuj.



परमाणु ज्योति PARMANU JYOTI

Department of Atomic Energy further expands the reach of pan-India school outreach mission – during August 2023, Parmanu Jyoti reaches out to over 10,000 students in 48 Jawahar Navodaya Vidyalayas (JNVs) across the states of Andhra Pradesh, Karnataka, Kerala, and Telangana.

“...this programme is aptly named Parmanu Jyoti as it aims to spread the light of knowledge about atomic energy in India...”



A Message to the Next Generation *Dr. A. K. Mohanty, Secretary, DAE & Chairman, AEC.*



JNV BIDAR, KARNATAKA

A New Perspective *Igniting the young minds and encouraging them to think out-of-the-box.*



Ambassadors of Atomic Energy Young scientists and engineers from BARC as Parmanu Mitra.



BONDING OF TRUST Mindful engagement of Parmanu Mitras with students, Overnight stay at the schools.



CONNECTING THE DOTS Putting ideas together to deepen the understanding of DAE Societal Technologies.



JNV KHAMMAM, TELANGANA

BUILDING THE BRIDGE *between the ideas and improvisation, guiding them for future possibilities.*



JNV RAMANAGARA, KARNATAKA



JNV CHITRADURGA, KARNATAKA



JNV EAST GODAVARI, TELANGANA

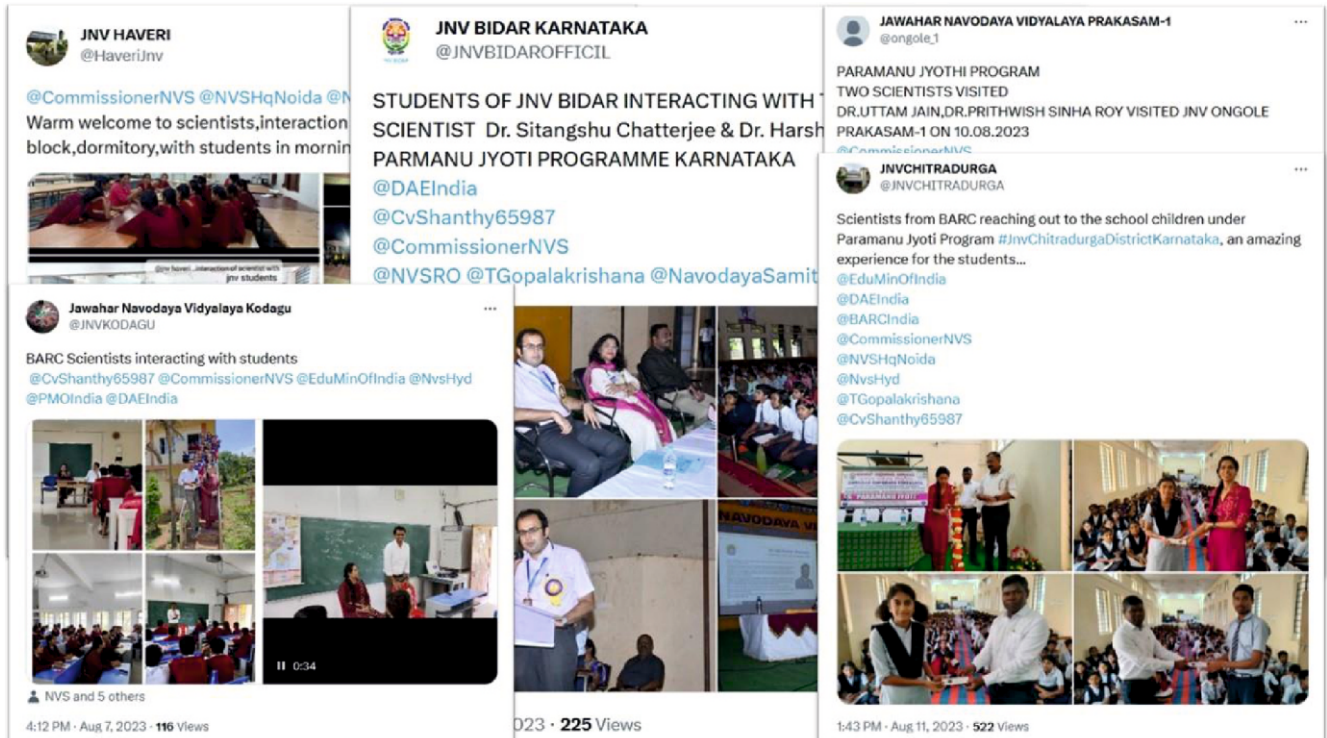


JNV MEDAK, TELANGANA

BACK TO SCHOOL *Parmanu Mitras mingle with the students.*



MEDIA COVERAGE Amplifying the impact of our mission, Spreading awareness far and wide.



ADVOCACY JNVs participating in the social media campaign on Paramanu Jyoti.

परमाणु ज्योति

60000+ STUDENTS

150+ SCHOOLS

100+ SCIENTISTS

34 STATES & UTs

3 CAMPAIGNS

1 MISSION



#BackToSchool



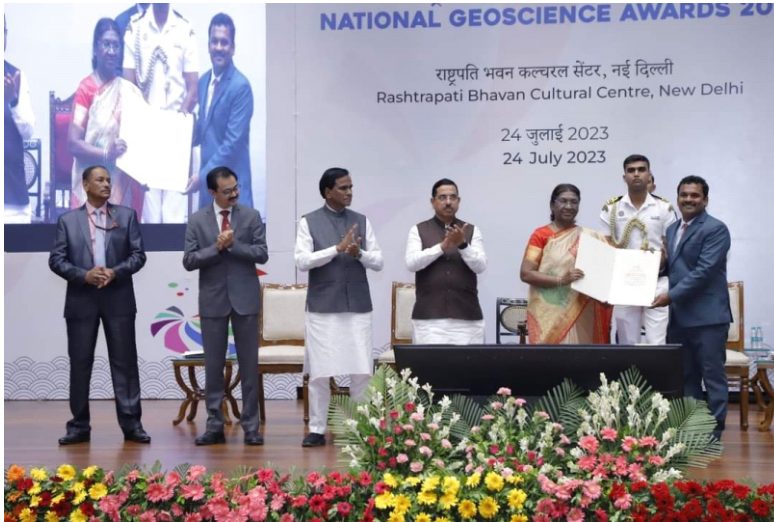
PAN-INDIA COVERAGE *Concurrent Execution at Multiple Locations for Effective Management.*



*Joining hands
and taking atomic energy
to the young minds of the country*

Science Communication, Outreach and Public Engagement (SCOPE) Section, NCPW, DAE.
Scientific Information Resource Division (SIRD), BARC.
Public Awareness Division (PAD), NCPW, DAE.

National Geoscience Award for BARC scientist



President of India Smt. Droupadi Murmu hands over National Geoscience Award to BARC scientist Dr. K. Tirumalesh at a formal event held on 24 July, 2023 in New Delhi.

The National Geoscience Award (NGA) scheme instituted by the Ministry of Mines, Government of India, has announced the awards for the year 2022 on March 28, 2023.

Dr. K. Tirumalesh, Scientific Officer/G of Isotope and Radiation Application Division, Radiochemistry & Isotope Group, BARC has been selected for this prestigious award jointly with Dr. Harish Bahuguna, Director, Geological Survey of India (GSI), Jammu.

The President of India Smt. Droupadi Murmu has conferred these awards in a function organized at Rashtrapati Bhavan Cultural Centre on July 24, 2023. Minister of Coal, Mines & Parliamentary Affairs, Shri Pralhad Joshi, Minister of State for Coal, Mines & Railways, Shri Rao Saheb Patil Danve, Secretary, Ministry of Mines, Shri Vivek Bhardwaj and Director General of Geological Survey of India, Dr. Janardan Prasad, graced the occasion.

Twenty-two geoscientists, including working professionals and academicians from across the country received the awards grouped under three categories namely National Geoscience Award for Life Time Achievement, National Young Geoscientist Award and National Geoscience Awards in various fields of geosciences. Dr. K. Tirumalesh has been awarded under Applied Geology category in recognition of his contribution to water resources development and management using isotope technology. The award carries a certificate and cash prize of Rs. 300,000/- shared equally between both awardees.

This page is intentionally left blank



The maiden CFD issue with articles specific to its applications in Chemical Engineering, Materials Science & Safety, published in Nov-Dec 2021 issue of BARC Newsletter.

Edited & Published by

Scientific Information Resource Division

Bhabha Atomic Research Centre, Trombay, Mumbai-400 085, India

BARC Newsletter is also available at URL:<https://www.barc.gov.in>